11-1-2022 1:30 PM

Mechanical Evaluation of Gyroid Structures to Combat Orthopaedic Implant Infections

Sydney Hitchon, *The University of Western Ontario*

Supervisor: Willing, Ryan, *The University of Western Ontario*
Co-Supervisor: Holdsworth, David, *The University of Western Ontario*
A thesis submitted in partial fulfillment of the requirements for the Master of Engineering Science degree in Biomedical Engineering

Abstract

Treatment of infected orthopaedic implants often require two separate surgeries to clear the infection and install a replacement implant. Current antimicrobial drug delivery methods are inefficient, and each additional surgery increases the physiologic burden on patients, with an increased risk of infection, decreased range of motion and longer recovery times. Porous orthopaedic implants, with adequate strength for permanent implantation and the ability to house and elude more efficient antibiotic delivery systems, could result in a single surgery to treat orthopaedic infections. Therefore, finite element models of porous gyroid structures at different porosities were developed and compared with experimental results. Discrepancies in predicted and actual apparent elastic moduli and fatigue lives were found due to anomalies caused from the 3D-printing of the specimens, however, similar relationships across porosities were observed. A case study of a porous gyroid humeral stem was created to evaluate the mechanical capabilities of the porous stems as well as their impact on humerus mechanobiology. The porous stems were found to exhibit adequate strength in three different bone densities during four different arm motions. Some evidence of improved bone remodelling behaviours was observed when comparing the effects of the porous stems versus a traditional solid stem.

Keywords

Orthopaedic Infections, Revision Surgery, Gyroid, Finite Element Modelling, Bone Mechanobiology, Implant Design

Summary for Lay Audience

Infection in orthopaedic implants often requires intervention through a process known as two-staged revision surgeries. One surgery is performed to remove the infected implant and replace it with a temporary implant loaded with antibiotics. About 90% of these antibiotics remain trapped within the temporary implant and do not get delivered to the body. The other 10% of the antibiotics are delivered at an unideal rate, with an initial burst of antibiotics followed by a rapid decline of antibiotic delivery. This process of drug delivery increases the body's resistance to antibiotics. Once the infection has been cleared, a second surgery is performed to replace the temporary implant with a new permanent implant. A porous implant that has adequate strength for permanent implantation could be used to house a more ideal antibiotic delivery system, which delivers a larger percentage of drugs at a more efficient rate. This could allow for just a single surgery to be performed to treat an infected orthopaedic implant, as opposed to two surgeries. In addition to improving drug delivery, a secondary benefit of a porous implant is the ability to better mimic the natural structure of bone. This imitation provides the potential for mitigating stress shielding, which is a known complication of orthopaedic implants that causes a loss of bone density.

A porous structure, known as the gyroid, was analyzed at five different porosities using computer models and physical experimental tests. A computer model was developed that was able to demonstrate accurate relationships between cylindrical gyroid porosities for static compression and fatigue tests. Shoulder implants were then created using these gyroid structures and implemented into computer models to predict their mechanical behaviours. These models showed that the gyroid-based shoulder implants, at porosities of 60%, 70%, and 80%, should be strong enough to withstand typical arm motions. It was also determined that compared to traditional solid implants, these porous implants should not have any further negative impacts on the bone remodelling of humeri of three different bone qualities. Future work should explore variations of these gyroid-based shoulder implants, such as the use of porosity gradients, to attempt to further improve the resulting bone effects.

Co-Authorship Statement

Chapter 1:

Manuscript Author – Sydney Hitchon

Manuscript Revisions – Sydney Hitchon, Ryan Willing, David Holdsworth

Chapter 2:

Study Design – Sydney Hitchon, Ryan Willing, David Holdsworth

Gyroid Design – Sydney Hitchon, Gregory Hong, Jaques Milner

Model Design – Sydney Hitchon, Jaques Milner, Todor Ivanov, Ryan Willing

Data Analysis – Sydney Hitchon

Manuscript Preparation – Sydney Hitchon

Manuscript Revisions – Sydney Hitchon, Ryan Willing, David Holdsworth

Chapter 3:

Study Design – Sydney Hitchon, Ryan Willing, David Holdsworth

Model Design – Sydney Hitchon, Pendar Soltanmohammadi, Ryan Willing

Data Analysis – Sydney Hitchon, Pendar Soltanmohammadi, Ryan Willing

Manuscript Preparation – Sydney Hitchon

Manuscript Revisions – Sydney Hitchon, Ryan Willing, David Holdsworth

Chapter 4:

Manuscript Author – Sydney Hitchon

Manuscript Revisions – Sydney Hitchon, Ryan Willing, David Holdsworth

Acknowledgements

I would like to thank my supervisors, Dr. Ryan Willing and Dr. David Holdsworth, for their incredible advice and guidance throughout this project. I would also like to thank my advisory committee members, Dr. Yara Hosein and Dr. Matthew Teeter, who were able to provide wonderful insights from outside the bubble of the project. Thank you to William Anderson, Gregory Hong, Todor Ivanov and all the members of the Biomechanical Engineering Research Lab for all their help and support during this study. A special thanks goes to Jaques Milner for his immense help with this research.

Outside of my research bubble, I would like to say a big thank you to one of my closest friends, who made moving by myself to a new city during a global pandemic a little less scary: Lauren Smith. And of course, an indescribably massive thank you to my family, specifically my parents, who have always made me believe that I could do anything I put my mind to. I would not be here without you.

Table of Contents

List of Tables

List of Figures

Chapter 1

1 Introduction

Revision surgeries for orthopaedic implant complications are a financial, physiological, and mental burden on patients and healthcare resources. More than 10,300 hip and knee revision surgeries were performed in Canada in 2019-2020 with estimated inpatient costs of $177 million [1]. On average, revision surgery led patients to stay in hospitals for 9.0 days compared to 3.8 days for patients undergoing primary joint replacement surgery. Average inpatient cost (excluding rehabilitation) was 70.2% higher for revision surgery than for a primary joint surgery. Infection is one of the leading causes for revision surgery of total joint replacements. Infection was the cause for 25.4% and 33.9% of hip and knee revisions in 2019-2020, respectively. Considered the gold standard, two-staged revision surgeries are often employed when an orthopaedic implant is infected [2-5]. The first surgery is performed to remove the infected implant and replace it with a temporary spacer. This temporary spacer is typically made of polymethyl methacrylate (PMMA), also known as bone cement, which is loaded with antibiotics to clear the infection. These bone cement spacers can withstand lesser loads and can result in a smaller range of motion than that of their permanent metal counterparts [6]. Additionally, PMMA has less than ideal drug elution kinetics [7]. Only around 10% of the antibiotics loaded into PMMA will elude into the body [8]. This elution also occurs at an inconsistent rate, with a quick initial delivery followed by an exponential decline [9]. Three to six months after this primary surgery, a secondary surgery is performed to replace the temporary spacer with a new permanent implant. These two-staged revision surgeries are a major burden on our healthcare systems and patients.

Additionally, a complication associated with orthopaedic implants is their vulnerability to stress shielding. Stress shielding is the result of implants that have a much higher stiffness than the surrounding bone, affecting the remodelling behaviour of that bone. This is due to the mechanobiological behaviour of bone, which has adaptive modelling processes based on long-term loading behaviours. This stress shielding can cause bone densities to decrease, which both weakens the bone and can lead to implant loosening.

The development of a permanent porous implant can help combat orthopaedic device-related infection (ORDI). A porous implant could be loaded with a biodegradable drug delivery system, which has superior drug elution kinetics [10], allowing for revision surgeries to be performed in one stage instead of two. The porous implant, loaded with antibiotics, would replace the need for

a temporary spacer and instead be implemented in the sole revision surgery. In addition, a porous implant can be designed to better match the stiffness of bone, potentially mitigating the stress-shielding effects currently faced. A porous implant is not only applicable to revision surgeries but could possibly be employed in the primary surgery, therefore potentially reducing the need for revision surgeries.

This chapter describes common anatomical terms, bone anatomy, joint arthroplasty, stress shielding, two-staged revision surgeries, additive manufacturing, triply periodic minimal surfaces, and finite element modelling. This chapter finishes with an overview of the next three chapters.

1.1 Anatomical Terms

Universal anatomical terms have been established to ensure consistency in the medical fields. The human body has been divided into three distinct planes as described in Figure 1-1.

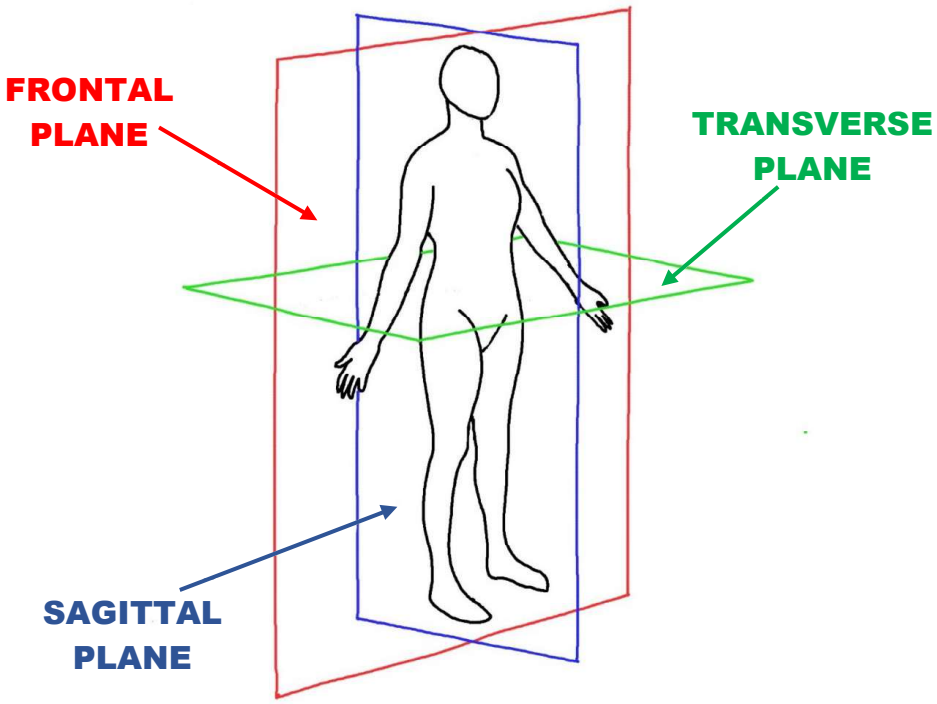

Figure 1-1. Anatomical planes of the human body. The sagittal plane divides the body into left and right sides. The frontal plane divides the body into front and back sides. The transverse plane divides the body into top and bottom parts.

Using the anatomical planes, we can describe the movement of our joints and appendages along these planes. Focusing specifically on the movements of the glenohumeral joint of the shoulder, flexion/extension are the movements of the arm along the sagittal plane and abduction/adduction are the movements of the arm along the frontal plane, as shown in Figure 1-2. Anatomical

positions are also established to identify specific locations of the body in relation to each other as described in Figure 1-3.

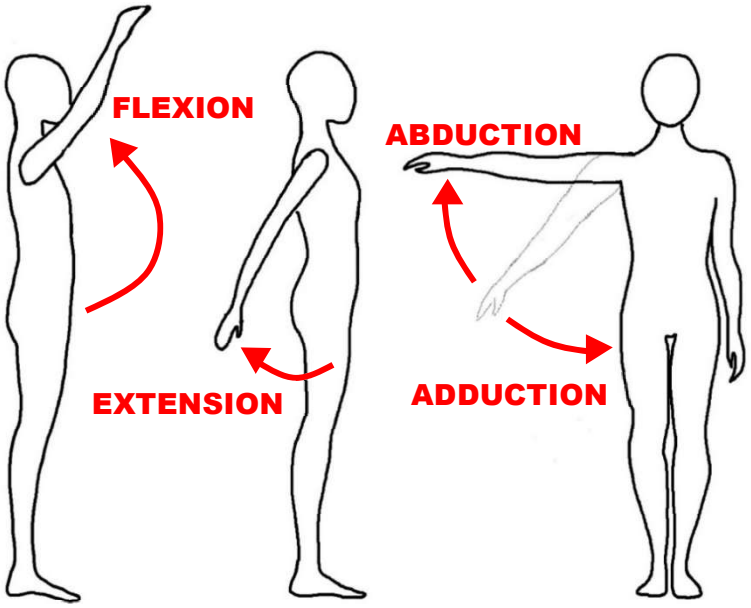

Figure 1-2. Anatomical motions of the shoulder joint and upper limb. Flexion refers to a decrease in the angle between two body parts. Extension refers to an increase in the angle between two body parts. Abduction refers to movement of appendages away from the body. Adduction refers to movement of appendages towards the body.

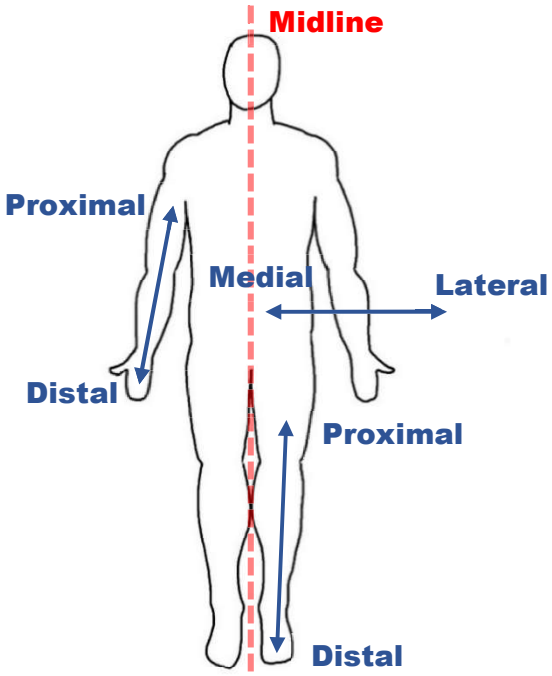

Figure 1-3. Anatomical directions of the human body. Proximal refers to being closer to the trunk. Distal refers to being farther away from the trunk. Lateral refers to being farther from the midline (where the sagittal plane crosses). Medial refers to being closer to the midline.

1.2 Anatomy of the Long Bone

Long bones are defined as being longer than they are wide [11]. The femur, tibia, and humerus, which are the main bones involved in hip, knee, and shoulder arthroplasties, are categorized as long bones. Long bones are divided into three main components: the diaphysis, the metaphyses and the epiphyses, as shown in Figure 1-4. The diaphysis is the main shaft of the bone consisting of the medullary cavity and an outer shell composed of cortical bone (also known as compact bone). The epiphyses are the regions at each end of a long bone, which are filled with trabecular bone (also known as cancellous or spongy bone). The metaphyses are the regions, also known as necks, that connect the diaphysis with the epiphyses.

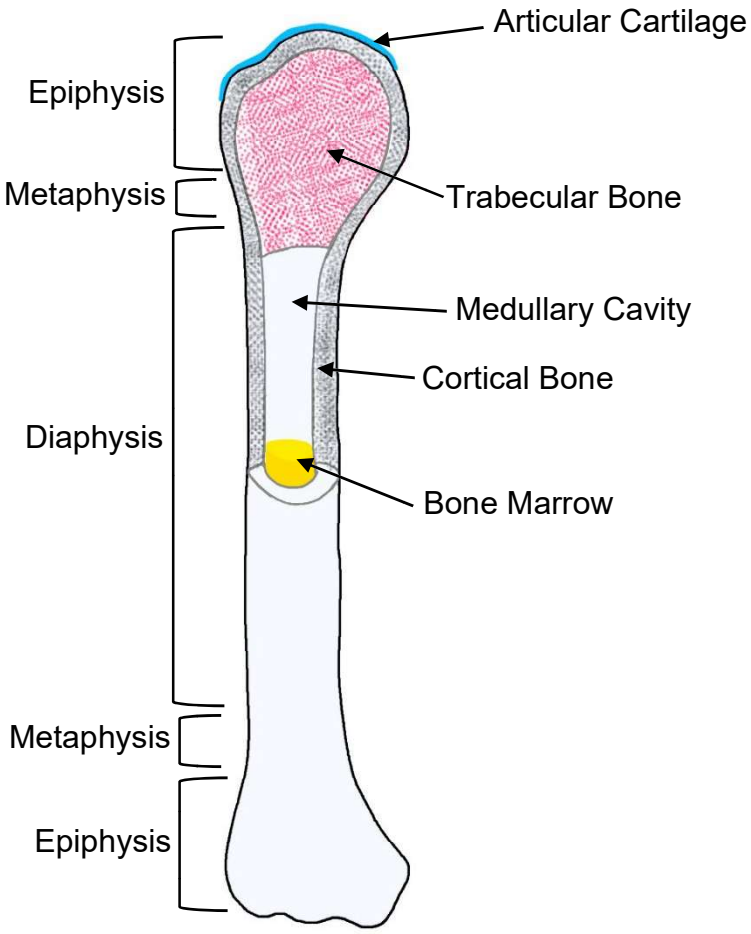

Figure 1-4. Anatomy of a long bone.

Cortical bone is the denser and stronger of the two bone tissues [12]. Its main functions are protection and support. It is composed of osteons, which are parallel tubes that run along the length of the bone tissue. This composition of cortical bone leads to its anisotropic behaviours, exhibiting greater strength in the longitudinal direction than the radial and circumferential

directions. In contrast, trabecular bone is composed of trabeculae which are lattice-like constructs. The lattices are formed along stress lines in the bone to help in support while decreasing the bone's mass. This heterogenous structure of trabecular bone makes it anisotropic as well, exhibiting the greatest strength in compression and the least in shear. The reported Young's moduli for trabecular and cortical bone is 10.4-14.8 GPa and 18.6-20.7 GPa, respectively [13].

Bones are composed of four different cell types that are critical to their function: osteoblasts, osteocytes, osteogenic cells, and osteoclasts. Osteoclasts and osteoblasts are the cells responsible for bone resorption and formation, respectively. Human bone undergoes a constant cycle of bone resorption/formation which is dependent on the mechanical loading that it experiences [11,14]. Once bones are in their adult life, meaning they are no longer growing in length, they maintain their structure through a process called bone remodeling. The osteoclasts will resorb damaged or old bone and in the same location, osteoblasts will deposit new minerals to replace the resorbed bone. This bone remodeling process adapts to the mechanical needs of the host. In a sedentary individual, where the bone is experiencing long-term lessened mechanical loads, the bone will have a greater percentage of bone resorption than formation, therefore decreasing the bone's mass. In contrast, an active individual, whose bones are experiencing increased long-term mechanical stresses, will have bone formation occurring at a rate greater than bone resorption, therefore increasing bone mass. This mechanical loading dependency can cause issues when employing orthopaedic implants, as they affect the mechanical loads experienced by these bones. This leads to a phenomenon called stress shielding which will be discussed further in Section 1.3.

1.3 Bone Remodelling and Stress Shielding

Julius Wolff made a significant impact on our current understanding of the mechanobiology of bones, starting with his first publication in 1870 [15-16]. His work led to our understanding of how mechanical loading affects the structure of our bones, also known as Wolff's law. Wolff's law states, "the law of bone remodelling is the law according to which alterations of the internal architecture, clearly observed and following mathematical rules, as well as secondary alterations of the external form of bones following the same mathematical rules, occur as a consequence of primary changes in the shape and stressing or in the stressing of bones [17]." Essentially, he discovered that the structure of healthy bones will adapt to the mechanical loads they experience.

In 1976, Cowin et al. were the first to quantify the bone remodelling process with equations, hypothesizing that the cortical bone remodelling process is strain-dependent [18]. In 1986, Fyhrie

et al. expanded upon this strain-dependent bone remodeling theory by considering the anisotropic properties of trabecular bone [19]. Their theory was developed to predict the effects of applied stress on trabecular orientation and apparent density. In 1987, Huiskes et al. further adapted these models to theorize that adaptive bone-remodeling can be characterized by the homeostatic strain energy density (SED) distributions [20]. They observed the stress-shielding effects of prostheses, using finite element modeling (FEM). Additional studies have been conducted observing the effects of stress-shielding from shoulder prostheses using finite element analysis, in vitro cadaveric experiments, and radiographic imaging [21-23].

When bones experience fracture or develop disease states, implantation is often the treatment of choice. With joint arthroplasty, a stem component is often implanted into the bone, outlined in Section 1.4. These solid metal stems often have a significantly higher stiffness (resistance to deformation) than that of the native bone. Solid Ti-6Al-4V (a common titanium alloy used in joint arthroplasties) has a Young's modulus of ~110 GPa whereas trabecular and cortical bone have Young's moduli of 10.4-14.8 GPa and 18.6-20.7 GPa, respectively [13]. This means when loads are applied to the implanted bone, the stem will assume most of that load, leaving the native bone to experience smaller than typical loads. This is what is known as stress shielding. As known from Wolff's law, this reduction in stresses and strains experienced by the native bone affects its remodeling process.

Many studies have been conducted to try and mitigate the effects of stress shielding. Different types of stem geometries, including hollow stems, short stems, long stems, porous stems and stemless implants, different fixation techniques, such as press-fit vs. bone cement, and different materials have been investigated to try and evaluate their effects on stress shielding [24-40]. Although the main purpose of this study is not to mitigate stress shielding effects, it is important to ensure that these porous implant stems will not further negatively impact bone mechanobiology. It is an added benefit if we discover a smaller mechanobiological impact from these porous stems than traditional solid stems.

1.4 Joint Arthroplasty

Joint arthroplasties are a common procedure performed to provide relief from pain caused by joint disease, trauma and injury, and aging. From 2018-2019, there were 75,220 knee, 61,645 hip, and 6,247 shoulder replacements performed in Canada [41]. Although total shoulder replacement is not as common as knee and hip replacement, shoulder arthroplasty is predicted to increase by 755.4% for patients over 55 years old and 333.3% for patients younger than 55 years old from

2015 to 2030 [42]. The Canadian Institute for Health Information reported a 5-year standardized percentage increase in knee, hip, and shoulder replacements of 9%, 8%, and 36%, respectively, between 2014-2019 [41].

The first reports of each of these joint arthroplasties were in the late 19th century. The first total knee replacement (TKR) was a hinged designed, made of ivory, by Themistocles Gluck in the 1890s [43]. These implants often failed from infection, inadequate mechanical properties, and poor fixation [44]. The hinged TKR was further developed by Dr. Waldius in the 1950's by using acrylic and then eventually cobalt chrome (Co-Cr). The modern-day TKR has strayed from the artificial hinge joint and instead involves resurfacing of the distal femur and proximal tibia. These resurfacing components typically include a stem component which is inserted into the femur and tibia for fixation.

Gluck is also accredited with the first reported hip replacement in 1891, where he replaced the femoral head of tuberculosis patients with ivory [45]. The first total hip replacement (THR) was cultivated in 1938, by Wiles, and has informed the modern hip implant [46]. Mechanical failure of THR in the early 20th century could be attributed to inadequate design and poor material choices. Charnley transformed THR by introducing low-friction torque, acrylic cement for fixation and the use of polyethylene as a bearing material. Although a variety of THR methods are used today, such as cemented and cementless fixation, most hip implants consist of a stem which is inserted into the proximal femur, a femoral head component, and an acetabular (socket of the hip bone) component, just as Charnley did 50 years ago.

In 1893, the first total shoulder replacement was performed in Paris, by surgeon Jules Emile Péan, to treat tuberculosis [47]. Although it provided adequate mobility, the implant, made of a platinum tube and a hardened rubber ball, was removed after two years in the patient due to a persistent fistula. Evidence of several plastic shoulder implants were recorded in the 1950s, made of materials including acrylic, polyamide and polyethylene [48]. These prostheses provided poor shoulder mobility and the polyethylene prostheses failed due to poor fixation. In the 1950's, Krueger [49] and Neer [50] guided the development of modern metal shoulder implants. In 1950, Krueger developed the first metal implant for shoulder hemiarthroplasty, made of cobalt chromium alloy (vitallium), which provided adequate mobility without pain [49]. In 1953, Neer implanted his first prosthesis and developed the following criteria for prostheses: must be made of an inert material with a similar elasticity to bone, should preserve normal anatomy, and should have a long stem with a large surface area to sufficiently anchor to the bone while avoiding bone

resorption [50]. Although the importance of a long stem is still being investigated [24], their developments of shoulder prostheses are similar to the interventions used today. Total shoulder replacement (TSR) typically has a stem which is implanted into the proximal humerus, a spherical head replacing the native humeral head, and a glenoid (concave surface of the scapula) component [51]. Examples of TKR, THR, and TSR are shown in Figure 1-5. These orthopaedic implants can be made from a collection of materials including titanium, cobalt chromium, stainless steels, and ceramics. Implant materials are chosen for a variety of reasons such as their strength, weight, elastic modulus, wear resistance, biocompatibility, and manufacturability. A medical grade titanium alloy, Ti6Al4V, is a common implant material which has a good corrosion resistance, yield strength and a moderate elastic modulus (closer to bone than Co-Cr alloys) [52], and will be used in the included studies.

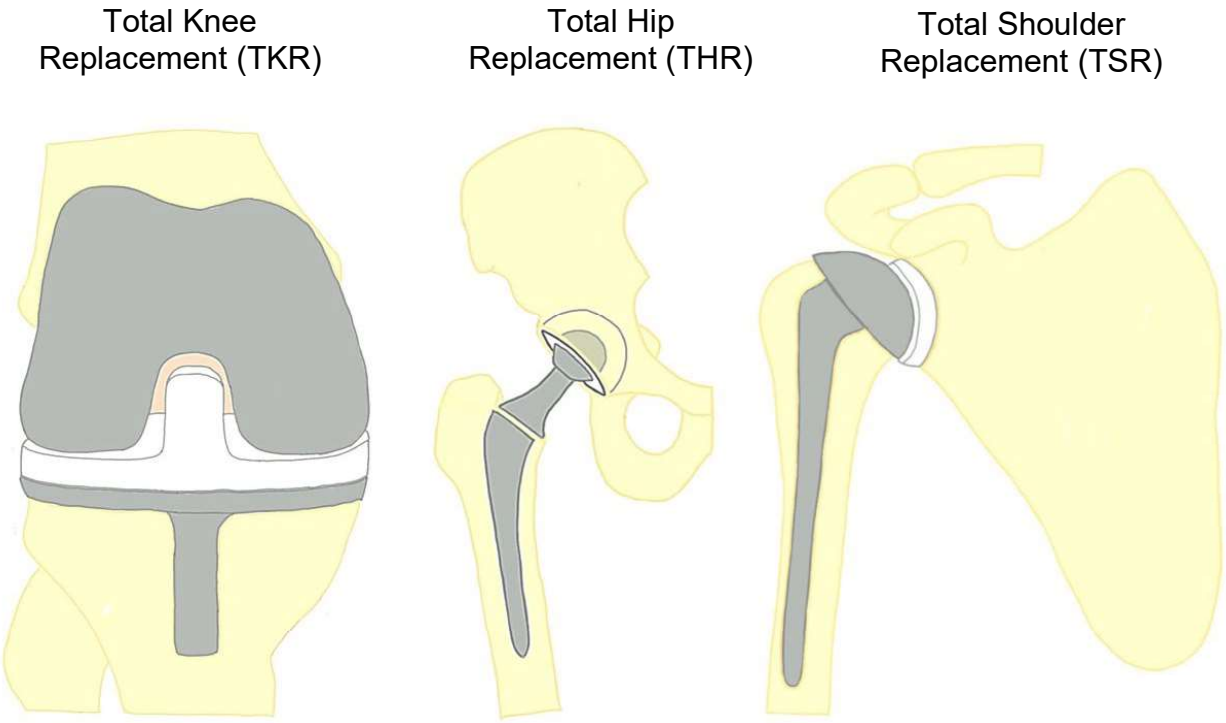

Figure 1-5. Three main types of joint replacement surgeries.

For all three joint arthroplasties, a stem component is typically implanted into the necessary bone(s), with the exception of some TKRs. The study of porous structures for better antibiotic delivery is the focus of this research and could be applied to all three of these surgeries.

1.5 Orthopaedic Device-Related Infection

Orthopaedic device-related infection (ODRI) is the encompassing term for fracture-related infection (FRI) and periprosthetic joint infection (PJI) [53]. ODRI is caused by an adherence of bacteria on or around an orthopaedic implant, forming what is known as a biofilm, and a decrease in host immunological defenses. There is always a risk for ODRI when undergoing implantation of an orthopaedic device. For total arthroplasties, the rate of infections is between 1%-5% [54-55]. Although this seems small, the impacts of these infections are substantial, therefore requiring research into the improvement of these surgeries. Untreated ODRI can lead to systemic infections such as sepsis or pneumonia [56]. Additionally, the risk of infection increases with each subsequent surgery [57-58]. When ODRI occurs, interventions to mitigate it's affects are required. This can include antibiotic therapy, resection arthroplasty, debridement and lavage, and one-staged and two-staged revision surgeries [59]. Two-staged revision is considered the gold standard for treating orthopaedic implant infection but there has been an increased interest in investigating the use of single-staged revisions. Reducing the number of surgeries that a patient undergoes can improve patient satisfaction and potentially improve overall mobility and range of motion [4]. The overall goal of this thesis is improving the treatment of orthopaedic implant infections by reducing two-staged revision surgeries to one-staged revisions. This research can also be applied to improving current one-staged approaches or even primary surgeries to potentially reduce the rate of infection.

1.5.1 Two-staged Revision Surgeries

Two-staged revision surgeries work by performing a first surgery where the infected implant is removed and a temporary spacer, loaded with antibiotics, is implanted into the bone. After the infection has been cleared, a second surgery is performed to replace the temporary spacer with a new permanent implant. Two-staged revision surgeries are considered the current gold standard for treatment of ODRI [2-5], however there are still many drawbacks to this approach.

The temporary spacer, employed in the first surgery, is typically made of polymethyl methacrylate (PMMA), also known as bone cement. These bone-cement spacers are not intended for permanent implantation due to their insufficient mechanical properties. A retrospective study by Jung et al. showed that more than 50% of patients that undergo a two-staged hip revision surgery for the treatment of ORDI will experience at least one non-infection related complication, the most common being mechanical malfunction of the bone cement spacer [60]. The compressive strength of PMMA decreases significantly with increasing amounts of impregnated antibiotics,

further increasing the risk of their use [61-62]. Although not intended for permanent implantation, there are reported cases of shoulder arthroplasty patients refusing to undergo the second surgery, leaving them with these temporary spacers permanently in their bodies [6,63].

In addition to mechanical disadvantages, PMMA also has inefficient drug elution kinetics [7]. Antibiotics are only released from the surface and pores of PMMA resulting in approximately 10% of the employed antibiotics actually eluding into the body [8]. The elution timeline of the antibiotics is not ideal, with an initial “burst” of drug release followed by an exponential decline [9]. These elution characteristics, coupled with the non-resorbing nature of PMMA, leaves it susceptible to bacteria growth and the potential development of antibiotic resistance [64]. As well, the curing process of PMMA creates high temperatures, which prevents the use of thermo-sensitive antibiotics [65]. Resorbable antibiotic carriers have been studied and compared to PMMA to improve upon local drug delivery. Several biodegradable carriers, such as calcium sulfate, have been shown to perform as well as or better than PMMA in terms of antibiotic elution and prevention of bacterial growth [8,66-67].

In addition to the problems related to bone cement spacers, there are certain risks associated with performing multiple additional surgeries. With every additional surgery a patient has, the risk of infection increases [58,68]. In addition to the negative physical effects of undergoing multiple surgeries, there is a huge mental toll on both patients and their caregivers [69]. Revision surgeries are also more expensive than primary replacements for both hospitals and patients, who are likely to require more time away from work [1].

A porous implant could be loaded with a biodegradable antibiotic carrier such as calcium sulfate. If the porous implant had adequate strength for permanent implantation, and allowed for the necessary drug elution kinetics, only one revision surgery would be needed. This would help mitigate these negative impacts that two-staged revision surgeries present or if employed in the primary surgery, potentially prevent the need of a revision surgery altogether.

1.6 Porous Structures

The idea of integrating porous structures with orthopaedic implants has been studied for decades. In 1971, Welsh et al. were studying the use of porous surfaces to improve the fixation between bones and implants through osseointegration [70]. By 1980, several others were investigating the use of porous surfaces for bony ingrowth on implants and Bobyn et al. were attempting to determine the optimum pore size for such applications [71]. More recently, studies have also been

conducted to explore porous implants for other reasons such as drug delivery and mitigation of stress shielding [72-74]. When choosing porous structures for use in orthopaedic implants, especially for entire structures as opposed to just surfaces, it is necessary to consider their mechanical properties to ensure their survival. One classification of porous structures, known for their high strength to low weight ratios, are triply periodic minimal surfaces.

1.6.1 Triply Periodic Minimal Surfaces

H. A. Schwarz published the first example of a triply periodic minimal surface (TPMS) in 1865 known today as Schwarz's diamond surface [75]. In 1883, Schwarz's student, E.R. Neovius, discovered another TPMS known today as the Neovius surface [76]. In 1970, Alan Shoen published an account of twelve additional examples of periodic minimal surfaces, free from self-intersections [77]. Minimal surfaces are characterized as having minimized surface areas also known as having zero mean curvatures [78].

The normal curvature, k, at a point, P, is the intersection of the surface normal and tangent plane shown in Figure 1-6. If the curve bends towards/away from the surface normal, then the curvature is positive/negative [79]. The principal curvatures, k_1 and k_2, of a surface at a point, P, are the maximum and minimum values of the normal curvature. The mean curvature, H, at a point, P, is defined by these principal curvatures in Equation 1-1. When the mean curvature of a surface is zero at all points on that surface, then it is defined as a minimal surface. A triply periodic minimal surface is a minimal surface that is translated in all three directions.

$$H(p) = \frac{k_1 + k_2}{2} \qquad \text{(Equation 1-1)}$$

These triply periodic minimal surfaces can be expressed by mathematical functions making them easier to model. The three most studied and well understood TPMSs today are the diamond, primitive, and gyroid surfaces. TPMS-based structures are often made in one of two ways [80]. Sheet-based TPMS structures are made by thickening the surfaces whereas skeletal-based TPMS structures are made by solidifying the pores of the surfaces as shown in Figure 1-7.

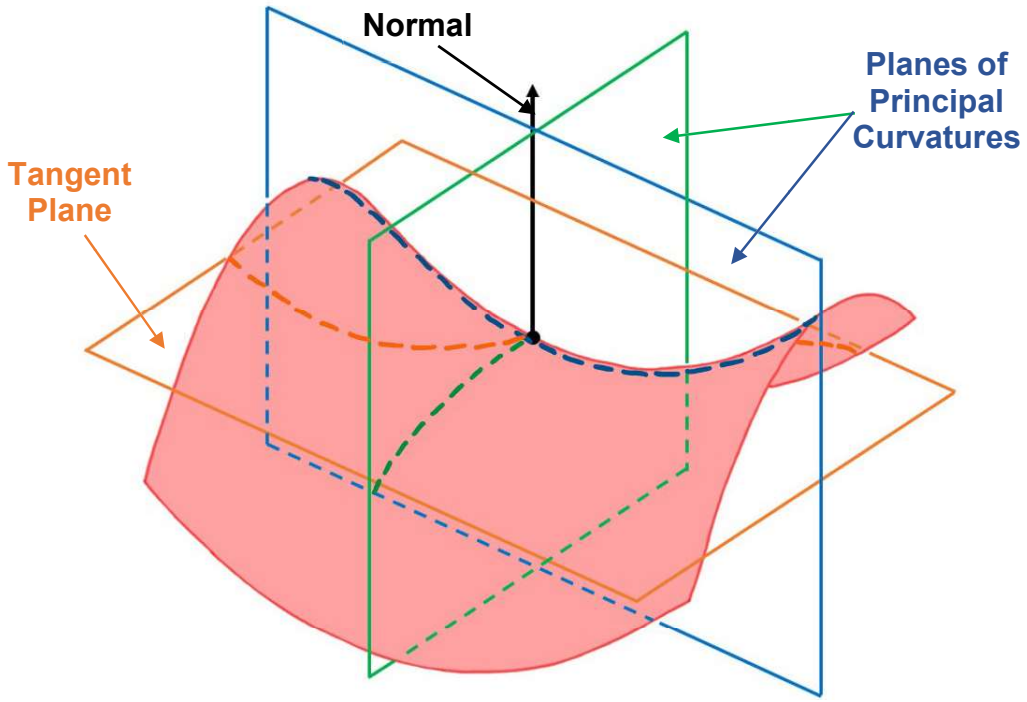

Figure 1-6. Normal and principal curvatures of a surface.

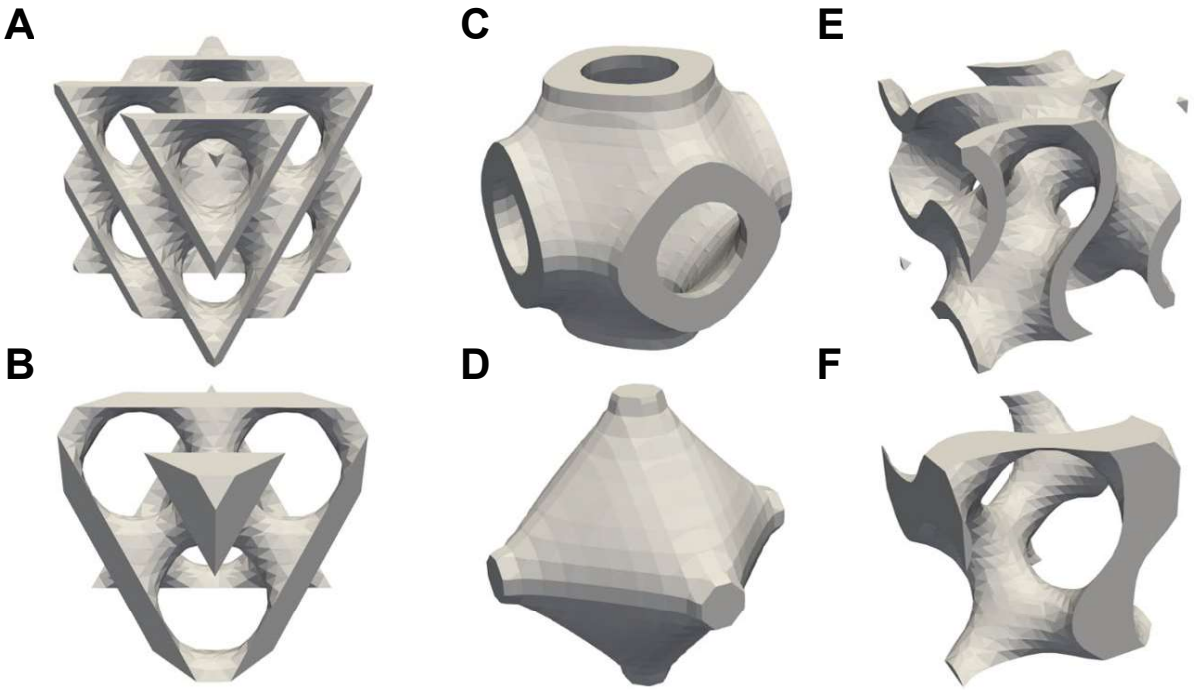

Figure 1-7. The types of TMPS structures. A depiction of the unit cells for A) the sheet-based diamond structure, B) the skeletal-based diamond structure, C) the sheet-based primitive structure, D) the skeletal-based primitive structure, E) the sheet-based gyroid structure, and F) the skeletal-based gyroid structure.

Although the discovery of TPMSs and the exploration of porous structures for implant design occurred several decades ago, the technology to reproduce these structures was not available until more recently. The creation of additive manufacturing began in the 1980's [81]. A surge of research would begin years later exploring the 3D-printing of porous structures, such as TPMSs, for tissue engineering and implant design. TPMSs have low weight to high strength ratios and their porous nature allows for the three-dimensional transportation of cells, nutrients, and potentially antibiotics.

1.6.2 Additive Manufacturing of Porous Structures

Additive manufacturing has allowed for the construction of complex structures, such as TPMSs, that were not possible with previous machining applications. Some of the first additive manufacturing rapid prototyping systems were invented by Hideo Kodama in 1981 [81]. Shortly after, in 1983, stereolithography was invented by Charles Hull. The Stereolithography (STL) file format is still used to today to transfer computer-aided designs (CAD) to 3D printers. Selective Laser Sintering (SLS) was one of the first additive manufacturing techniques, developed in 1986. SLS works by sintering powdered material with a laser to form a desired structure, layer-by-layer [82]. In 1988, Fused Deposition Modeling (FDM), today's most commonly used technique, was invented. FDM works by heating and extruding thermoplastic filaments, however Liu et al. have explored the use of FDM for the 3D-printing of metals [83]. Selective Laser Melting (SLM) is a similar technique to SLS, however the laser completely melts the powder particles before solidification [82]. By completely liquifying the material, complex, thin-walled geometries can be printed at more than 99% densities [84]. With these advancements made in additive manufacturing, there has been a revival of research into TPMSs in the last two decades [85]. There has been a special focus on how effective these 3D-printing processes are at manufacturing these complex structures [86-90] and assessing their mechanical properties through finite element analysis and mechanical testing.

1.6.3 Mechanical Evaluation of TPMS-based Structures

Research regarding the applications of TPMSs has been explored in a variety of fields including computer graphics, manufacturing science, mechanics, thermology, optics, acoustics, chemistry, and biology [91]. Several studies have been conducted to investigate and compare the mechanical properties of TPMSs by 3D-printing them in materials such as maraging steel, graphene foams, and polymers [80,92-93]. Al-Ketan et al. concluded sheet-based TPMSs exhibit superior mechanical properties to their skeletal-based counterparts and that the sheet-based

diamond surface exhibited the greatest mechanical properties compared to several other TPMSs, including the gyroid and primitive surfaces [80]. Jung et al. compared the effects of pore size and porosity amongst the diamond, gyroid, and primitive surfaces [92]. They discovered that for the same spanned area in the unit cell, the primitive surface is the lightest weight whereas the diamond surface is the heaviest. Using a relative density comparison, the diamond surface has the largest Young's modulus and smallest Poisson's ratio. The primitive surface has the smallest Young's modulus and largest Poisson's ratio with the gyroid surface being in between the two. Potentially their most important finding, Jung et al. concluded that the gyroid surface has nearly perfect isotropic elastic properties making it more advantageous with polycrystalline structures compared to the other surfaces. Maskery et al. concluded that although the primitive surface has a significantly higher elastic modulus, it experiences significant deformation [93]. They state, "if the application require that the latticed part undergoes high strain before failure, a gyroid or diamond lattice would be preferred."

In addition to mechanical strength, fluid permeability and mass transfer properties have been studied to compare these TPMSs with each other and other strut-based architectures [94-97]. A preliminary study by Castro et al. concluded that the primitive and gyroid surfaces have more favorable permeabilities for bone applications [94]. Based on these mechanical property, weight, stiffness, elastic behaviour, and fluid permeability comparisons in the current literature, the sheet-based gyroid surface was chosen for further investigation in it's use for orthopaedic implant design.

1.7 Gyroid Structures

Gyroids are found to exist naturally in structures such as butterfly wings [98-99], cell membranes [100], and block copolymers [101-102]. The gyroid surface, both sheet-based and skeletal-based, has been of particular interest in tissue engineering [103-107] and bone implantation [108-110] due to its low-weight to high-strength ratio. Its structure has been studied and determined to be well matched with trabecular bone, making it suitable for such applications [111-112].

As previously mentioned, TPMSs can be defined mathematically. The mathematical equation representing the gyroid surface is:

$$sinXcosY + sinZcosX + sinYcosZ = 0 \qquad \text{(Equation 1-2)}$$

$X = 2\alpha\pi x$, $Y = 2ß\pi y$, and $Z = 2\gamma\pi z$ where α, ß, ɣ are constants relating to the unit cell size in the x, y, z directions, respectively.

This mathematical formula allows for easy modelling and manipulation of this surface. Several studies have been conducted investigating the effect of the gyroid's porosity on its material properties, by altering either pore size, wall thickness, or both [113-117]. Several studies have also explored the effects of porosity gradients throughout gyroid structures [115]. Liu et al. were able to successfully develop TPMS-based scaffolds with cell-size gradients that exhibited superior strength but similar elastic moduli to cortical bone [116]. Wallat et al. took this one step further by developing both linear and non-linear porosity gradients [118]. They concluded that the graded-porosity structures, compared to uniformly porous structures, have greater peak stresses but lower mean normalised stresses. Kelly et al. have performed fatigue testing on gyroids of different porosities, by altering both wall thickness and pore size [119]. While most gyroid testing has been performed with cuboid shapes, Timercan et al. have explored more complex, cylindrical-based shapes, for intervertebral applications [120].

As there are many 3D-printing factors (eg. printing method, printing material, post-printing treatment) and specific geometry parameters (eg. pore size, wall thickness, overall shape) that can affect the mechanical strength of these gyroid structures, further testing of these structures is still required.

1.8 Finite Element Modelling

Before spending the time and resources on the manufacturing of these structures, it is best to perform computer simulations to predict their behaviours. Finite element (FE) analysis allows for the estimation of stresses and strains throughout complex structures. This is done by breaking down (discretizing) these complex structures, into smaller, simple, inter-connected, finite elements [121]. This collection of elements is known as the mesh.

The accuracy of these models is dependent upon multiple factors. One factor is the mesh size. The smaller the elements in the mesh, and therefore the larger the number of elements, the more accurate the results will be. However, there is a trade-off. As a mesh becomes finer, more computational power is required. It is important to find a mesh size that will give accurate results without being unnecessarily time-consuming. This can be done with a mesh convergence analysis. Another factor influencing model accuracy is the element type. Element type is defined by its shape, tetrahedral or hexahedral, and its order, linear or quadratic. Studies have shown that second order elements provide more accurate results whereas linear elements can exhibit stiffer behaviour than experimental results [122].

Within FE modelling software packages, we can assign specific material properties, boundary conditions, and loads to our structures. For biomedical engineering applications, we can mimic complex materials, such as bones, by assigning different material properties to individual elements within a single structure [25]. Then using algebraic equations, we can solve for the desired variables at each of these elements. Resultant data, such as stresses, strains, and displacements, can be obtained and exported from each individual element. This data can then be used to determine important information about the structures, such as stiffness, strength, and strain energy densities, depending on the purpose of the study.

1.9 Project Scope and Objectives

This study aims to contribute to the viability of gyroid structures for porous implant stems. The primary step is to validate the finite element analyses of gyroid structures by comparing their in-silico results to physical experimental results. The next step is a case study of developing shoulder implant stems out of these gyroids structures and implementing them in finite element humerus models. The porous stems are compared to a solid stem to assess their various impacts on the surrounding bone in addition to their structural integrity for permanent implantation.

The main objectives of this study were:

1. To develop finite element models of cylindrical gyroids and perform compression and fatigue testing on them to validate the models.
2. Perform a case study of gyroid humeral implant stems and assess their structural viability, as well as their mechanobiological effects on proximal humeri, using FE modelling.

1.10 Thesis Overview

Chapter 2 describes the process of constructing gyroid cylinder models using computer-aided design, simulating loading on them using finite element modelling, and validating those models with physical testing. Chapter 3 describes the construction of gyroid glenohumeral implant stems, the simulation of them implanted into proximal humeri of different densities and evaluating the effects of this loading on both the stems and the humeri. Chapter 4 summarizes the work, highlighting the strengths and limitations and outlining the future of this work. Supplementary information can be found in the Appendices.

Chapter 2

2 Static Compression and Fatigue Behaviour of Heat-treated Selective Laser Melted Titanium Alloy (Ti6Al4V) Gyroid Cylinders

This chapter describes the process of constructing cylindrical sheet-based gyroid structures using a variety of computer techniques. A comparison of in silico and experimental static compression and fatigue loading on the structures are also discussed.

2.1 Introduction

Triply periodic minimal surfaces (TPMSs) have become of great interest in the fields of mechanics and biomedical engineering, due to their high strength to low weight ratios. Minimal surfaces are described as having zero mean curvature, meaning at any point on their surface the sum of the principal curvatures is equal to zero [79]. The nature of these surfaces reduces the build up of stress concentrations that are produced in other porous structures with sharper angles and corners. TPMSs are not a new topic of study, however traditional manufacturing techniques limited the ability to produce these structures for several decades. An emergence of research regarding TPMSs has arisen in the last 20 years due to the advancements of additive manufacturing.

Additive manufacturing (AM), also known as 3D-printing, has allowed for the production of more complex structures. AM takes a computer-aided design (CAD) model and prints it layer by layer. AM can be used to print objects in a variety of materials from plastic and polymers to metals and ceramics. Different AM techniques are suited for different materials and applications. One AM technique often used for the printing of complex metal structures is Selective Laser Melting (SLM) [84]. SLM works by selectively melting powder particles with a laser to solidify and build the object one cross-section at a time. Many researchers have studied the mechanical properties of 3D-printed TPMS-based structures [80,92-93]. Based on the current research, one TPMS named the gyroid surface, has been of particular interest. The gyroid has almost perfect isotropic elastic properties.

For applications such as orthopaedic implants, it is important that these structures not only have adequate yield strengths, but they also have long fatigue lives. Finite element (FE) modelling is an important modelling technique that allows researchers to analyze and predict the behaviours

of materials at a reduced cost, both financially and time-wise. Although FE modelling is not a novel concept, computer modelling of materials for their fatigue behaviours is less common. The fatigue properties of regularly used materials are less known than their monotonic properties. The manufacturing of these materials, such as selective laser melting, will also affect these properties. A fatigue analysis software called Fe-safe uses Seeger's method to predict the fatigue properties of a material based on its Youngs modulus and ultimate tensile strength [123]. Duan et al. demonstrated that Fe-safe could predict the fatigue life of machined dental implants within a 95% confidence interval of their experimental results [124]. The purpose of this study is to observe the trends of static compression and compression-compression fatigue behaviour across gyroid porosities and validate the in silico predictions with experimental testing.

2.2 Methods

2.2.1 Gyroid Construction

Cylindrical gyroid structures were constructed using computer-aided design. First, a gyroid unit cell was developed mathematically based on Equation 2-1. This unit cell was 6 mm in length, width, and height. Using an opensource creation suite (Blender), the gyroid unit cell was arrayed in all three directions to create a rectangular gyroid prism of size 18mm x 18mm x 42mm. The thickness of the gyroid surface was increased to 0.85, 0.60, 0.45, 0.30 and 0.20 mm. This developed five different structures at 60%, 70%, 80%, 85% and 90% porosities. These porosities are the metal-void volume percentages of the corresponding solid geometry. A Boolean operation was then performed between each gyroid rectangular prism and a solid cylinder (17mm in diameter, 40mm in height) to construct the gyroid cylinders as shown in Figure 2-1. These cylinders will be referred to as 60P, 70P, 80P, 85P, and 90P for the remainder of this chapter.

$$sinXcosY + sinZcosX + sinYcosZ = 0 \qquad \text{(Equation 2-1)}$$

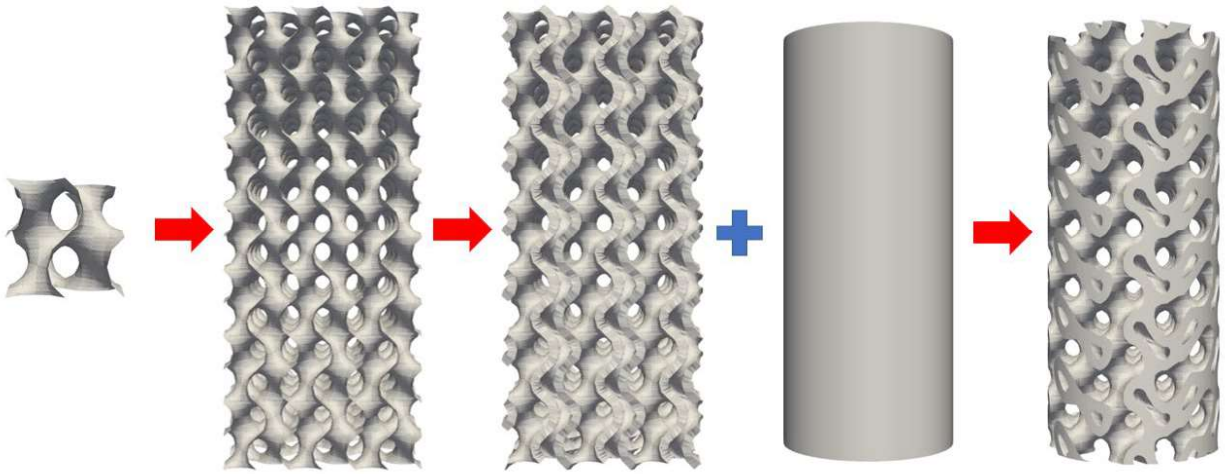

Figure 2-1. Development of the gyroid cylinder. Gyroid unit cell is translated in all three cartesian directions and the resultant surface is thickened to obtain the desired porosity. A Boolean operation is then performed between the thickened gyroid structure and a cylinder to develop the gyroid cylinder.

In order to analyze these structures in the FE software (Abaqus), surface optimization was required. First, a stereolithography (STL) file of the gyroid cylinder was exported from blender. A binary rasterization code was developed to create a binary image volume representation of the gyroid cylinder in a MetaImage (mha) format. An isosurface extraction was then performed on each MetaImage to generate a new surface triangulation (Microview). Surface improvements were performed to smooth any edges and trim the ends to ensure they were perfectly flat (Geomagic). A high-quality mesh was then created (Netgen) before importing the structures into the finite element modeling software (Abaqus). Meshing parameters are shown in Appendix 5.1. Two meshes of each cylinder were developed which consisted of a) linear tetrahedral elements (C3D4) and b) quadrilateral tetrahedral elements (C3D10). The number of elements increased as porosity decreased and ranged from approximately 1.3 million to 4.0 million elements.

2.2.2 3D Printing

A metal 3D printer (Renishaw AM400), was used at the Additive Design in Surgical Solutions (ADEISS) Centre at Western University, which is an ISO 13485 compliant company. The gyroid cylinders were printed in medical grade titanium (Ti-6Al-4V) using selective laser melting (laser power: 200-400W, scanning speed: 10,000-20,000 points/second, particle diameter: 15-45 microns, spot size: 70 microns) and underwent heat treatment (24-hour cycle of stress relief, 850 °C for 1 hour then passive cool down). Five specimens were printed for the 70P, 80P, 85P and six specimens were printed for the 60P and 90P. The actual porosities were determined from the

masses of the printed specimens. A density of 4.28 g/cm was assumed for the 3D-printed titanium and confirmed by the mass of a printed solid part [125].

End caps were added to both sides of each cylindrical gyroid specimen for 3D printing, as shown in Figure 2-2. The bottom surface of these end caps was perfectly flat where they connect with the flat gyroid ends. They consisted of a 4 mm thick cylindrical region with a shallow cone to ensure an equal application of force across the cross-section of the cylinder as well as providing a location for mark placements for the strain measurement (explained further in 2.2.3).

Figure 2-2. CAD models of the gyroid cylinders with end caps developed for the experimental testing. Left: 60P. Right: 90P.

2.2.3 Static Compression Testing

A static compression test was performed on each porosity (N=1) at a displacement rate of 0.3mm/min, in accordance with ISO 13314 [126], to determine the apparent modulus of elasticity and yield strengths of each structure. The specimens were loaded to 10 kN or until catastrophic failure. Three 60P specimens underwent these tests to assess repeatability. A video extensometer was used to measure the overall strain in the specimens from a white paint circle placed on each endcap, shown in Figure 2-3. Further explanation of the video extensometer calibration and validation can be found in Appendix 5.2. The apparent modulus of elasticity was determined using Equations 2-1 to 2-3, to compare the stiffness of the experimental tests to the computational models.

$$\sigma = \frac{F}{A_c} \quad \text{(Equation 2-2)}$$

$$\varepsilon = ln\left(\frac{L}{L_o}\right) \quad \text{(Equation 2-3)}$$

$$E = \frac{\sigma}{\varepsilon} \quad \text{(Equation 2-4)}$$

σ is the apparent stress, F is the applied force, A_c is the surface area of the cross section of a 17mm cylinder (diameter of the gyroid cylinders), ε is the overall axial strain measured from the video extensometer, L is the length between tracking marks, L_o is the original length between tracking marks, and E is the apparent modulus of elasticity. The apparent modulus of elasticity was the chosen measurement because the purpose of this study is not to analyze the strength and stiffness of the 3D-printed titanium but to compare each of the porous gyroid fill structures as a metamaterial.

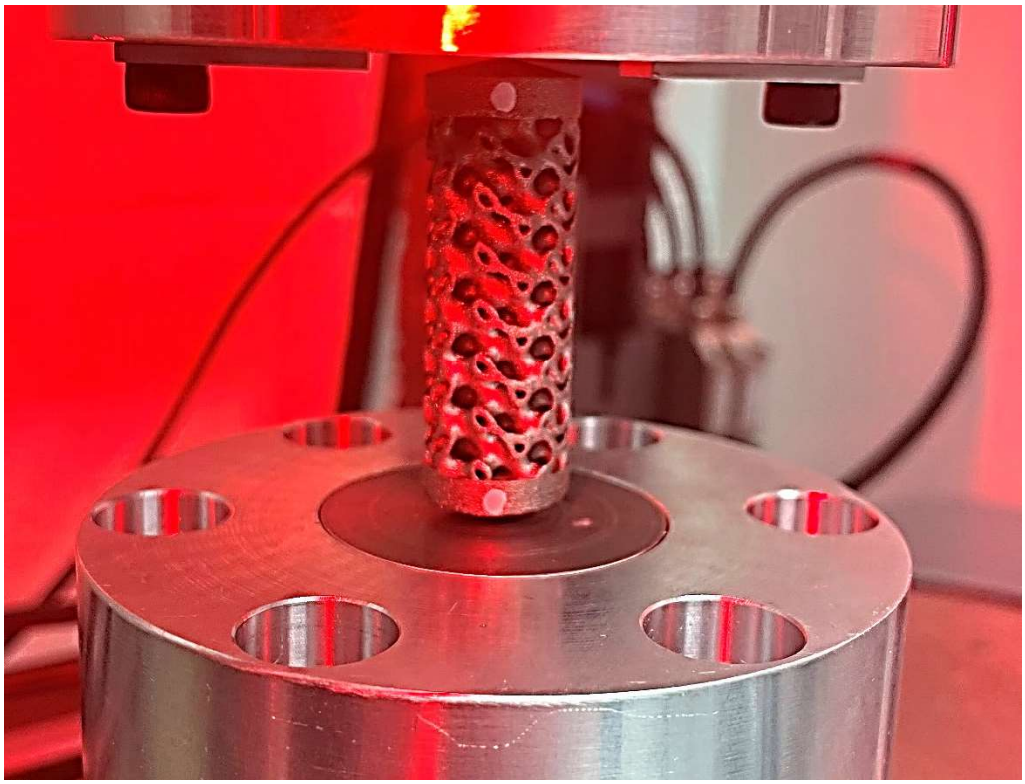

Figure 2-3. Gyroid testing configuration for static compression tests. White marks on each end of gyroid were tracked by the video extensometer to measure the overall strain of the specimen in real time.

2.2.4 Fatigue Testing

Compression-compression fatigue tests were performed (frequency: 10 Hz, sinusoidal waveform, loading ratio: 0.1). One specimen was tested per loading cycle to obtain a fatigue life curve for each gyroid porosity. The maximum loads were chosen as 50%, 70%, 80%, and 90% of the yield force. Due to the limited capability of the Instron, the 70P specimens were tested at maximum loads of 50%, 65%, 70%, and 75% of their yield force. The tests were stopped when a million cycles were reached, or catastrophic failure occurred. The 60P specimens (N=3) were tested at the same maximum load of ~45% of its yield force. The 60P specimens were not stopped at a million cycles but continued until catastrophic failure occurred.

2.2.5 Finite Element Modeling

In Abaqus, the gyroid cylinders were assumed to be made of titanium (Ti-6Al-4V) by assigning the material a Young's modulus of 110 GPa and a Poisson's ratio of 0.34 [24,127]. Plasticity was considered by defining the yield strength of Ti-6Al-4V as 880 MPa [128]. A reference point was created 5 mm from the center of each cylinder end. All the nodes on the bottom surface of the cylinders were connected to the closest reference point via kinematic coupling (Figure 2-4). The reference point was then constrained in all degrees of freedom. All the nodes on the top surface were connected to the closest reference point via kinematic coupling. A 10kN load was applied to the reference point to be evenly distributed across the top surface of the gyroid.

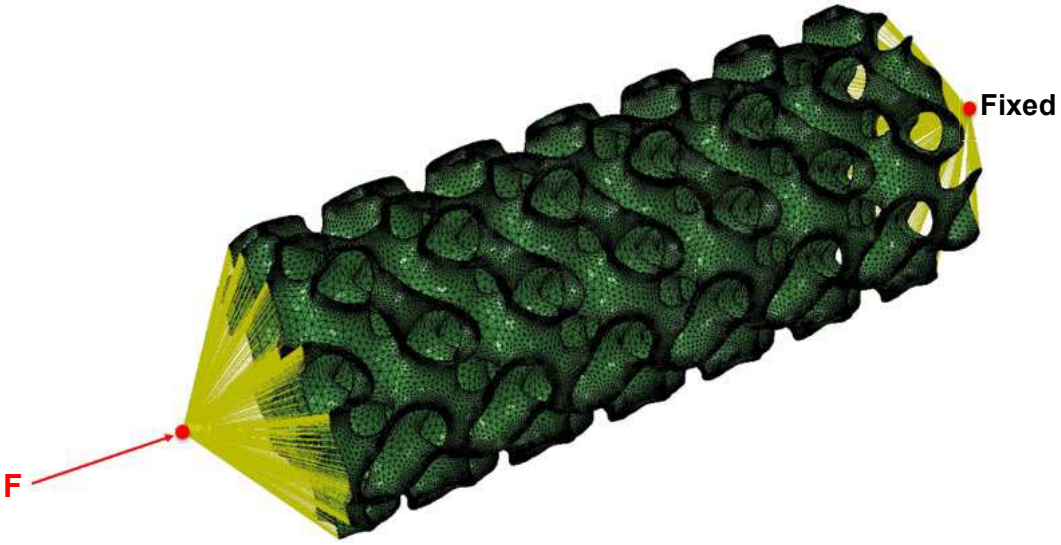

Figure 2-4. Constraints, boundary conditions, and loads applied to the gyroid cylinder structures. A reference point located in the center of each cylinder end was constrained to all the points on their respective surfaces. One reference point was constrained in all degrees of freedom. The opposite reference point had a concentrated force of 10kN applied to it which is distributed across all connected nodes.

The FE model results were loaded into a compatible fatigue analysis software (Fe-safe) which reads the resultant stresses and strains on the structure. Although it can typically be assumed that a structure will fail where the maximum stresses are occurring, Fe-safe can provide contours of several fatigue parameters such as predicted fatigue lives or probability of failure under a defined number of cycles. Fatigue analyses are more complex than simple static analyses, as they require more material specific parameters, known as fatigue parameters. The fatigue parameters of certain materials, such as SLM Ti6Al4V, are not well known. Fe-safe can approximate the fatigue properties (Table 2-1) from its ultimate tensile strength (UTS) and Young's modulus, using Seeger's method [123]. The surface finish was also considered by defining the Roughness Average (Ra) to be between 1.6μm and 4μm, aligning with reported

values for grit-blasted Ti6Al4V [129]. The Fe-safe process used is described in further detail in Appendix 5.3.

The same loading scenarios were analysed in the virtual fatigue tests as the experimental tests described in 2.2.4. The applied loads in the models were increased based on the experimental static compression results to mimic the actual deformation and strain that the gyroid cylinders experienced. The fatigue strength coefficient (sf') was altered from the Seeger's approximation to align the computational results of the 80P gyroid, at the 80% of yield force maximum loading scenario, with the experimental results. This new sf' was used for each fatigue life analysis scenario to assess the agreement between in silico and experimental results. Failure was determined as the lowest predicted fatigue life within the internal struts of the gyroid cylinders, as failure of the external struts along the outer surface of the cylinder would not produce catastrophic failure.

Table 2-1. Fatigue parameters estimated by Fe-safe using Seeger's method before calibration.

Fatigue Parameter	Symbol	Estimated Value
Cyclic strain hardening coefficient	K'	1529.5 MPa
Cyclic strain hardening exponent	n'	0.11
Basquin's fatigue strength exponent	b	-0.095
Coffin-Manson fatigue ductility exponent	c	-0.69
Fatigue ductility coefficient	Ef'	0.35
Fatigue strength coefficient	sf'	1586.5 MPa

2.3 Results

2.3.1 3D Printing

The 3D-printing of these porous structures produced slightly more porous than intended specimens. The nominal porosities and actual printed porosities can be found in Table 2-2. These porosities were calculated based on the average mass of the specimens for each porosity group.

Table 2-2. Average porosity of 3D-printed specimens compared to the nominal porosity. Nominal porosity refers to the porosity of the gyroid if there were zero internal porosity based on the volume of the CAD models. Actual porosity refers to the average porosity of all the specimens in each porosity grouping, based on their masses and the assumption that the endcaps on each end of the gyroids were 100% solid.

Porosity Label	60P	70P	80P	85P	90P
Nominal Porosity	60.7%	70.5%	79.8%	84.8%	89.8%
Actual Porosity	64.2%	74.0%	82.9%	87.8%	92.4%

The 85P and 90P cylinders had visible defects at the top boundary between the gyroid structure and the end cap (See Figure 2-5). Electron beam machining was performed to slice off the top 3mm of the gyroid and the top endcaps on these specimens. A new end cap was manufactured that the cut surface could fit into. A finalized printed specimen from each porosity group can be seen in Figure 2-6.

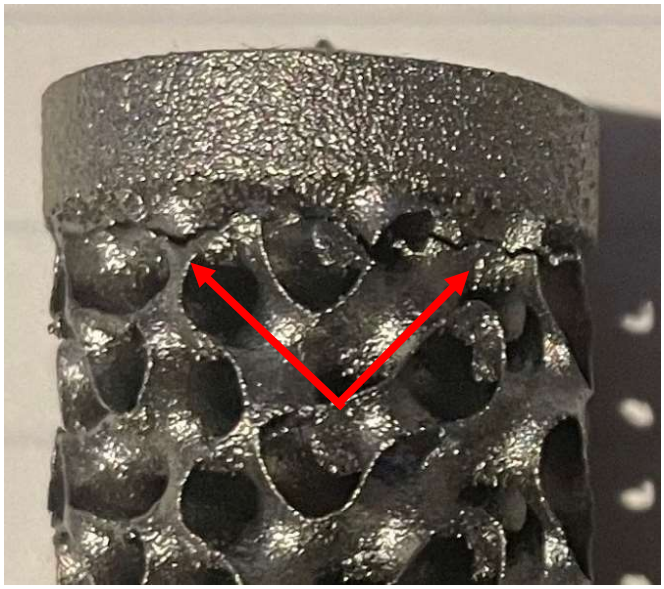

Figure 2-5. Picture of the cracks developed in a 90P specimen.

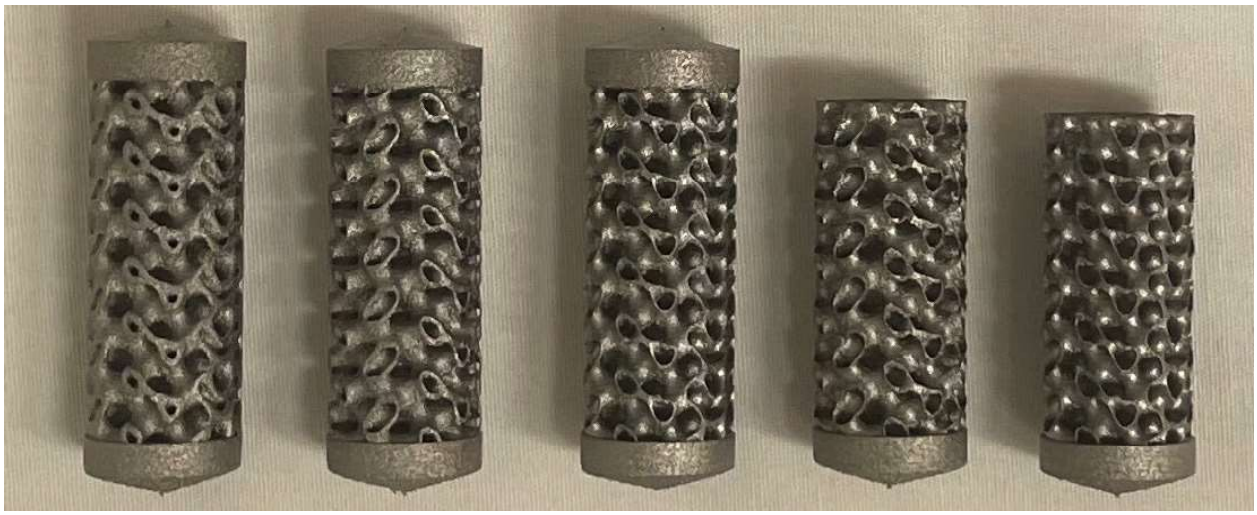

Figure 2-6. One specimen of each of the gyroid cylinders. From left to right: 60P, 70P, 80P, 85P, 90P.

2.3.2 Static Compression Testing

The apparent modulus of elasticity for each porosity level was determined from the linear region of apparent stress vs. strain curves (See Appendix 5.5). The apparent modulus of elasticity was

determined in the same manner for the finite element models and a comparison of these values for each porosity can be found in Figure 2-7.

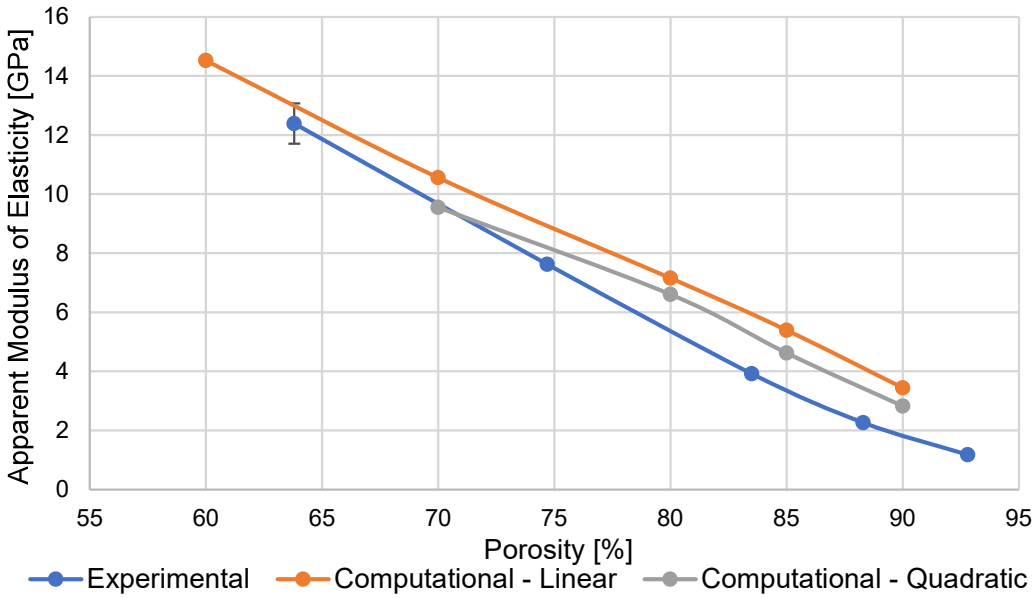

Figure 2-7. Comparison of the apparent modulus of elasticity versus porosity between the computational models (linear and quadratic elements) and the experimental results. Due to limited computational capabilities, the computational model of the 60P specimen with quadrilateral elements could not be analysed. Error bars represent the standard deviation for the 60P specimens (N=3). All other porosities were tested with one sample.

The repeatability of the static compression tests was analyzed using three 60P specimens which resulted in apparent moduli of elasticity of 11.83 GPa, 11.98 GPa, and 13.35 GPa (See Figure 2-8).

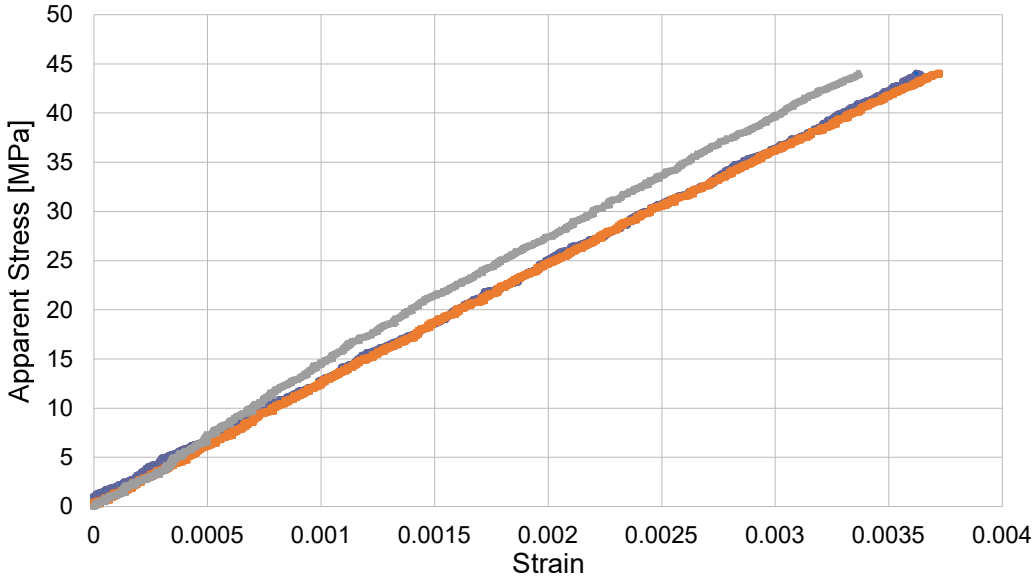

Figure 2-8. Apparent stress versus strain for the static compression tests of the 60P specimens. Each colour represents a different specimen. The Apparent modulus of elasticity (slope of the lines) are 11.83 GPa, 11.98 GPa, and 13.35 GPa.

2.3.3 Fatigue Testing

The fatigue lives of the specimens were defined by the number of cycles to catastrophic failure. Each specimen had a smooth increase in deformation, with less than 0.1% overall strain, before catastrophic failure occurred. Images of the tested specimens can be found in Appendix 5.6. The maximum apparent stresses are plotted against the predicted and experimental fatigue lives for all the specimens in Figure 2-9. When using the FE models to predict the fatigue lives of the specimens, the number of cycles to failure was consistently overpredicted with each scenario predicting over a million cycles. As shown in Section 2.3.2, the FE models were predicting the gyroids to be stiffer than exhibited by the experimental tests. Considering this difference, the loads applied to the FE models were increased to match the overall deformation of the gyroids instead of applied loads. After scaling these loads, the fatigue strength coefficient (sf') was adjusted until the 80P specimen (at a maximum load of 80% yield force) had a fatigue life prediction within 20,000 cycles of the experimental results. The 80P specimen was predicted to fail at 522396 cycles (experimental life: 503249 cycles) when sf' was lowered to 1225 MPa from 1586.5 MPa. This new sf' of 1225 MPa was used for the fatigue life prediction of all the fatigue loading scenarios which can be seen in Figure 2-9.

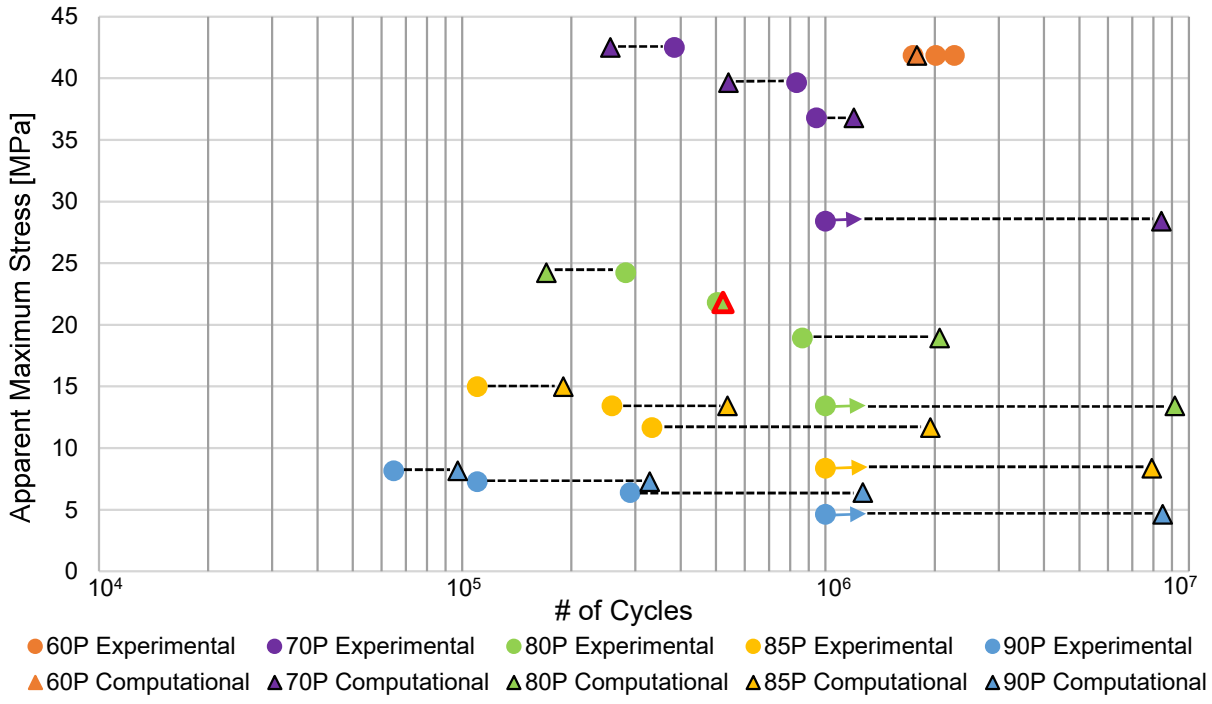

Figure 2-9. S-N diagram of the experimental fatigue tests. Apparent stress refers to the maximum loading divided by the cross-section of a 17mm diameter cylinder. Arrows represent specimens which were stopped at 10^6 cycles. The triangle outlined in red represents the computational specimen used to determine a new sf' value.

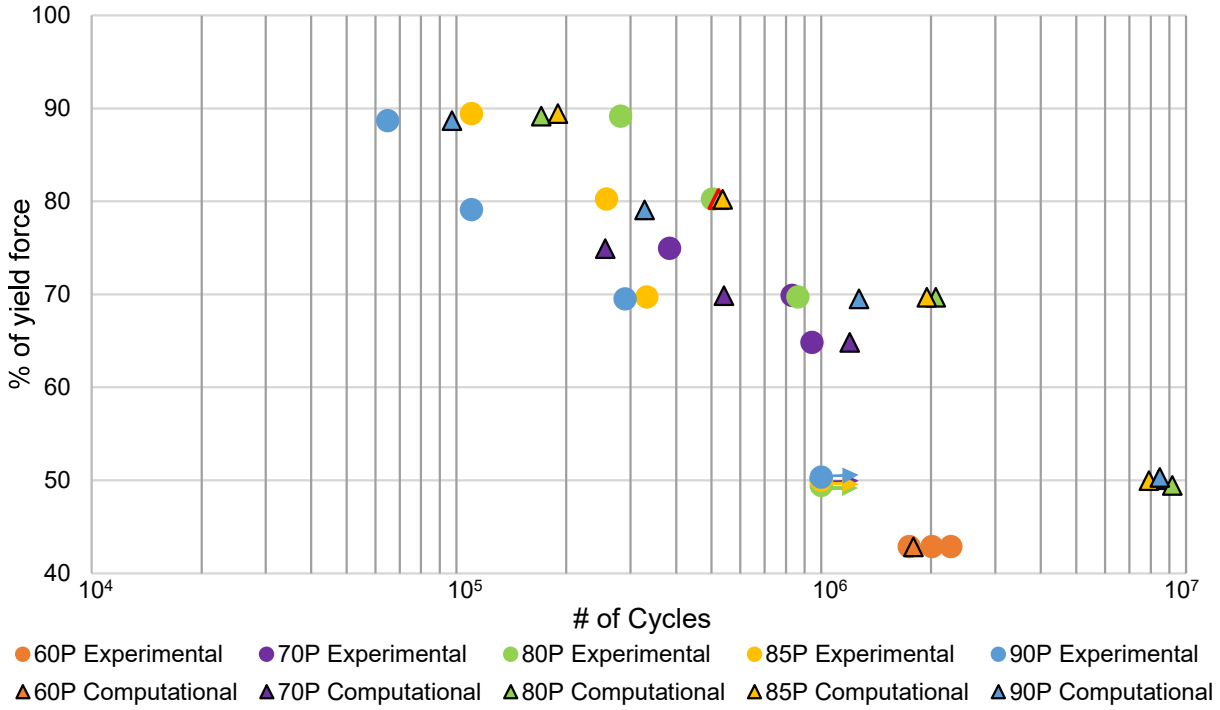

Figure 2-10. Maximum loading as a percentage of yield force versus the number of cycles to catastrophic failure. Arrows represent specimens that exceeded 10^6 cycles. The triangle outlined in red represents the computational specimen used to determine a new sf' value.

As gyroid porosity increased, the number of cycles to failure at the same percentage of their yield force decreased as shown in Figure 2-10. A better agreement was observed between predicted and actual fatigue lives as stem porosity decreased.

2.4 Discussion

The purpose of this study was to observe trends and compare the in silico and experimental results of static compression and compression-compression fatigue testing on cylindrical gyroid structures. The SLM printed gyroid structures were found to be 2.6%-3.5% more porous than designed in the computational models, based on their masses. This can be an indication of potential printing non-idealities such as internal voids and/or thinner walls produced than intended. There was a difference of an apparent modulus of elasticity of 1.52 GPa between the 60P specimens during the experimental static compression tests. This demonstrates that the stiffness of these gyroids is highly sensitive to the printing defects that are present. The walls of these 60P gyroids are thin (0.85mm) which is understandable why they are so sensitive to the potential defects. As shown in Figure 2-11, the printing tolerances of the 3D printer will have a bigger impact on thin-walled structures. The only difference between the gyroid cylinders in this study are the thicknesses of their walls. As the walls get thinner, the ratio between the nominal

thickness and actual printed thickness gets larger, leading to larger discrepancies between the computational models and experimental results.

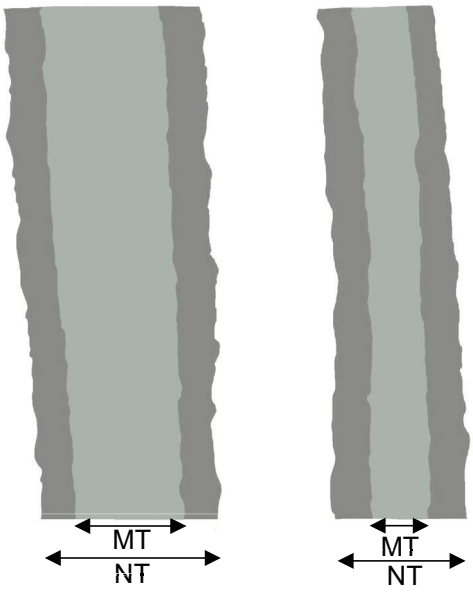

Figure 2-11. Depiction of the ratio of the minimum thickness printed (MT) and the nominal (intended) thickness (NT). As the nominal walls get thinner, the ratio of minimum thickness to nominal thickness gets larger. The darker grey outer region is where the material is not 100% consolidated meaning the wall thickness will have some variations throughout the structure.

Another issue encountered with the printing of these specimens were the cracks developed at the top edge of the 85P and 90P specimens. The harsh transition from the highly porous gyroid to the solid endcap left it vulnerable to crack initiation during printing. In future studies, it is important to take better note of this transition between the gyroids and solid structures when the build requires the highly porous structure to support a solid one. If this scenario were required, a decreasing porosity gradient leading into the solid structure could help prevent crack initiation.

The linear and quadratic computational models predicted, on average, 2.74 ± 0.45 GPa and 2.15 ± 0.40 GPa higher apparent moduli of elasticity for the gyroids than demonstrated by the experimental tests, respectively. The difference between the in silico and experimental results can be attributed to the difference between nominal and actual porosities. By using the quadrilateral elements versus the linear elements, there was a slight change in the apparent modulus of elasticity in favour of the experimental results. This was expected, as second-order tetrahedral elements have been shown to provide more accurate results than first-order elements in the literature [122]. The trade-off with using quadrilateral elements for complex geometries with fine meshes is they take significantly more computing power. Although the FE models showed

the gyroids to be stiffer than in reality, the curve comparing porosity with apparent elastic moduli were similar to the experimental results, further demonstrating that the discrepancy can be attributed to the printing non-idealities.

The S-N curves got steeper as gyroid porosity increased, meaning the fatigue life was more sensitive to the applied loads as the walls of the gyroid got thinner. To get a better idea of how sensitive the gyroid porosity is to the applied loads, the fatigue lives were plotted against the apparent stress as a percentage of the yield stress. There was a consistent trend that for the same percentage of their yield stress, an increase in gyroid porosity caused the gyroid to fail at fewer load cycles. This could be attributed to the higher porosity gyroids being more sensitive to printing non-idealities, as they have thinner walls. On average, the predicted fatigue lives were within 54% of the experimental fatigue lives. A limitation of this study is the porosity of the gyroids were only altered by changing the thickness of their walls. Another method to altering the gyroid porosity would be to change the size of the unit cell. If this study were conducted again with a fixed wall thickness and an alteration of unit cell size to obtain desired porosities, it is possible there would be a better agreement between the gyroids fatigue lives and their apparent stress as a percentage of their yield strength.

A previous study by Duan et al. was able to demonstrate Fe-safe fatigue life predictions within a 95% confidence interval [124]. The main differences between their study and this one is the manufacturing and geometry of the specimens. The additive manufacturing of the specimens in this study causes a change in fatigue parameters not accounted for in Fe-safe. Even with the calibration of the fatigue strength coefficient, there was not a great agreement between the fatigue life predictions and the experimental fatigue lives. There was a trend of better agreement with the lower cycle fatigue compared to the higher cycle fatigue for all gyroid porosities (with the exception of the 60P specimen which had very good agreement at high-cycle fatigue). There was a better agreement between actual and theoretical fatigue lives as porosity decreased. The complex geometry of the gyroid could also contribute to these differences. Unlike a simple geometry, it is impossible to determine the exact location of crack initiation on the gyroid cylinder from the experimental tests. It was assumed in the computational models that the any cracks initiated on the struts on the outer perimeter of the cylinder would not cause catastrophic failure and were therefore ignored in the fatigue life predictions.

2.5 Conclusion

Overall, the computational models were able to provide similar trends to the experimental results. Although the FE models did not provide accurate static and fatigue results, they were still able to provide a good relationship of the five different stem porosities. Most of the discrepancies in this study can be attributed to the manufacturing of the specimens. The static compression testing provided important data to calibrate the virtual fatigue tests, which helped close the gap between predicted and actual fatigue lives of the specimens. Further calibration of the fatigue parameters could probably improve the fatigue life predictions and should be explored. Due to the geometry of these specimens, defining when failure will occur in the virtual models was difficult and therefore most likely added to the disparities between in silico and experimental results. Future work should explore the effects of different printing parameters and gyroid configurations (e.g., different pore size) to obtain a better agreement between nominal and actual porosities and therefore better agreement between computational and experimental results.

Chapter 3

3 Mechanical Analysis of Porous versus Solid Shoulder Implants in Humeri of Different Bone Densities

This chapter demonstrates the construction of a gyroid-based humeral implant stem and the exploration of its mechanical properties and mechanobiological impact on proximal humeri, using finite element modeling.

3.1 Introduction

As described in Chapter 1, orthopaedic device-related infection (ODRI) can be a serious complication of shoulder arthroplasty. Approximately 2% of primary and 4% of revision shoulder arthroplasties will become infected [130]. When ODRI occurs, the current gold standard is to replace the implant with a two-staged revision surgery, however there are several disadvantages to these procedures. Two-staged revision surgeries involve one surgery to remove the infected implant and replace it with a temporary spacer loaded with antibiotics and a second surgery to reimplant a new permanent device. Polymethyl methacrylate (PMMA), the material typically used for temporary spacers, is not an ideal carrier for antibiotic delivery. PMMA is a dense, non-resorbing, acrylic which can only elude antibiotics from its surface and pores [7]. This results in only around 10% of the loaded antibiotics being eluded into the patient [8]. As well, the drug-release timeline can make the patient susceptible to antibiotic resistance and bacteria growth on the implant [64]. One way to improve this antibiotic delivery after ODRI is to use resorbable drug carriers, such as calcium sulfate [8,66-67]. Resorbable carriers will fully resorb over time, delivering the antibiotics over a longer period of time at a more consistent rate than PMMA. As well, if a permanent implant scaffold was used to house these resorbable drug carriers, then no material removal and replacement would be required in a second surgery. The development of a permanent porous implant that could be employed in that first surgery could reduce the two-staged process to one-stage.

A porous implant would need to have the mechanical strength to withstand physiologically relevant loads as well as an infinite fatigue life. One structure which has become of recent interest in the fields of biomedical and tissue engineering is the gyroid, which was investigated in Chapter 2. The gyroid, discovered by Alan Schoen in 1970, is a triply periodic minimal surface (TPMS).

TPMSs have zero mean curvature which means the mean curvature at every point on the surface is equal to zero. Unlike some other TPMSs, gyroids have nearly perfect isotropic properties [60]. Although these complex structures are difficult to replicate with traditional machining techniques, the development of additive manufacturing has made the production of gyroids quite simple [115,119]. In fact, their constant curvature and self-supporting nature minimizes the waste material during printing.

Another benefit to using a porous structure for implant design is the potential to mitigate stress shielding. Stress shielding has been a major problem with orthopaedic implants for their entire existence and researchers are constantly searching for ways to reduce/prevent it. Razfar et al. compared the impact of stemless, short-stemmed and standard stem humeral implants on bone mechanobiology [24]. Aibinder et al. [28] and Denard et al. [30] have also analyzed the use of stemless and short stemmed implants, respectively. Soltanmohammadi et al. explored the use of hollow stems instead of solid [25]. Denard et al. investigated the stress shielding effects between press-fit and cemented fixation for reverse shoulder arthroplasty [26]. Kim et al. concluded lower filling ratios reduce stress shielding in reverse shoulder arthroplasty [27]. Tan et al. examined the use of a proximal porous coating on the humeral stem [131].

The objective of this study is to evaluate the mechanical viability of gyroid humeral implant stems using finite element modeling (FEM). Although mitigating stress shielding effects is not the main goal of this study, the impact that porous gyroid stems would have on stress shielding and bone mechanobiology is still important to explore. It is hypothesized that the reduced stiffness of the porous stems will reduce stress shielding effects on the surrounding bone. The significance of this study is to combat orthopaedic implant infection and potentially reduce two-staged revision surgeries to one surgery.

3.2 Methods

3.2.1 Humeral Stem Construction

Humeral implant stems were constructed using sheet-based gyroid structures, as described in Chapter 2. A gyroid unit cell (6mm x 6mm x 6mm) was arrayed in all three directions to create a cuboid structure (30mm x 30mm x 78mm). The walls of the gyroid were thickened to 0.85 mm, 0.60 mm, and 0.45 mm to obtain porosities of 60%, 70%, and 80% (referred from here as G60, G70, and G80, respectively). A Boolean operation was then performed with a shortened humeral stem (~70 mm in length) to obtain the gyroid stems, as shown in Figure 3-1.

Due to surface mesh problems caused by the Boolean operation, the resultant stems were not compatible with the finite element (FE) analysis software (Abaqus). Before performing FE analyses, the gyroid humerus stems needed to undergo several preparation steps. First, a binary rasterization code was used to develop a binary image volume representation of each structure. The image volumes underwent an isosurface extraction (Microview), generating new surface triangulations. Surface smoothing and enhancements were performed to create the final gyroid humerus structures (Geomagic). Lastly, a high-quality surface and volume mesh was created (Netgen). These meshing parameters can be found in Appendix 5.1. The meshed parts were imported into the FE software for analysis (Abaqus). The stems consisted of approximately 800,000 to 1,500,000 linear tetrahedral elements. The gyroid stems were assumed to be made of 3D-printed titanium alloy (Ti-6Al-4V) with grit-blasted surfaces, which has a Young's modulus of 110 GPa and a poisson's ratio of 0.34 [24,127].

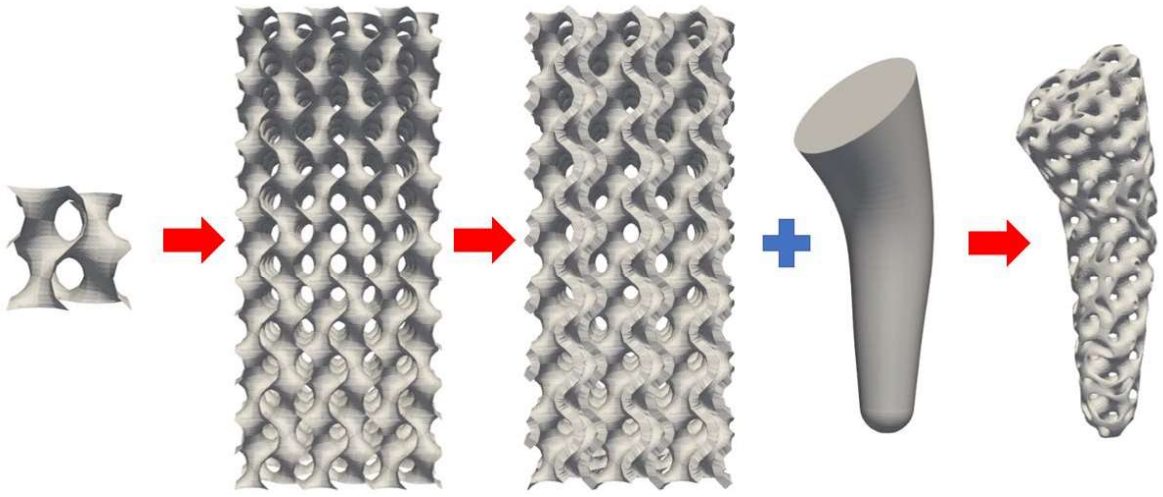

Figure 3-1. Process of constructing the gyroid glenohumeral stem. Gyroid unit cell is translated in all three cartesian directions and the resultant surface is thickened to obtain the desired porosity. A Boolean operation is then performed between the thickened gyroid structure and a solid glenohumeral stem to develop the gyroid stem.

3.2.2 Humerus Models

Statistical shape and density models were created to develop one humerus shape based on computed tomography (CT) scans of 75 cadaveric shoulders (57 males and 17 females, 54 donors, 73 +/- 13 years) in a previous study [132]. Three bone densities were created to represent a healthy, an osteopenic, and an osteoporotic humerus. The Young's moduli (E) of the bones were assigned on an element-by-element basis, with a minimum allowable E of 15 MPa. The humeral heads of each specimen were virtually osteotomized and the medullary cavities were reamed in the proximal humerus for stem placement [25]. Each bone mesh consisted of

approximately 300,000 linear tetrahedral elements with an average edge length of 1.5 mm. Identical meshes were created between intact and reconstructed humeri to allow for element-by-element comparisons. The G60, G70, and G80 stems, and a solid stem were virtually implanted into all the reconstructed proximal humeri models, as shown in Figure 3-2, by manual placement. Each stem type is in the exact location across the different bone densities and for all the loading conditions.

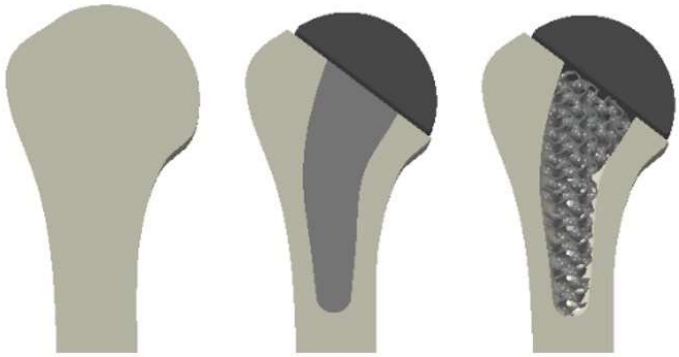

Figure 3-2. Intact bone (left), reconstructed bone with solid implant (middle) and reconstructed bone with 80p stem (right). Reconstructed bones have identical humeral head components.

3.2.3 Loading Conditions

A frictional coefficient of 0.63 was assigned to represent the frictional force between the humerus and the grit-blasted stems [133]. The distal end of each humerus was constrained in all degrees of freedom, as shown in Figure 3-3. Contact forces and frictional moments were reported from a single patient, in vivo study by Bergman et al. [134], as a percentage of the patient's body weight. The resultant forces and frictional moments used in this study (Table 3-1) were calculated from the average weight of donors (63.5 kg) used in the statistical shape and density models, as discussed in Section 3.2.2.

Table 3-1. Resultant forces and frictional moments applied to the humerus during four different loading scenarios. All forces are in N. All moments are in N·mm.

Arm Position	F_x	F_y	F_z	F_{net}	M_x	M_y	M_z	M_{net}
45° of Abduction	130.8	-274.1	99.7	319.6	1370.5	1183.6	872.1	2009.9
75° of Abduction	211.8	-461.0	155.7	530.7	1806.5	1681.9	1495.0	2885.7
90° of Flexion	193.1	-417.4	143.3	481.7	809.8	498.3	-747.5	1209.5
120° of Flexion	317.7	-666.5	230.5	773.5	1868.8	1370.5	2242.6	3224.9

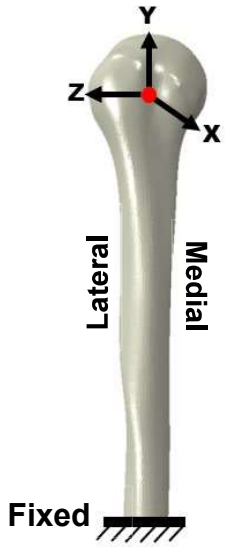

Figure 3-3. Coordinate system for the proximal humeri and boundary conditions applied to distal end. The x-axis runs in the posterior/anterior directions. The y-axis runs longitudinal along the middle of the humerus. The z-axis runs in the lateral/medial directions.

3.2.4 Stem Viability

The viability of these porous stems was assessed by looking at the Von Mises stress distributions under each of the loading conditions and comparing them to the yield strength (880 MPa) of Ti6Al4V [128]. A virtual fatigue life assessment was also conducted to determine the amount of cyclic loading these structures could withstand at each of the loading scenarios (Fe-safe). Fe-safe reads the stresses and strains from the FE analyses and can provide contours of multiple fatigue-related results such as the predicted number of cycles until failure or probability of failure at a provided number of cycles. Unlike the monotonic properties for commonly used materials, such as Ti6Al4V, the fatigue properties of these materials are less known. Fe-safe uses Seeger's method to estimate the fatigue parameters of a material from a provided Young's modulus and ultimate tensile strength (UTS) [123]. Along with providing these two monotonic properties, the surface finish is defined by selecting a range of Roughness Averages (Ra). For the case of grit-blasted Ti6Al4V, the surface finish was defined to be in the range of 1.6 μm < Ra < 4 μm [129].

3.2.5 Bone Mechanobiology Measures

Using the resultant stresses and strains at each of the bone elements, three different measures were used to determine the mechanobiological impact these porous stems have on the bones. The first measure was the volume-weighted average change in the magnitude of von Mises stress

of the bone following reconstruction with respect to the intact state ($\Delta\sigma_{VWA}$), represented by Equations 3-1 to 3-3.

$$\Delta\sigma_{VWA} = \frac{\sum(\Delta\sigma_{VM1}) \times Volume_{Reconstructed\ Element}}{\sum(\Delta\sigma_{VM})_{Intact} \times Volume_{Reconstructed\ Element}} \times 100 \quad \textit{(Equation 3-1)}$$

$$\Delta\sigma_{VM1} = (\sigma_{VM})_{Reconstructed} - (\sigma_{VM})_{Intact} \quad \textit{(Equation 3-2)}$$

$$\sigma_{VM} = \sqrt{0.5 \times \left[\left(\sigma_{xx} - \sigma_{yy}\right)^2 + \left(\sigma_{yy} - \sigma_{zz}\right)^2 + (\sigma_{zz} - \sigma_{xx})^2 + 6 \times \left(\sigma_{xy}^2 + \sigma_{yz}^2 + \sigma_{zx}^2\right)\right]} \quad \textit{(Equation 3-3)}$$

The second measure is the volume-weighted average deviatoric component of the change in stress tensor with respect to the intact state (ΔS), represented by Equations 3-4 to 3-6.

$$\Delta S = \frac{\sum(\Delta\sigma_{VM2}) \times Volume_{Reconstructed\ Element}}{\sum(\Delta\sigma_{VM})_{Intact} \times Volume_{Reconstructed\ Element}} \times 100 \quad \textit{(Equation 3-4)}$$

$$\Delta\sigma_{VM2} = \sqrt{0.5 \times \left[\left(\Delta\sigma_{xx} - \Delta\sigma_{yy}\right)^2 + \left(\Delta\sigma_{yy} - \Delta\sigma_{zz}\right)^2 + (\Delta\sigma_{zz} - \Delta\sigma_{xx})^2 + 6 \times \left(\Delta\sigma_{xy}^2 + \Delta\sigma_{yz}^2 + \Delta\sigma_{zx}^2\right)\right]} \quad \textit{(Equation 3-5)}$$

$$\Delta\sigma_{ij} = \left(\sigma_{ij}\right)_{Reconstructed} - \left(\sigma_{ij}\right)_{Intact} \quad \textit{(Equation 3-6)}$$

Where i and j = x, y, z.

The last measure is the volume percentage of bone that has the potential for bone formation/resorption based on the strain energy density (SED) of each element, represented by Equation 3-7. If the SED of the reconstructed element is more than 55% above/below the SED of the respective element in the intact state, then that bone element is considered to have the potential for bone formation/resorption [25,127,135].

$$SED = 0.5 \times (\sigma \cdot \varepsilon) \quad \textit{(Equation 3-7)}$$

These three measures were calculated separately for the cortical and trabecular regions at 10mm incremental slices throughout the proximal 80mm of each bone, shown in Figure 3-4. The overall average of the top 40mm and 80mm of the proximal bones were also calculated for the trabecular and cortical bones, respectively, due to a lack of trabecular bone in the distal 40 mm.

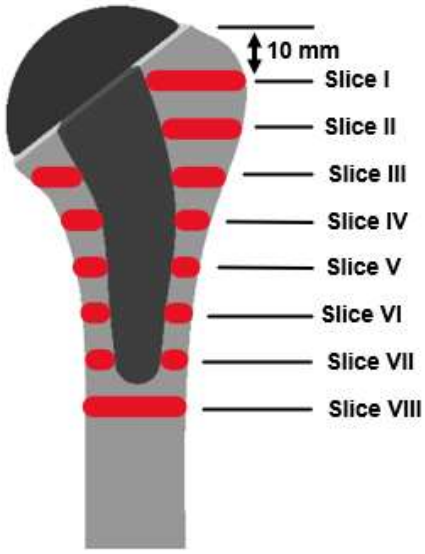

Figure 3-4. Slices taken on the proximal humeri. Cortical bone is found in all 8 slices. Trabecular bone is found in the proximal four slices. Bone mechanobiology measures were calculated and average across all slices as well as across the entire proximal 80mm/40m for the cortical and trabecular regions.

3.2.6 Stem Construction and Placement Sensitivity

The humeral stem was translated 1.5mm (25% of the gyroid unit length) in one direction, before the Boolean operation, to create a second 60% porosity stem (referred from here as G60b) to compare the effect of gyroid location within the stem. The G60b stem was analyzed within the osteopenic bone only. The G60 stem was also manually implanted into the osteopenic bone a second time to compare the effects of the manual placement. The G60b stem and second G60 stem placement were only analyzed under the 90° of flexion loading condition.

3.2.7 Statistical Analysis

The mean values and standard deviations were calculated across the four loading conditions for each of the bone mechanobiology measures. Independent t-tests were performed in Excel to compare the mean values of each stem type in each slice. Significant difference was defined at the 5% level ($p<0.05$).

3.3 Results

3.3.1 Stem Viability

The Von Mise stress distributions across each porous stem for each scenario (three bone densities, four held-arm positions) were analysed. With the exception of a few mesh-dependent singularities, none of the porous stems exceeded the yield strength of Ti6Al4V (880 MPa) in any of the scenarios. To better understand the effects of gyroid porosity and bone density on the

viability of these stems, Figure 3-5 shows the distributions of Von mises stresses in each porous stem for each scenario. As expected, the stresses in the porous stems increased as stem porosity increased (decrease in wall thickness). There was not a clear trend in the stress distributions on the stems across the different bone densities however, the largest stresses were observed in the G80 stem when employed in the healthy bone under the 120° of flexion loading condition. The average Von Mises stress in this localized high stress region was 408.9 MPa.

The predicted fatigue lives for each of the stems in each loading scenario were predicted using a fatigue analysis software (Fe-safe). All the stems were predicted to exceed 10 million cycles (of the full range of their respective loads) without catastrophic failure, as no failure was predicted in the internal struts of the porous stems.

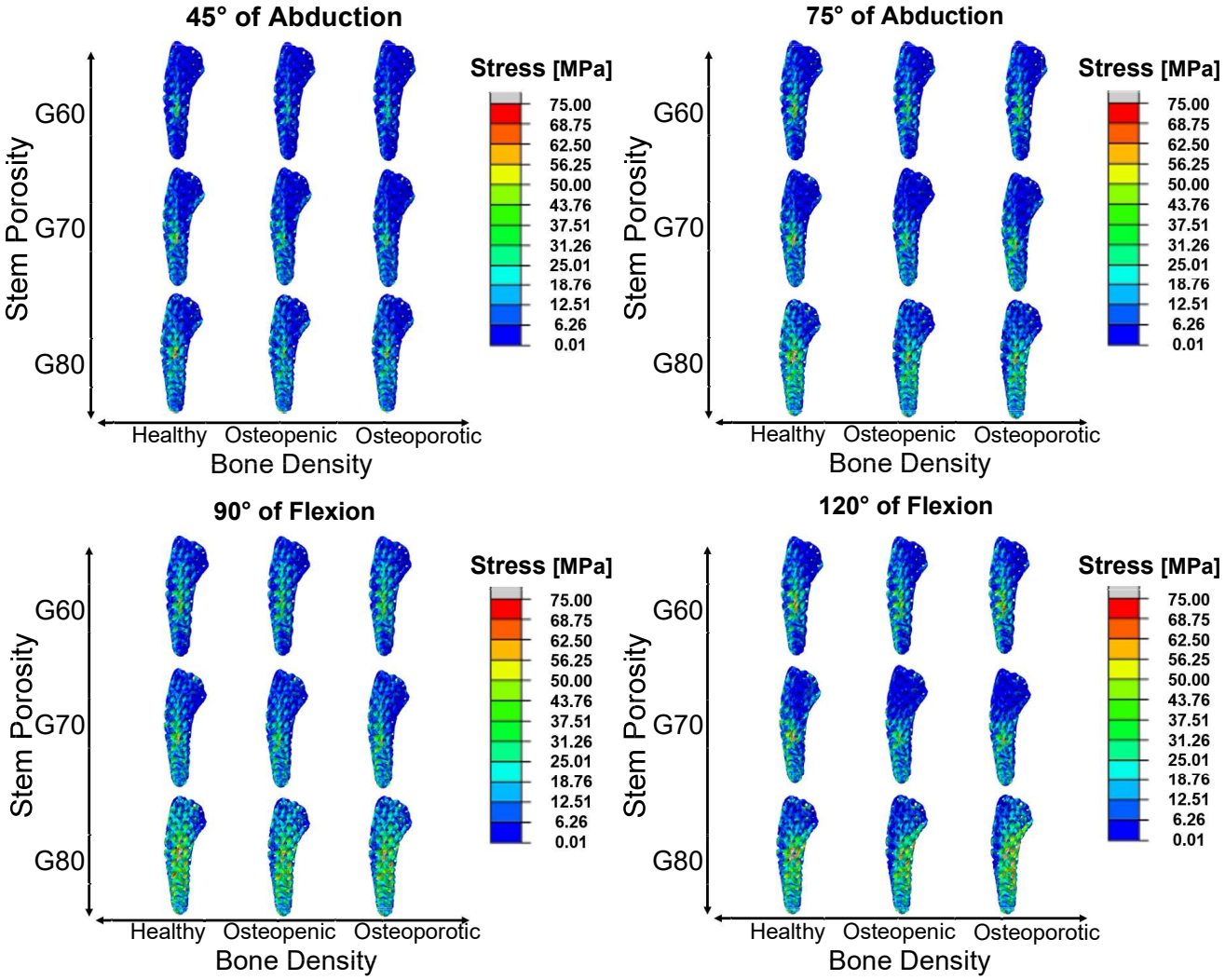

Figure 3-5. Von Mises stress distributions on the porous stems when under each of the loading conditions in each of the bone densities. Stress values are scaled down to better exhibit the stress distributions.

3.3.2 Bone Mechanobiology

The results for all three outcome measures have been averaged across the four loading conditions in order to observe trends in the effects of stem porosity versus a traditional solid stem. The results for each individual loading scenario can be found in Appendix 5.7.

3.3.2.1 Change in Von Mises Stress

The volume-weighted average changes in von Mises stress with respect to the intact bone are shown for each slice and the overall proximal bone in Figure 3-6. There is a trend of a decrease in stresses as you move distally down the humerus for all the stems. The effects of stem porosity are not consistent from slice to slice, however the greatest and most consistent effects are in the osteoporotic bone, where an increase in stem porosity further decreases the Von mise's stresses in the bone compared to the solid stem. The greatest significant difference in all the slices is in the trabecular region of the most proximal slice (Slice I) of the healthy humerus, with a ~43% decrease in stress when the G70 stem is employed versus the solid. For the entire proximal regions analysed, the greatest significant difference in stress was a ~25% decrease in the trabecular region of the osteoporotic bone when the G80 stem was employed versus the solid stem.

To compare the effects of stem design, stem placement, and gyroid to bone interaction, the change in Von Mises stress in the osteopenic bone when the G60 stem, G60b stem, G60 stem in a slightly different location, and the solid stem with a reduced elastic modulus (14.5 GPa) to represent the 60% porous gyroid (refer to Chapter 2) are plotted in Figure 3-7. The largest difference observed between stem scenarios was in the trabecular region of slice IV. The G60 stem caused a ~29% decrease compared to the G60b stem. The greatest difference in the overall cortical region was a ~3% decrease when the G60b stem when employed versus the solid stem with a reduced elastic modulus. The greatest difference in the overall trabecular region was a ~15% decrease when the G60 stem in a new location was employed versus the G60 stem.

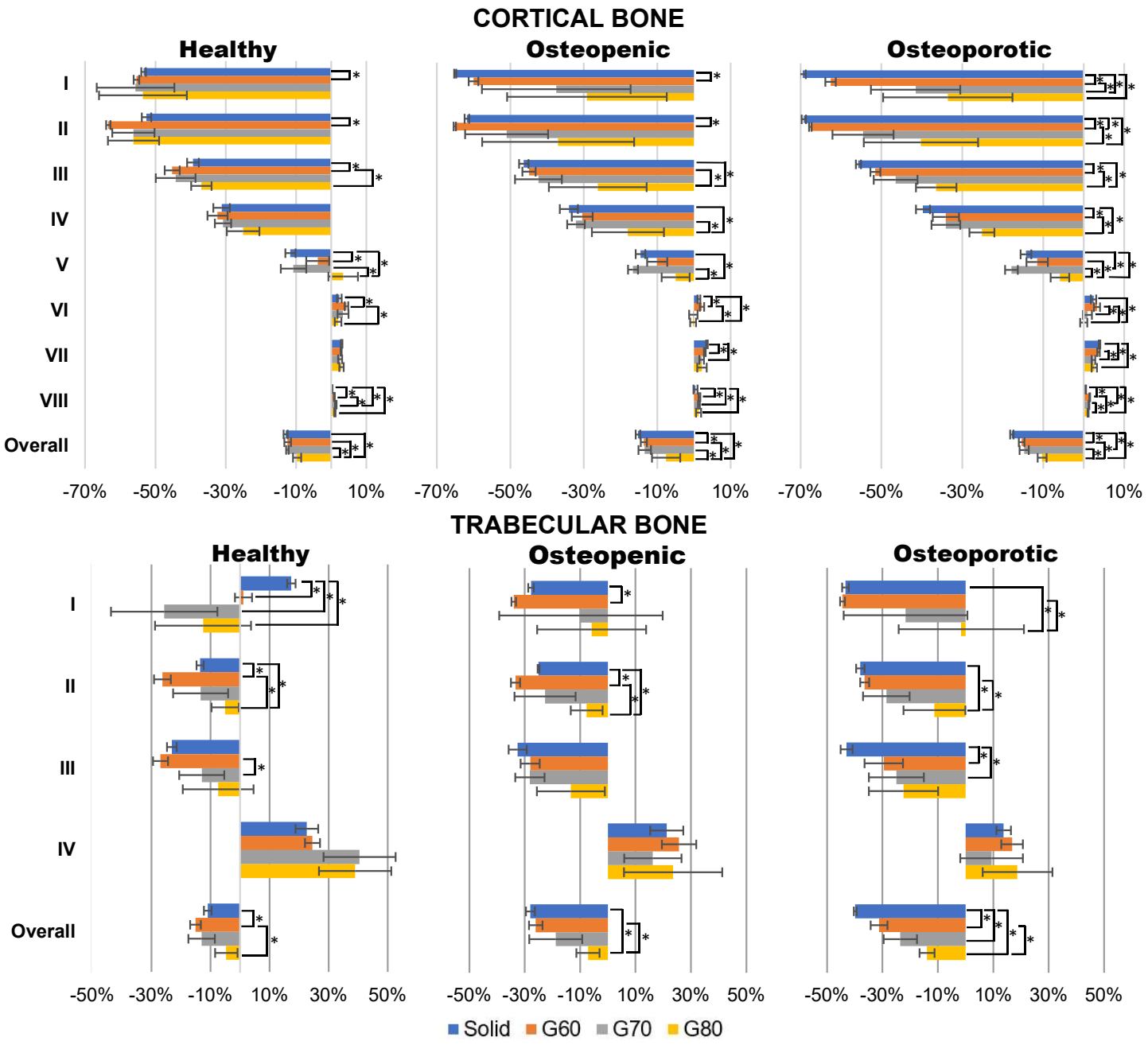

Figure 3-6. Volume-weighted average change in the magnitude of Von Mises stress for the reconstructed bone as a percentage of the intact bone. Reported values are averaged across the four loading conditions to compare the effects of stem porosity in all three bone densities. * indicates a significant difference between the two values.

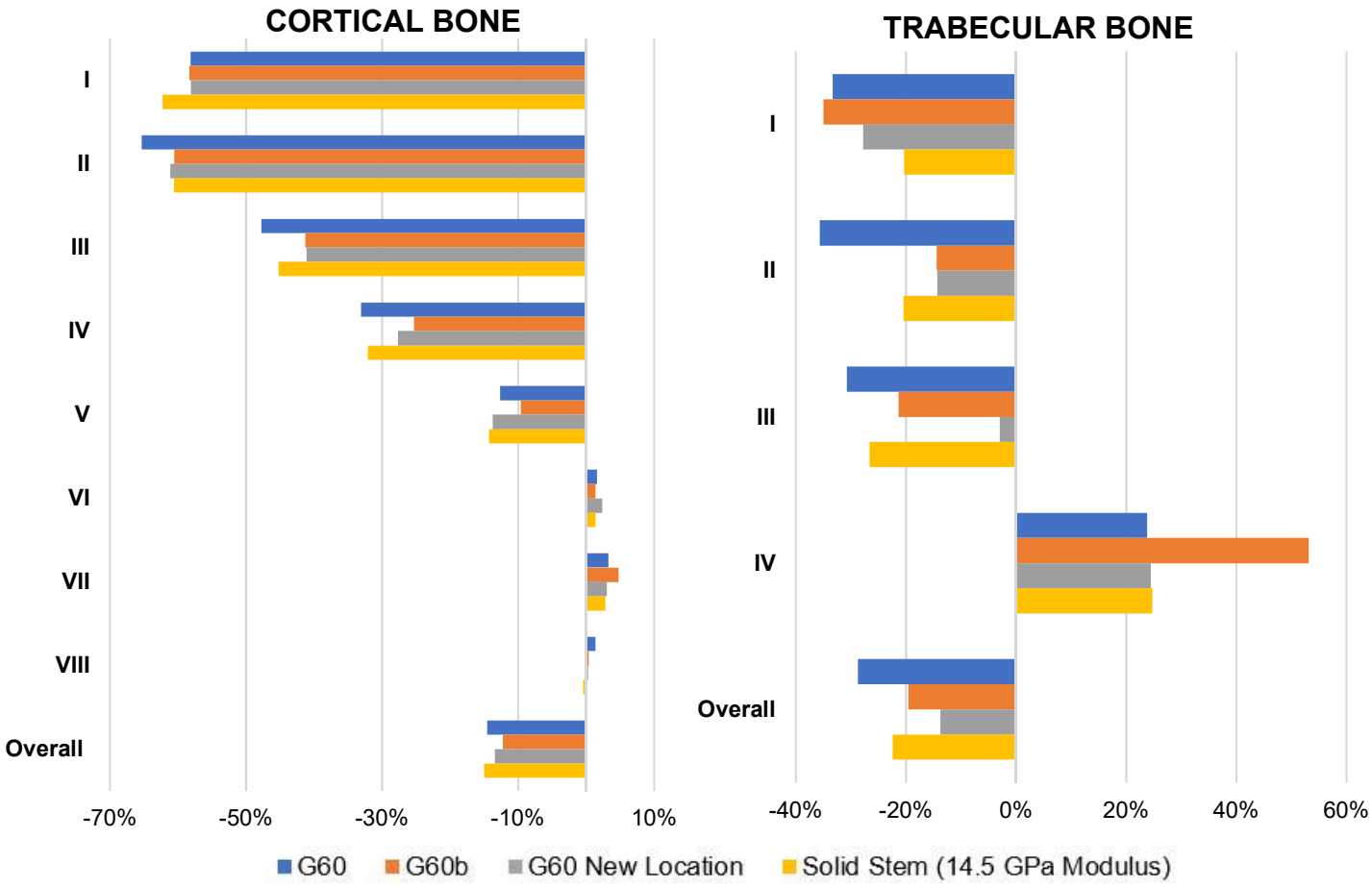

Figure 3-7. Volume-weighted average change in the magnitude of Von Mises stress for the reconstructed bone as a percentage of the intact bone. In this scenario, the osteopenic bone is under the 90° of flexion loading condition. G60 represents the original porous stem. G60b represents the second created stem where the implant stem was shifted 1.5 mm within the gyroid structure before the Boolean operation.

3.3.2.2 Deviatoric Change in Stress

The deviatoric changes in stress tensor with respect to the intact state at each slice, as well as the overall proximal region of the bone, are shown in Figure 3-8. There was not a consistent trend when comparing the stem porosities effects for this outcome measure in any of the bone densities. However, there is a decrease in the deviatoric change in stress as you move distally along the humeri for all the employed stem scenarios.

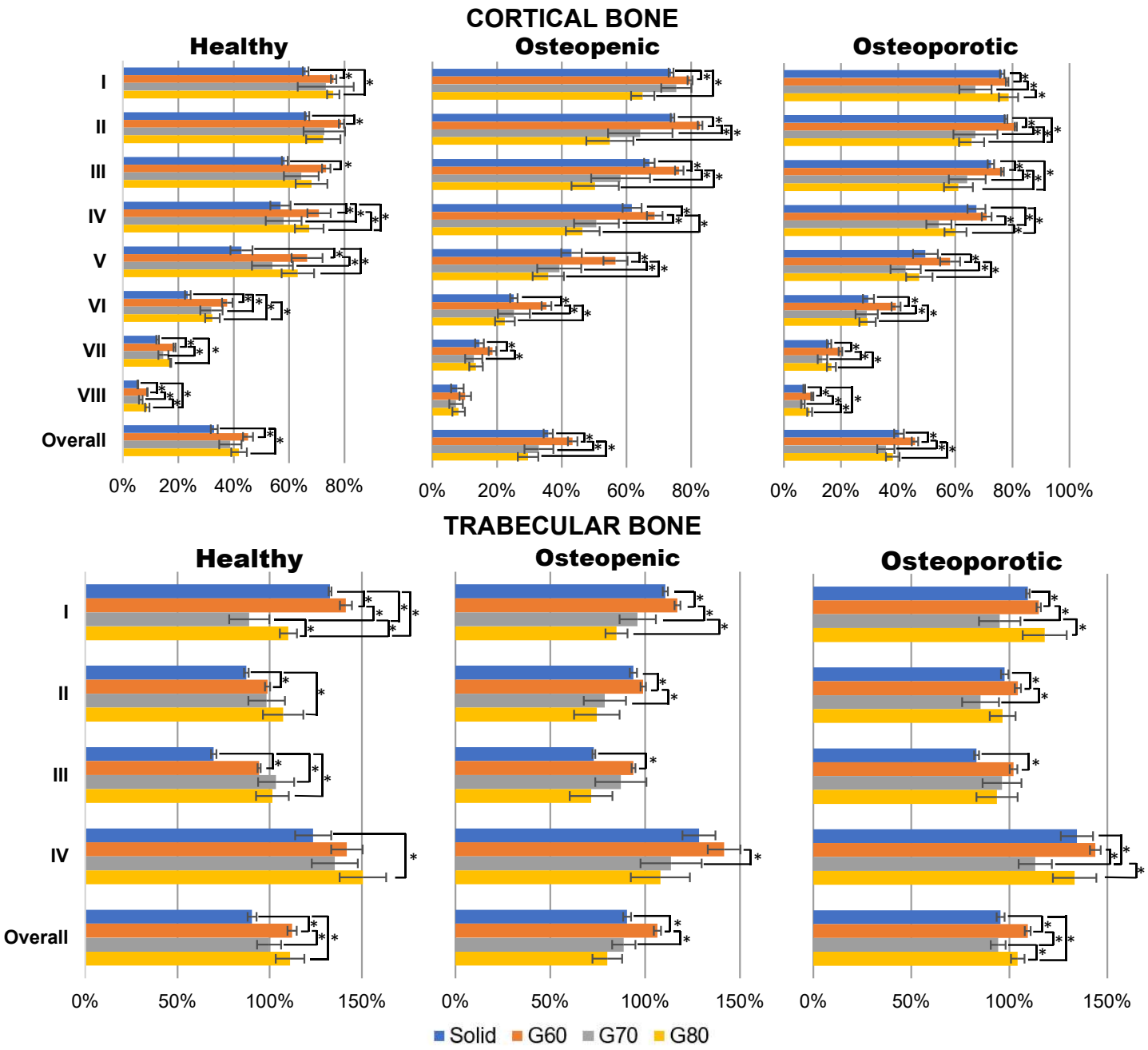

Figure 3-8. Volume-weighted deviatoric change in stress tensor for the reconstructed bone as a percentage of the intact bone. Reported values are averaged across the four loading conditions. Error bars represent the standard deviation. * indicates a significant difference between the two values.

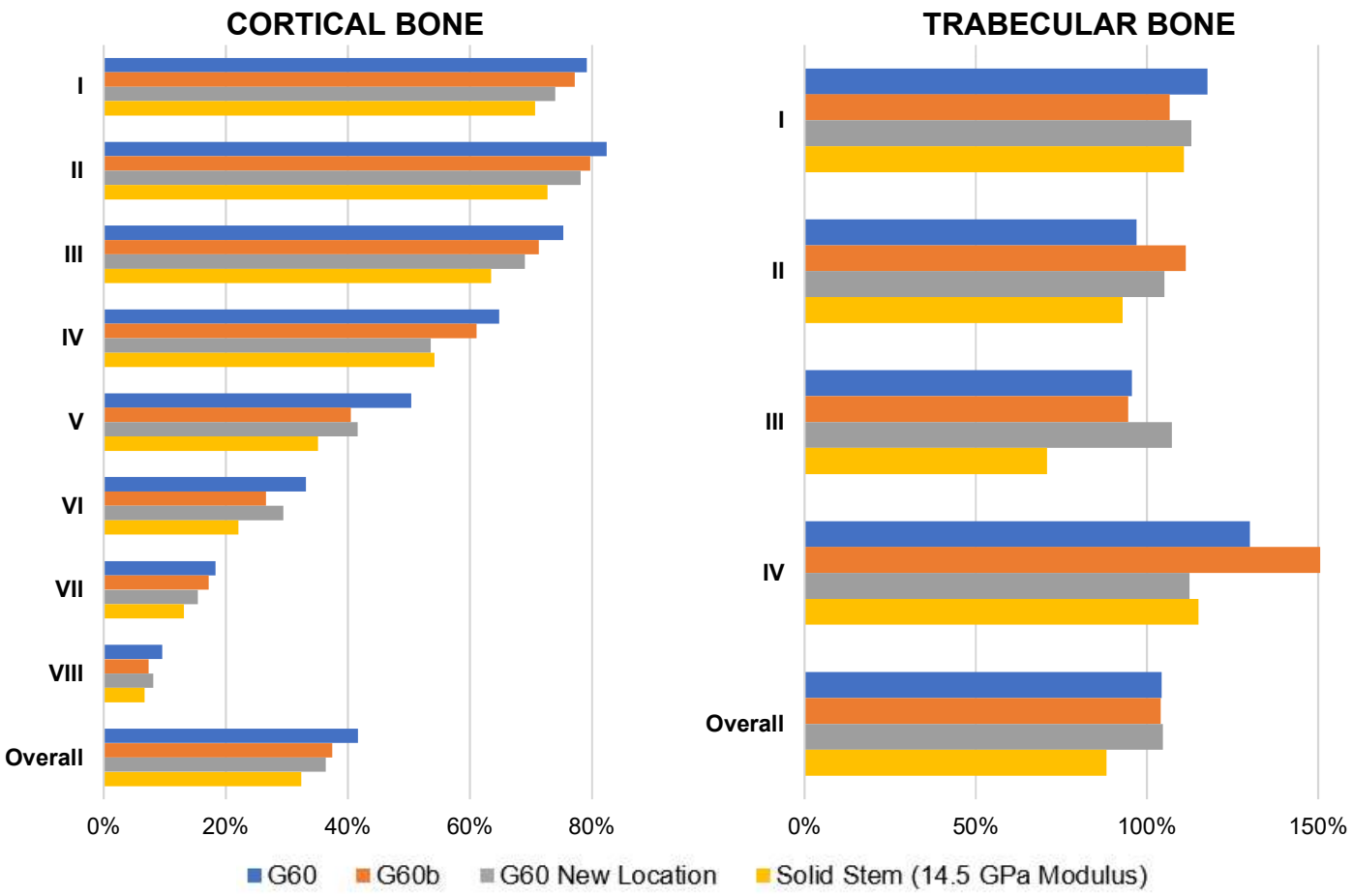

Figure 3-9. Volume-weighted deviatoric change in stress tensor for the reconstructed bone as a percentage of the intact bone. This is when the osteopenic bone is under the 90° of flexion loading condition. G60 represents the original porous stem. G60b represents the second created stem where the implant stem was shifted 1.5 mm within the gyroid structure before the Boolean operation.

The greatest significant difference was observed in the trabecular region of the most proximal slice (slice I) in the healthy bone when the G70 stem caused a ~52% decrease compared to when the G60 stem is employed. The greatest significant difference in the entire analysed proximal region was in the trabecular region of the healthy humerus, where a ~22% decrease was caused by the employment of the solid stem versus the G60 stem.

To compare the effects of stem design, stem placement, and gyroid to bone interaction, the deviatoric change in stress in the osteopenic bone when the G60 stem, G60b stem, G60 stem in a slightly different location, and the solid stem with a reduced elastic modulus (14.5 GPa) to represent the 60% porous gyroid (refer to Chapter 2) are plotted in Figure 3-9. The largest difference between stem scenarios (~38% decrease) occurred in the trabecular region of slice IV, when the G60 stem was employed in a new location versus the G60b stem. The greatest difference in the overall cortical region was a ~9% decrease when the solid stem with a reduced elastic modulus was employed versus the G60 stem. The greatest difference in the overall

trabecular region was a ~16% decrease when the solid stem with a reduced elastic modulus versus the G60 stem in a new location.

3.3.2.3 Percentage of Bone Resorption/Formation

This measure estimates the bone remodelling potential of the bone. There is not a consistent trend across all slices, but there is a trend of a decrease in bone resorption as we increase stem porosity in the overall proximal bone, particularly in the osteopenic and osteoporotic humeri. Across all slices, the greatest decrease in bone resorption (~47% of bone volume) is observed in the cortical region of the most proximal slice (Slice I) of the osteoporotic bone when the G80 stem is employed compared to the solid stem. For the overall proximal regions, the greatest decrease in bone resorption is observed in the cortical region of the osteoporotic bone when the G80 stem is employed compared to the solid stem (~17% of bone volume). The volume percentage of bone resorption/formation is displayed in Figure 3-10 for both the cortical and trabecular bone regions for all bone slices and the overall proximal region of the bone.

To compare the effects of stem design, stem placement, and gyroid to bone interaction, the potential bone resorption/formation in the osteopenic bone when the G60 stem, G60b stem, G60 stem in a slightly different location, and the solid stem with a reduced elastic modulus (14.5 GPa) to represent the 60% porous gyroid (refer to Chapter 2) are plotted in Figure 3-11. The largest difference in bone resorption between stem scenarios was in the cortical region of Slice IV (~21% decrease) when the G60 stem was in a new position versus its original position. The cortical and trabecular regions both had an overall decrease in bone resorption of ~5%. For the cortical bone, this decrease was caused by the employment of the G60b stem versus the G60 stem. For the trabecular bone, this decrease was a result of the G60 stem in a new location versus the G60 stem.

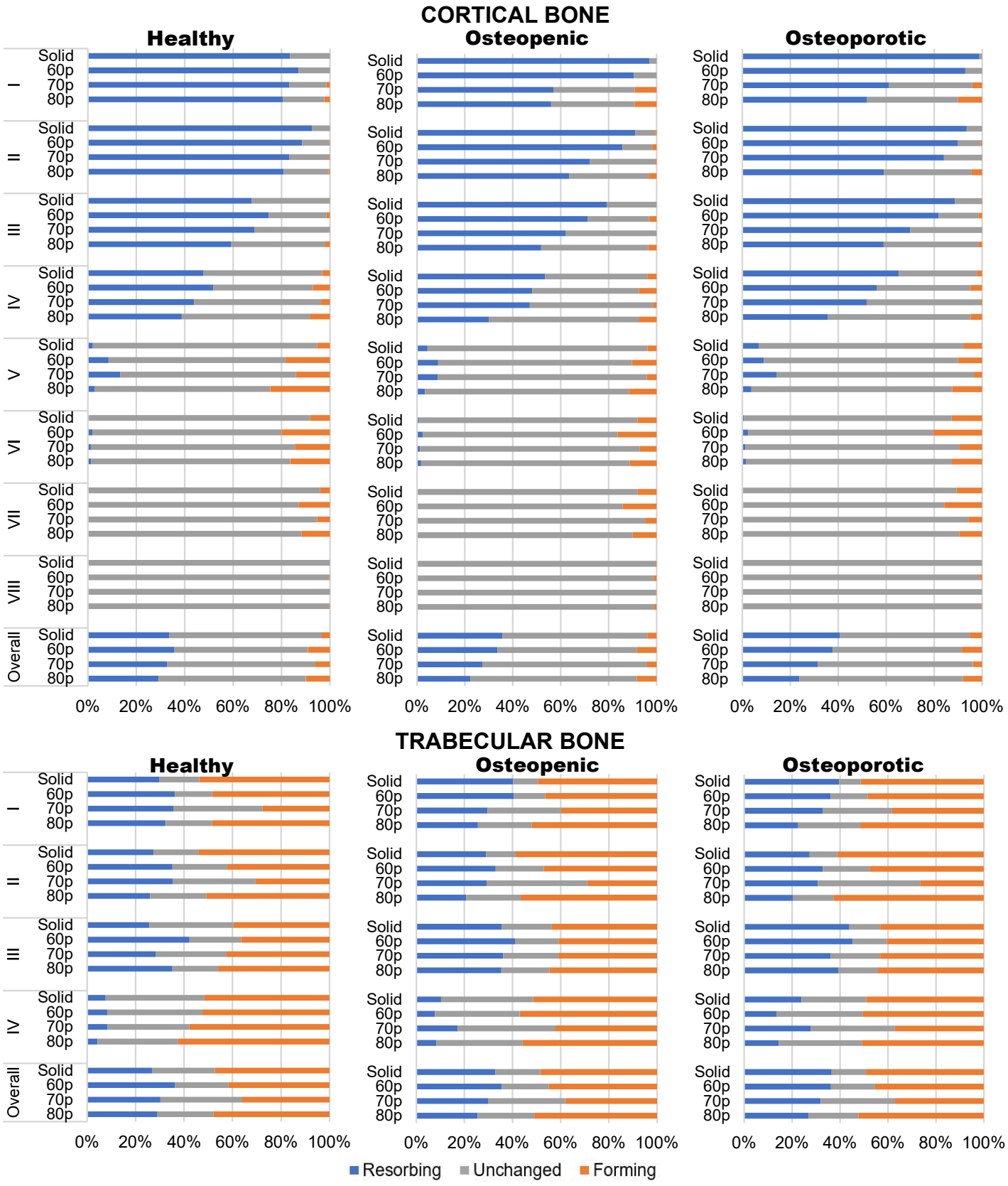

Figure 3-10. Volume percentage of bone resorption/formation in the reconstructed bones.
Reported values are averaged across the four loading conditions.

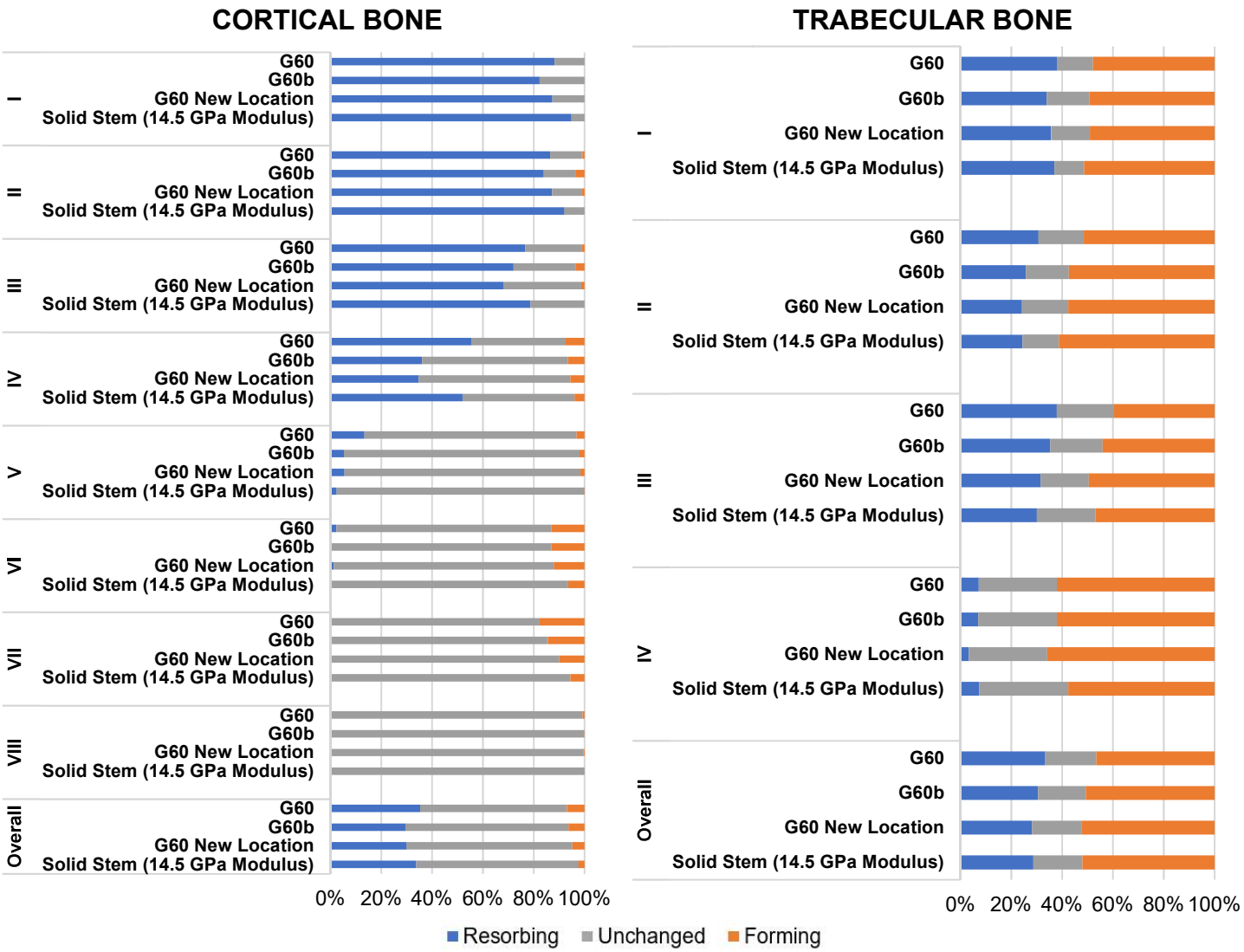

Figure 3-11. Volume percentage of bone resorption/formation in the reconstructed osteopenic bone when under the 90° of flexion loading condition. G60 represents the original porous stem. G60b represents the second created stem where the implant stem was shifted 1.5 mm within the gyroid structure before the Boolean operation.

3.4 Discussion

The main objective of this study was to assess the mechanical capabilities of porous humeral stems constructed from sheet-based gyroids, using finite element modelling. All three stem porosities demonstrated adequate strength for implantation based on four physiologically relevant loads. Not only did none of the stems experience stresses exceeding the yield strength of titanium but they were all predicted to experience more than 10 million life cycles (of each arm position) through a virtual fatigue life analysis (Fe-safe). This is an important finding that indicates these porous stems would be viable for permanent implantation. Good agreement between Fe-safe

fatigue life predictions and experimental fatigue lives have been demonstrated in the literature, assuming no disparities between the virtual models and 3D printed structures. Duan et al. used Fe-safe to predict the fatigue lives of dental implants within a 95% confidence interval of their experimental results [124]. Although there were more discrepancies between the predicted and actual fatigue lives outlined in Chapter 2, these disparities could be attributed to the printing defects.

Although an implant stem would experience more than 10 million loading cycles in its lifetime, there are other factors that will affect the loading on the stems. One major factor is the bony ingrowth that may occur within the pores of the stem. A study by Kelly et al. explored the ability of osseointegration on gyroid structures for implant applications [136]. It can be assumed that bony ingrowth could potentially increase the strength of the stem and extend its fatigue life.

A secondary goal of this study was to observe the mechanobiological impact of these porous stems in comparison with a solid stem of similar length. Although a clear indication of positive effects would have been ideal, there is no evidence of these stems having a further negative impact on the bones than a traditional solid stem. The percentage of change in stress and deviatoric stress tensor did not provide a clear trend regarding the effects of stem porosity on the resultant bone stresses. The percentage of bone resorption/bone formation was a better indication of how stem porosity will affect the bone remodelling process. Although not consistent on a slice-by-slice basis, there was a trend of a decrease in bone resorption as stem porosity increased in the overall proximal humeri. These trends became more prominent as bone density decreased. These results indicate that the use of a porous stem may have some beneficial impacts on bone mechanobiology and these benefits will increase when employed in bones of lesser density.

Another factor that was touched on in this study was the effects of the gyroid stem construction and its placement within the humeri. Some differences were observed, but overall there was no obvious best choice between the three porous stem options. These results do indicate that bone mechanobiology is sensitive to the gyroid design and the gyroid stem placement. This highlights the importance of not only a reduced elastic modulus for implant design, but the implant to bone interaction as well. Due to the gyroid stems macroporosity, a smaller amount of the bone is in contact with the stem (in comparison to the solid stem) therefore altering the load transfer to the bone. An automized method to develop these gyroid stems and place them within the bone models could potentially determine the scenario with an optimized stem to bone contact. An idea

of how the porous stems, without the effect of different bone to stem interactions, could impact the bone mechanobiology is demonstrated in Appendix 5.8, where each scenario was analyzed using the solid stem with reduced moduli to represent the G60 (14.5 GPa), G70 (10.6 GPa), and G80 (7.15 GPa) stems (refer to Chapter 2).

Future work could explore different variations of the porous stem design, such as a porosity gradient. It is clear with all the employed stems, solid and porous, there are greater stress shielding effects observed proximally than distally in the humerus. A porosity gradient, which increases proximally, may exhibit more ideal bone effects. Although the humerus models in this study were averaged from 75 cadaveric humeri, further investigation of these gyroid stems should include the use of various humerus shapes as well.

3.5 Conclusion

This study was a preliminary analysis to see if the use of porous gyroid stems is a feasible option to combat orthopaedic infection. Based on the finite element results, these stems show promise in exhibiting the adequate strength for bone implantation. Although their bone mechanobiological impacts were not clear, some improvements were demonstrated. Further computational work should include the use of different humerus shapes as well as an exploration of different gyroid stem configurations.

Chapter 4

4 Summary and Future Works

This chapter summarizes the objectives of this work, the methods used to explore those objectives and the conclusions that were found. This chapter also outline the strengths and limitations of the studies and the future work that should be conducted to help achieve the research goal.

4.1 Summary

Infection is a serious complication associated with orthopaedic implants. The current gold standard to treat ODRI requires patients to undergo multiple surgeries and uses an ineffective method of drug delivery, leaving the patient at further risk of infection. More ideal drug delivery carriers, such as calcium sulfate, could help decrease the amount of infection that occurs from revision surgeries. Housing this calcium sulfate in a permanent porous implant, as opposed to a temporary spacer like PMMA, will not only improve the antibiotic delivery, therefore reducing the chances of biofilm formation, but will only require a single revision surgery instead of two.

A better understanding of the mechanical capabilities of gyroid-based structures was required in order to determine if they are a potential option for a porous implant. The first objective of this study was to compare the FE models of cylindrical gyroids to experimental static compression and compression-compression fatigue tests. Although there were some discrepancies between the in silico and experimental results, due to manufacturing defects, the FE models were able to provide insight into the trends across different gyroid porosities. There was a similar relationship between the apparent moduli of elasticity and porosity for both computational and experimental models. The agreement between fatigue life predictions and actual fatigue lives improved as stem porosity decreased. This indicates if there were no differences between the nominal and actual porosities, the fatigue life predictions would be far more representative of the actual fatigue behaviours. This is further confirmed by a study outlined in a thesis by William Anderson, who saw good agreement between Fe-safe predictions and experimental results of 3D-printed Ti6Al4V solid specimens [137].

The second objective of this study was to develop a case study of gyroid-based shoulder implants to assess both their mechanical capabilities and effect on bone mechanobiology. The gyroid cylinders exhibited high strengths, surviving loads much greater than the loads typically

experienced in the shoulder. However, the shoulder does not experience purely compression loads and therefore an exploration of physiologically relevant loads, both in magnitude and direction, were important to analyze. Using finite element models, three different gyroid stem porosities (60%, 70%, and 80%) were determined to have adequate strength (static and fatigue) under twelve different loading scenarios (three bone densities, four held-arm positions). Although there were discrepancies exhibited between the FE models and the experimental tests with the gyroid cylinders, the gyroid stem results are under the assumption that there would be no manufacturing defects present in the stems used for implantation. It was also concluded that the use of these porous stems does not have a greater negative impact than solid stems on the bone mechanobiology of proximal humeri and may even offer some benefits to bone remodelling, most prominently in osteoporotic bone.

4.2 Limitations and Strengths

The first objective of this study was limited by the manufacturing of the specimens. As demonstrated by the static compression testing, there was a 1.52 GPa difference in the apparent modulus of elasticity between the 60P specimens. It can be assumed from the difference between nominal and actual porosities, there are variations between the FE models and physical specimens. This difference could be due to internal voids or thinner than intended walls in the physical specimens. Although adjustments were made to match the FE models with the experimental strains, there are some dissimilarities from specimen to specimen, as demonstrated by the static compression results. The high cycle fatigue behaviour was not as affected by the inconsistencies between specimens, as shown by the similar fatigue lives of the 60P specimens at the same loading cycle. Another limitation of this study is that the specimens were only tested in compression. For the application of orthopaedic implants, it is not realistic that the specimens would only experience pure compression. In the future, torsion and bending testing would allow for a better understanding of the mechanical capabilities of these gyroid structures. A strength of this study was the use of five different porosity levels. Although there was some disagreement in the static and fatigue parameters determined between in silico and experimental tests, there was similar trends observed in both methods across the porosities.

The second objective of this study explored the case study of humeral gyroid implant stems. This objective was limited by the use of linear tetrahedral elements as opposed to quadratic elements. As demonstrated in Chapter 2, second-order elements are more indicative of actual behaviours, however they require much greater computing power which was not possible in this study.

Another limitation of this study is the use of one humerus shape. However, the humerus shape was developed to represent 75 humeri [25]. As well, the identical meshes between intact and reconstructed bones allowed for the direct comparison of bone mechanobiology measures between different stem scenarios. A strength of the study was the use of three different bone densities, to observe the effects across different populations. Another limitation of this study was the manual placement of the gyroid stems. Although each gyroid stem type was in the exact same location across bone densities and loading scenarios, there are slight variations in the placement of the three stem porosities. The effects of the stem placement were explored in a case study of the G60 stem. There were some differences observed between the two placements of the G60 stem, however there was no definitive better placement. The study was also limited by the development of the gyroid stems. Although three different porosities were explored, the porosity was only altered by the thickness of the walls. Future work should explore the effect of altering pore size as a method of varying porosity. The gyroid stems were constructed through a Boolean operation between a cuboid structure and a solid humeral stem. Depending on the placement of the solid stem within the gyroid structure, it alters the outer surface of the gyroid stem. The effects of this Boolean operation were explored in the comparison of the G60 and G60b stems. Again, there were some differences observed between the G60 and G60b stems, but there was not clear better choice. Along with different stem porosities and bone densities, four abduction/flexion motions were analyzed based on an in vivo study by Bergmann et al [134]. The simulations of these motions explored the more physiologically-relevant loads experienced in the shoulder, as opposed to the pure-compression models in Chapter 2.

4.3 Future Directions

This study demonstrated that the FE models can allow us to predict the relationships between gyroid porosities. In order to see better agreement between the monotonic and fatigue behaviours of the in silico and experimental results, an in-depth study of the 3D-printing of these thin-walled structures should be assessed. It is anticipated that solving the inconsistencies within the printed specimens will solve the discrepancies between in silico and experimental results. After better agreement is shown between testing methods, the torsion and bending behaviours of these models should be explored.

An interesting future study, regarding the gyroid shoulder implant stems, would be to explore the construction of the gyroid stems to optimize strength and reduce stress shielding. This optimization could include altering the pore size or incorporating a porosity gradient. Although,

these two factors are important to explore, there may be a trade-off between the strength of the gyroid stems and their drug elution kinetics. Farther in the future, the next step would be to conduct in vitro testing of these gyroid stems using cadaveric humeri. The in vitro stresses and strains could be measured and directly compared to the in silico models.

4.4 Significance

Orthopaedic implant infection is a detrimental complication of joint arthroplasties. The results shown in this thesis are preliminary steps in developing an implant stem that could prevent the need of two-staged revision surgeries to treat ODRI. A single revision surgery would have a major benefit to patients, doctors, caretakers, and our medical system. Although further work is still required, this research shows that these gyroid implant stems are a promising solution to this extremely important healthcare problem.

References

[1] C. I. f. H. Information, "Canadian Joint Replacement Registry: 2019-2020 Full Annual Report.," Ottawa, 2021.

[2] R. S. Charette and C. M. Melnic, "Two-Stage Revision Arthoplasty for the Treatment of Prosthetic Joint Infection," *Current Reviews in Musculoskeletal Medicine,* vol. 11, pp. 332-340, 2018.

[3] B. A. Marson, S. T. Walters, B. V. Bloch and K. Sehat, "Two-stage revision surgery for infected total knee replacements: resonable function and high sucess rate with the use of primary knee replacement implants as temporary spacers," *European Journal of Orthopaedic Surgery & Traumatology,* vol. 28, pp. 109-115, 2018.

[4] H. A. Leonard, A. D. Liddle, O. Burke, D. W. Murray and H. Pandit, "Single- or Two-stage Revision for Infected Total Hip Arthroplasty? A Systematic Review of the Literature," *Clinical Orthopaedics and Related Research,* vol. 472, pp. 1036-1042, 2014.

[5] R. Pivec, Q. Naziri, K. Issa, S. Banjeree and M. A. Mont, "Systematic Review Comparing Static and Articulating Spacers Used for Revision of Infected Total Knee Arthroplasty," *The Journal of Arthroplasty,* vol. 29, pp. 553-557, 2014.

[6] A. Pellegrini, C. Legnani, V. Macchi and E. Meani, "Two-stage revision shoulder prosthesis vs. permanent articulating antiobiotic spacer in the treatment of perprosthetic shoulder infections," *Orthopaedics & Traumatology: Surgery & Research,* no. 105, pp. 237-240, 2019.

[7] H. van de Belt, D. Neut, W. Schenk, J. R. van Horn, H. C. van der Mei and H. J. Busscher, "Infection of orthopaedic implants and the use of antibiotic-loaded bone cements: A review," *Acta Orthopaedica Scandinavica,* vol. 72, no. 6, pp. 557-571, 2001.

[8] K. Urabe, K. Naruse, H. Hattori, M. Hirano, K. Uchida, K. Onuma, H. J. Park and M. Itoman, "In vitro comparison of elution characterisitcs of vancomycin from calcium phosphate cement and polymethylmethacrylate," *Journal of Orthopaedic Science,* vol. 14, pp. 784-793, 2009.

[9] S. Samuel, B. S. Mathew, B. Veeraraghavan, D. H. Fleming, S. B. Chittaranjan and J. A. J. Prakash, "In vitro study of elution kinetics and bio-activity of meropenem-loaded acrylic bone cement," *Journal of Orthopaedics and Traumatology,* vol. 13, pp. 131-136, 2012.

[10] S. Gitelis and G. T. Brebach, "The treatment of chronic osteomyelitis with a biodegradable antibiotic0impregnated implant," *Journal of Orthopaedic Surgery,* vol. 10, no. 1, pp. 53-60, 2002.

[11] OpenStax College, Anatomy and Physiology, Houston, Texas: OpenStax College, 2013.

[12] E. F. Morgan, G. U. Unnikrisnan and A. I. Hussein, "Bone Mechanical Propeties in Healthy and Diseased States," *Annual Review of Biomedical Engineering,* pp. 119-143, 2019.

[13] J. Y. Rho, R. B. Ashman and C. H. Turner, "Young's modulus of trabecular and cortical bone material: ultrasonic and microtensile measurements," *Journal of Biomechanics,* vol. 26, no. 2, pp. 111-119, 1993.

[14] Q.-H. Qin, Mechanics of Cellular Bone Remodeling: Coupled Thermal, Electrical, and Mechanical Field Effects, Boca Ranton: Taylor & Francis Group, LLC, 2013.

[15] J. Wolff, "Ueber die innere Architectur der Knochen und ihre Bedeutung fUr die Frage vom Knochenwachsthum," *Virchows Archiv: an international journal of pathology,* vol. 50, no. 3, pp. 389-450, 1870.

[16] H. Zippel, "Julius Wolff and the Law of Bone Remodelling," in *Wolff's Law and Connective Tissue Regulation*, Berlin, Walter de Gruyter & Co., 1993, pp. 1-12.

[17] P. Maquet, "Wolff's Law," in *Wolff's Law and Connective Tissue Regulation*, Berlin, Walter de Gruyter, 1992, pp. 31-33.

[18] S. C. Cowin and D. H. Hegedus, "Bone remodeling I: theory of adaptive elasticity," *Journal of Elasticity,* vol. 6, no. 3, pp. 313-326, 1976.

[19] D. P. Fyhrie and D. R. Carter, "A Unifying Principle Relating Stress to Trabecular Bone Morphology," *Journal of Orthopaedic Research,* vol. 4, no. 3, pp. 304-317, 1986.

[20] R. Huiskes, H. Weinans, H. J. Grootenboer, M. Dalstra, B. Fudala and T. J. Sloof, "Adaptive Bone-Remodeling Theory Applied to Prosthetic-Design Analysis," *Journal of Biomechanics,* vol. 20, no. 11, pp. 1135-1150, 1987.

[21] M. Zhang, T. Gregory, U. Hansen and C.-K. Cheng, "Effect of stress-shielding-induced bone resorption on gelnoid loosening in reverse total shoulder arthroplasty," *Journal of Orthopaedic Research,* vol. 38, pp. 1566-1574, 2020.

[22] S. Klingebiel, K. N. Schneider, G. Gosheger, T. Ackmann, M. Timme, C. Rickert, N. Deventer and T. Christoph, "Periprosthetic Stress Shielding of the Humerus after Reconstruction with Modular Shouldeer Megaprostheses in Patients with Sarcoma," *Journal of Clinical Medicine,* vol. 10, pp. 1-10, 2021.

[23] C. Quentel, J. Golgado, P. R. Fernandes and J. Monteiro, "Bone remodelling analysis of the humerus after a shoulder arthroplasty," *Medical Engineering & Physics,* vol. 34, pp. 1132-1138, 2012.

[24] N. Razfar, J. M. Reeves, D. G. Langohr, R. Willing, G. S. Athwal and J. A. Johnson, "Comparison of proximal humeral bone stresses between stemless, short stem, and standard stem length: a finite element analysis," *Journal of Shoulder and Elbow Surgery,* vol. 25, pp. 1076-1083, 2016.

[25] P. Soltanmohammadi, A. Tavakoli, G. D. G. Langhor, G. S. Athwal and R. Willing, "Structural analysis of hollow versus solid-stemmed shoulder implants of proximal humeri with different bone qualities," *Journal of Orthopaedic Research,* vol. 40, pp. 674-684, 2020.

[26] P. J. Denard, G. Haidamous, R. Gobezie, A. A. Romeo and E. Lederman, "Short-term evaluation of humeral stress shielding following reverse shoulder arthroplasty using press-fit fixation compared with cemented fixation," *Journal of Shoulder and Elbow Surgery,* vol. 29, pp. 906-912, 2020.

[27] S. C. Kim, J. H. Park, H. Bukhary and J. C. Yoo, "Humeral stem with low filling ratio reduces stress shielding in primary reverse shoulder arthroplasty," *International Orthopaedics,* vol. 46, pp. 1341-1349, 2022.

[28] W. R. Aibinder, F. Uddin, R. T. Bicknell, R. Krupp, M. Scheibel and G. S. Athwal, "Stress shielding following stemless anatomic total shoulder arthroplasty," *Shoulder & Elbow,* Vols. 1-7, no. 0, p. 0, 2021.

[29] F. Schmidutz, Y. Agarwal, P. E. MUller, B. Gueorguiev, R. G. Richards and C. M. Sprecher, "Stress-shielding induced bone remodeling in cementless shoulder resurfacing arthroplasty: a finite element analysis and in vivo results," *Journal of Biomechanics,* vol. 47, pp. 3509-3516, 2014.

[30] P. J. Denard, M. P. Noyes, J. B. Walker, Y. Shishani, R. Gobezie, A. A. Romeo and E. Lederman, "Proximal stress shielding is decreased with a short stem compared with a traditional-length stem in total shoulder arthroplasty," *Journal of Shoulder and Elbow Surgery,* vol. 27, pp. 53-58, 2018.

[31] M. Schnetzke, S. Coda, G. Walch and M. Loew, "Clinical and radiographical results of a cementless short stem shoulder prosthesis at minimum follow-up of two years," *International Orthopaedics,* vol. 39, pp. 1351-1357, 2015.

[32] G. Cortis, I. Mileti, F. Nalli, E. Palermo and L. Cortese, "Additive manufacturing structural rediseign of hip prostheses for stress-shielding reduction and improved functionality and safety," *Mechanics of Materials,* vol. 165, p. 104173, 2022.

[33] S. Gross and E. W. Abel, "A finite element analysis of hollow stemmed hip prostheses as a means of reducing stress shielding of the femur," *Journal of Biomechanics,* vol. 34, pp. 995-1003, 2001.

[34] C. Piao, D. Wu, M. Luo and H. Ma, "Stress shielding effects of two prosthetic groups after total hip joint simulation replacement," *Journal of Orthopaedic Surgery and Research,* vol. 9, no. 1, p. 71, 2014.

[35] S. Arabnjad, B. Johnston, M. Tanzer and D. Pasini, "Fully Porous 3D Printed Titanium Femoral Stem to Reduce Stress-Shielding Following Total Hip Arthoplasty," *Journal of Orthopaedic Research,* pp. 1774-1783, 2017.

[36] R. Bieger, A. Ignatius, H. Reichel and L. DUrselen, "Biomechanics of a Short Stem: In Vitro Primary Stability and Stress Shielding of a Conservative Cementless Hip Stem," *Journal of Orthopaedic Research,* pp. 1180-1186, 2013.

[37] A. Completo, P. Talaia, F. Fonseca and J. A. SimOes, "Relationship of design features of stemmed tibial knee prosthesis with stress shielding and end-of-stem pain," *Materials and Design,* vol. 30, pp. 1391-1397, 2009.

[38] L. de Ruiter, K. Rankin, M. Browne, A. Briscoe, D. Janssen and N. Verdonschot, "Decreased stress shielding with a PEEK femoral total knee prosthesis measured in validated computational models," *Journal of Biomechanics,* vol. 118, p. 110270, 2021.

[39] T. A. Correa, B. Pal, R. J. van Arkel, F. Vanacore and A. A. Amis, "Reduced tibial strain-shielding with extraosseous total knee arthoplasty revision system," *Medical Engineering and Physics,* vol. 62, pp. 22-28, 2018.

[40] A. Completo, F. Fonseca and J. A. SimOes, "Strain shielding in proximal tibia of stemmed knee prosthesis: Experimental study," *Journal of Biomechanics,* vol. 41, pp. 560-566, 2008.

[41] Canadian Institute for Health Information, "Implantable Medical Devices in Canada Insights Into High-Volume Procedures and Associated Costs," Canadian Institute for Health Information, Ottawa, 2020.

[42] V. T. Deore, E. Griffiths and P. Monga, "Shoulder arthroplasty - Past, present and future," *Journal of Arthroscopy and Joint Surgery,* vol. 5, pp. 3-8, 2018.

[43] T. Gluck, "Report on the Positive Results Obtained by the Modern Surgical Experiment Regarding the Suture and Replacement of Defects of Superior Tissue, as well as the Utilization of Re-adsorbable and Living Tamponade in Surgery," *Clinical Orthopaedics and Related Research,* vol. 469, pp. 1528-1535, 2011.

[44] A. S. Ranawat and C. S. Ranawat, "The Knee Joint," in *The history of total knee arthroplasty*, Paris, Springer, 2012, pp. 699-707.

[45] S. R. Knight, R. Aujla and S. P. Biswas, "Total Hip Arthroplasty - over 100 years of operative history," *Orthopaedic Reviews,* vol. 3, no. 16, pp. 72-74, 2011.

[46] I. D. Learmonth, C. Young and C. Rorabeck, "The operation of the century: total hip replacement," *The Lancet,* vol. 370, pp. 1508-1519, 2007.

[47] W. J. Willems, "Histroy of shoulder arthroplasty," *Journal of Arthroscopy and Joint Surgery,* vol. 8, pp. 2-6, 2020.

[48] S. Zilber, "Shoulder Arthroplasty: Historical Considerations," *The Open Orthopaedics Journal,* vol. 11, pp. 1100-1107, 2017.

[49] F. Kruger, "A vitallium replica arthroplasty on the shoulder: a case report of asceptic necrosis of the proximal end of the humerus," *Surgery,* vol. 30, no. 6, pp. 1005-1011, 1951.

[50] C. S. Neer, "ARTICULAR REPLACEMENT FOR THE HUMERAL HEAD," *The Journal of Bone and Joint Surgery,* vol. 11, pp. 215-228, 1955.

[51] T. L. Uhl and N. Myers, "Total Shoulder Arthoplasty," in *Orthopaedic Physical Therapy Secrets: Third Edition*, Elsevier, 2017, pp. 346-352.

[52] L. C. Jones, L. T. Topoleski and A. K. Tsao, "Biomaterials in orthopaedic implants," in *Mechanical Testing of Orthopaedic Implants*, Cambridge, UK, Woodhead Publishing, 2017, pp. 17-32.

[53] T. F. Moriarty, L. G. Harris, R. A. Mooney, J. C. Wenke, M. Riool, S. A. J. Zaat, A. Moter, T. P. Schaer, N. Khanna, R. Kuehl, V. Alt, A. Montali, J. Liu, S. Zeiter, H. J. Busscher, D. W. Grainger and R. G. Richards, "Recommendations for Design and Conduct of Preclinical in Vivo Studies of Orthopedic Device-Related Infection," *Journal of Orthopaedic Research,* pp. 271-287, 2019.

[54] P. Izakovicova, O. Borens and A. Trampuz, "Periprosthetic joint infection: current concepts and outlook," *EFORT Open Reviews,* vol. 4, pp. 482-494, 2019.

[55] A. L. Zhang, B. T. Feeley, B. S. Schwartz, T. T. Chung and C. B. Ma, "Management of deep postoperative shoulder infections: is there a role for open biopsy during staged treatment?," *Journal of Shoulder and Elbow Surgery,* vol. 24, pp. 15-20, 2015.

[56] W. Zimmerli, "Clinical presentation and treatment of orthopaedic implant-associated infection," *Journal of Internal Medicine,* vol. 276, pp. 111-119, 2014.

[57] V. Franceschini and C. Chillemi, "Periprosthetic Shoulder Infection," *The Open Orthopaedics Journal,* vol. 7, pp. 243-249, 2013.

[58] P. Weber, S. Utzschneider, P. Sadoghi, H.-J. Andress, V. Jansson and P. E. MUller, "Management of the infected shoulder prosthesis: a retrospective analysis and review of the literature," *International Orthopaedics,* vol. 35, pp. 365-373, 2011.

[59] J. S. Coste, S. Reig, C. Trojani, M. Berg, G. Walch and P. Boileau, "The management of infection in arthroplasty of the shoulder," *The Journal of Bone & Joint Surgery,* Vols. 86-B, no. 1, pp. 65-69, 2004.

[60] J. Jung, N. V. Schmid, J. Kelm, E. Schmitt and K. Anagnostakos, "Complications after spacer implantation in the treatment of hip joint infections," *International Journal of Medical Sciences,* pp. 265-273, 2009.

[61] A. Lilikakis and M. P. F. Sutcliffe, "The effect of vancomycin addition to the compression strength of antibiotic-loaded bone cements," *International Orthopaedics,* vol. 33, pp. 815-819, 2009.

[62] A. R. Bishop, S. Kim, M. W. Squire, W. E. Rose and H.-L. Ploeg, "Journal of the Mechanical Behaviour of Biomedical Materials," *Vancomycin elution, activity and impact on mechanical properties when added to orthopaedic bone cement,* vol. 87, pp. 80-86, 2018.

[63] I. R. Proubasta, J. P. Itarte, C. G. Lamas and I. U. Escribá, "Permanent Articulated Antibiotic-Impregnated Cement Spacer in Septic Shoulder Arthroplasty: A Case Report," *J Orthop Trauma,* vol. 19, no. 9, pp. 666-668, 2005.

[64] K. Anagnostakos, P. Hitzler, D. Pape, D. Kohn and J. Kelm, "Persistance of bacterial growth on antibiotic-loaded beads: Is it actually a problem?," *Acta Orthopaedica,* vol. 79, pp. 302-307, 2008.

[65] S. S. Aiken, J. J. Cooper, H. Florance, M. T. Robinson and S. Michell, "Local Release of Antibiotics for Surgical Site Infection Management Using High-Purity Calcium Sulfate: An In Vitro Study," *Surgical Infections,* vol. 16, no. 1, pp. 54-61, 2015.

[66] S. J. McConoughey, R. P. Howlin, J. Wiseman, P. Stoodley and J. H. Calhoun, "Comparing PMMA and calcium sulfate as carriers for the local delivery of antibiotics to infected surgical sites," *2015,* vol. 103B, no. 4, pp. 870-877, Journal of Biomedical Materials Research Part B.

[67] J. G. Penn-Barwell, C. K. Murray and J. C. Wenke, "Local Antibiotic Delivery by a Bioabsorbable Gel Is Superior to PMMA Bead Depot in Redicing Infection in an Open Fracture Model," *Journal of Orthopaedic Trauma,* vol. 28, pp. 370-375, 2014.

[68] S. Simha, E. J. Shields and J. M. Wiater, "Periprosthetic Infections of the Shoulder," *The Journal of Bone and Joint Surgery,* vol. 6, no. 9, pp. 1-8, 2018.

[69] A. Manohar, K. Cheung, C. L. Wu and T. S. Stierer, "Burden Incurred by Patients and Their Caregivers After Outpatient Surgery: A Prospective Observational Study," *Clinical Orthopaedics and Related Research,* vol. 472, pp. 1416-1426, 2014.

[70] P. R. Welsh, R. M. Pilliar and I. McNab, "Surgical Implants: The Role of Surface Porosity in Fixation to Bone and Acrylic," *The Journal of Bone & Koint Surgery,* vol. 53, pp. 963-977, 1971.

[71] J. D. Bobyn, R. M. Pilliar, H. U. Cameron and G. C. Weatherly, "The Optimum Pore Size for the Fixation of Porous-Surfaced Metal Implants by the Ingrowth of Bone," *Clinical Orthopaedics and Related Research,* vol. 150, pp. 263-270, 1980.

[72] A. Ketabchi, K. Komm, M. Miles-Rossouw, D. A. D. Cassani and F. Variola, "Nanoporous Titanium Surfaces for Sustained Elution of Proteins and Antibiotics," *PLOS ONE,* vol. 9, no. 3, p. e92080, 2014.

[73] E. Liverani, G. Rogati, S. Pagani, S. Brogini, A. Fortunato and P. Caravaggi, "Mechanical interaction between additive-manufactured metal lattice structures and bone in compression: implications for stress shielding of orthopaedic implants," *Journal of the Mechanical Behaviour of Biomedical Materials,* vol. 121, p. 104608, 2021.

[74] S. Wang, X. Zhou, L. Liu, Z. Shi and Y. Hao, "On the deisgn and properties of porous femoral stems with adjustable stiffness gradient," *Medical Engineering and Physics,* vol. 81, pp. 30-38, 2020.

[75] H. A. Schawrz, "Gesammelte Mathematische Abhandlungen," Julius Springer, Berlin, 1890.

[76] E. R. Neovius, "Bestimmung Zweier Spezieller Periodischer MinimalflAchen," Akademische Abhandlung, Helsinki, 1883.

[77] A. H. Schoen, "Infinite Periodic Minimal Surfaces Without Self-Intersections," National Aeronautics and Space Adminstration, Washington, D.C., 1970.

[78] U. Dierekes, S. Hildebrandt and F. Sauvigny, Minimal Surfaces, Berlin: Springer Berlin Heidelberg, 2010, pp. 3-51.

[79] L. Han and S. Che, "An Overview of Materials with Triply Periodic Minimal Surfaces and Related Geometry: From Biological Structures to Self-Assembled Systems," *Advanced Materials,* vol. 30, pp. 1-22, 2018.

[80] O. Al-Ketan, R. Rowshan and R. K. Abu Al-Rub, "Topology-mechanical property relationship pf 3D printed strut, skeletal, and sheet based periodic metallic cellular materials," *Additive Manufacturing,* vol. 19, pp. 167-183, 2018.

[81] P. Kocovic, "History of Additive Manufacturing," in *3D Printing and Its Impact on the Production of Fully Functional Components: Emerging Research and Opportunities*, Hershey, Philidelphia, IGI Global, 2017, pp. 1-24.

[82] P. Kocovic, "3D Printing Technologies," in *3D Printing and Its Impact on the Production of Fully Functional Components: Emerging Research and Opportunities*, Hershey, Pennsylvania, IGI Global, 2017, pp. 38-49.

[83] B. Liu, Y. Wang, Z. Lin and T. Zhang, "Creating metal parts by Fused Deposition Modeling and Sintering," *Materials Letters,* vol. 263, p. 127252, 2020.

[84] E. L. Papzoglou, N. E. Karkalos, P. Karmiris-ObrantaNski and A. P. Markopoulos, "On the Modeling and Simulation of SLM and SLS for Metal and Polymer Powders: A Review," *Archives of Computational Methoads in Engineering,* vol. 29, pp. 941-973, 2022.

[85] S. C. Kapfer, S. T. Hyde, K. Mecke, C. H. Arns and G. E. SchrOder-Turk, "Minimal surface scaffold designs for tissue engineering," *Biomaterials,* vol. 32, pp. 6975-6882, 2011.

[86] C. Silva, A. I. Pais, G. Caldas, B. P. P. A. Gouveia, J. L. Alves and J. Belinha, "Study on 3D printing of gyroid-based structures for superior structural behaviour," *Progress in Additive Manufacturing,* vol. 6, pp. 689-703, 2021.

[87] D. Mahmoud, K. S. Al-Rubaie and M. A. Elbestawi, "The influence of selective laser melting defects on the fatigue properties of Ti6Al4V porosity graded gyroids for bone implants," *International Journal of Mechanical Sciences,* vol. 193, p. 106180, 2021.

[88] D. Mahmoud, M. A. Elbestawi and B. Yu, "Process-Strcture-Property Relationships in Selective Laser Melting of Porosity Graded Gyroids," *Journal of Medical Devices,* vol. 13, pp. 1-11, 2019.

[89] A. du Plessis, S. M. Razavi and F. Berto, "The effects of microporosity in struts of gyroid lattice structures produced by laser powder bed fusion," *Materials and Design,* vol. 194, p. 108899, 2020.

[90] D. Mahmoud and M. A. Elbestawi, "Selective laser melting of porosity graded lattice structures for bone implants," *The international Journal of Advanced Manufacturing Technology,* vol. 100, pp. 2915-2927, 2019.

[91] J. Feng, J. Fu, X. Yao and Y. He, "Triply periodic minimal surface (TPMS) porous structures: from multiscale design, precise additive manufacturing to multidisciplinary applications".

[92] G. S. Jung and M. J. Buehler, "Multiscale Mechanics of Triply Periodic Minimal Surfaces of Three-Dimensional Graphene Foams," *Nano Letters,* vol. 18, pp. 4845-4853, 2018.

[93] I. Maskery, L. Sturm, A. Aremu, A. Panesar, C. Williams, C. Tuck, R. Wildman, I. Ashcroft and R. Hague, "Insights into the mechanical properties of several triply periodic minimal surface lattice structures made by polymer additive manufacturing," *Polymer,* vol. 152, pp. 62-71, 2018.

[94] A. P. Castro, T. Pires, J. E. Santos, B. P. Gouveia and P. R. Fernandes, "Permeability versus Design in TPMS Scaffolds," *Materials,* vol. 12, pp. 1-8, 2019.

[95] G. Yu, Z. Li, S. Li, Q. Zhang, Y. Hua, H. Liu, X. Zhao, D. T. Dhaidhai, W. Li and X. Wang, "The select of internal architecture for porous Ti alloy scaffold: A compromise between mechanical properties and permeability," *Materials and Design,* vol. 192, p. 108754, 2020.

[96] J. C. Coimbra, M. A. Martins, P. S. Oliveira and L. A. Minim, "The potential use of a gyroid structure to represent monolithic matrices for bioseparation purposes: Fluid dynamics and mass transfer analysis via CFD," *Separation and Purification Technology,* vol. 254, p. 117594, 2021.

[97] D. Ali and S. Sen, "Finite element analysis of mechanical behaviour, permeability and fluid induced wall shear stress of high porosity scaffolds with gyroid and lattice-based architectures," *Journal of the Mechanical Behaviour of Biomedical Materials,* vol. 75, pp. 262-270, 2017.

[98] K. Michielsen and D. G. Stavenga, "Gyroid cuticular structures in butterfly wing scales: biological photonic crystals," *Journal of the Royal Society Interface,* vol. 5, pp. 85-94, 2008.

[99] V. Saranathan, C. O. Osuji, S. G. J. Mochrie, H. Noh, S. Narayanan, A. Sandy, E. R. Dufresne and R. O. Prum, "Structure, function, and self-assembly of single network gyroid (I4132) photonic crystals in butterfly wing scales," *The Proceedings of the National Academy of Sciences,* vol. 107, no. 26, pp. 11676-11681, 2010.

[100] T. Landh, "From entangled membranes to eclectic morphologies: cubic membranes as subcellular space organizers," *FEBS Letters,* vol. 369, pp. 13-17, 1995.

[101] P. D. Olmsted and S. T. Milner, "Strong Segregation Theory of Bicontinuous Phases in Block Coploymers," *Macromolecules,* vol. 31, pp. 4011-4022, 1998.

[102] F. S. Bates, M. A. Hillmyer, T. P. Lodge, C. M. Bates, K. T. Delaney and G. H. Fredickson, "Mu;tiblock Polymers: Panacea or Pandora's Box?," *Science,* vol. 336, pp. 434-440, 2012.

[103] L. Germain, C. A. Fuentes, A. W. van Vuure, A. des Rieux and C. Dupont-Gillain, "3D-printed biodegradable gyroid scaffolds for tissue engineering applications," *Materials and Design,* vol. 151, pp. 113-122, 2018.

[104] A. P. G. Castro, R. B. Ruben, S. B. GonCalves, J. Pinheiro, J. M. Guedes and P. R. Fernandes, "Numerical and experimental evaluation of TPMS Gyroid Scaffolds for bone tissue engineering," *Computer Methods in Biomechanics and Biomedical Engineering,* vol. 22, no. 6, pp. 567-573, 2019.

[105] X. Dong, A. Heidari, A. Mansouri, W. S. Hao, M. Deghani, S. Saber-Samandari, D. Toghraie and A. Khandan, "Investigation of the mechanical properties of a bony scaffold for comminuted distal radial fractures: Addition of akermanite nanoparticles and using a freeze-drying technique," *Journal of the Mechanical Behavior of Biomedical Materials,* vol. 121, p. 104643, 2021.

[106] J. M. Walker, E. Bodamer, A. Kleinfehn, Y. Luo, M. Becker and D. Dean, "Design and mechanical characterization of solid and highly porous 3D printed poly(propylene fumarate) scaffolds," *Progress in Additive Manufacturing,* vol. 2, pp. 99-108, 2017.

[107] A. L. Olivares, E. Marsal, J. A. Planell and D. Lacroix, "Finite element study of scaffold architecture design and culture conditions for tissue engineering," *Biomaterials,* vol. 30, pp. 6142-6149, 2009.

[108] A. Ataee, Y. Li, D. Fraser, G. Song and C. Wen, "Anisotropic Ti-6Al-4V gyroids scaffolds manufactured by electron beam melting (EBM) for bone implant applications," *Materials and Design,* vol. 137, pp. 345-354, 2018.

[109] A. YAnez, A. Herrera, O. Martel, D. Monopoli and H. Afonso, "Compressive behavious of gyroid lattice structures for human cancellous bone implant applications," *Materials Science and Engineering C,* vol. 68, pp. 445-448, 2016.

[110] C. Yan, L. Hao, A. Hussein and P. Young, "Ti-6Al-4V triply periodic minimal surface structures for bone implants fabricated via selective laser melting," *Journal of the Mechanical Behavior of Biomedical Materials,* vol. 51, pp. 61-73, 2015.

[111] Y. Tripathi, M. Shukla and A. D. Bhatt, "Idealization through interactive modeling and experimental assessment of 3D-printed gyroid for trabecular bone scaffold," *Journal of Engineering in Medicine,* vol. 235, no. 9, pp. 1025-1034, 2021.

[112] Y. Tripathi, M. Shukla and A. D. Bhatt, "Implicit-Function-Based Design and Additive Manufacturing of Triply Perioidic Minimal Surfaces Scaffolds for Bone Tissue Engineering," *Journal of Materials Engineering and Performance,* vol. 28, pp. 7445-7451, 2019.

[113] H. A. Zaharin, A. M. A. Rani, F. I. Azam, T. L. Ginta, N. Sallih, A. Ahmad, N. A. Yunus and T. Z. A. Zulkifli, "Effect of Unit Cell Type and Pore Size on Porosity and Mechanical Behavior of Additively Manufactured Ti6Al4V Scaffolds," *Materials,* vol. 11, pp. 1-15, 2018.

[114] L. Yang, C. Yan, C. Han, P. Chen, S. Yang and Y. Shi, "Mechanical response of a triply periodic minimal surface cellular structures manufactured by selective laser melting," *International Journal of Mechanical Sciences,* vol. 148, pp. 149-157, 2018.

[115] A. Pham, C. Kelly and K. Gall, "Free boundary effects and representative volume elements in 3D printed Ti-^al-4V gyroid structures," *Journal of Materials Research,* vol. 105, pp. 2547-2555, 2020.

[116] S. Ma, Q. Tang, Q. Feng, J. Song, X. Han and F. Guo, "Mechanical behaviours and mass transport properties of bone-mimicking scaffolds consisted of gyroid structures manufactured using selective laser melting," *Journal of the Mechanical Behavior of Biomedical Materials,* vol. 93, pp. 158-169, 2019.

[117] D. W. Abueidda, M. Elhebeary, C.-S. (. Shiang, S. Pang, R. K. Abu Al-Rub and I. M. Jasiuk, "Mechanical propertiesof 3D printed polymeric Gyroid cellular structures: Experimental and finite element study," *Materials and Design,* vol. 165, pp. 1-9, 2019.

[118] L. Wallat, P. Altschuh, M. Reder, B. Nestler and F. Poehler, "Computational Design and Characterisation of Gyroid Structures with Different Gradient Functions for Porosity Adjustment," *Materials,* vol. 15, no. 3730, pp. 1-13, 2022.

[119] C. N. Kelly, J. Francovich, S. Julmi, D. Safranski, R. E. Guldberg, H. J. Maier and K. Gall, "Fatigue behavior os As-built selective laser melted titanium scaffolds with sheet-based gyroid microarchitecture for bone tissue engineering," *Acta Biomaterialia,* vol. 94, pp. 610-626, 2019.

[120] A. Timercan, V. Cheremetyev and V. Brailovski, "Mechanical properties and fluid permeability of gyroid and diamond lattice structures for intervertebral devices: functional requirements and comparative analysis," *Science and Technology of Advanced Materials,* vol. 22, no. 1, pp. 285-300, 2021.

[121] J. N. Reddy, "The Finite Element Method," in *Introduction to the Finite Element Method, Third Edition*, New York City, McGraw-Hill Education, 2006.

[122] A. Ramos and J. A. SimoEs, "Tetrahedral versus hexahedral finite elements in numerical modelling of the proximal femur," *Medical Engineering and Physics,* vol. 28, pp. 916-924, 2006.

[123] Safe Technology Ltf, "Fe-Safe User Manual Volume 2: Fatigue Theory Reference Manual," Safe Technology Ltd, Sheffield, UK, 2017.

[124] Y. Duan, J. A. Gonzalez, P. A. Kulkarni, W. W. Nagy and J. A. Griggs, "Fatigue lifetime prediction of a reduced-diameter dental implant system: Numerical and experimental study," *Dental Materials,* vol. 34, pp. 1299-1309, 2018.

[125] G. Hong, J. Liu, S. F. Cobos, T. Khazaee, M. Drangova and D. W. Holdsworth, "Effective magnetic susceptibility of 3D-printed porous metal scaffolds," *Magentic Resonance in Medicine,* vol. 87, pp. 2947-2956, 2022.

[126] "ISO 13314 Mechanical testing of metals - Ductility testing - Compression test for porous and cellular metals," 2011.

[127] M. J. Reeves, G. S. Athwal, J. A. Johnson and D. G. Langohr, "The Effect of Inhomogenous Trabecular Stiffness Relationship Selection on Finite Element Outcomeds for Shoulder Arthroplasty," *Journal of Biomechanical Engineering,* vol. 141, p. 034501, 2019.

[128] R. Boyer, G. Welsch and E. W. Collings, Material Properties Handbook: Titanium Alloys, ASM International, 1994.

[129] O. Yetik, H. Kocoglu, Y. Y. Avcu, E. Avcu and T. SinmazCelik, "The Effects of Grit Size and Blasting Pressure on the Surface Properties of Grit Blasted Ti6Al4V Alloy," *Materials Today: Proceedings,* vol. 32, pp. 27-36, 2020.

[130] D. Shia and K. Yamaguchi, "Infection After Total Shoulder Arthroplasty," *Seminars in Arthroplasty,* vol. 18, pp. 85-88, 2007.

[131] M. T. Tan, J. W. Read and D. J. Bokor, "Does proximal porous coating in short-stem humeral arthroplasty reduce stress shielding?," *Shoulder & Elbow,* vol. 11, pp. 56-66, 2019.

[132] P. Soltanmohammadi, J. Elwell, V. Veeraghavan, G. S. Athwal and R. Willing, "Investigating the Effects of Demographics on Shoulder Morphology and Density Using Statisitical Shape and Density Modeling," *Journal of Biomechanical Engineering,* vol. 142, p. 121005, 2020.

[133] J. A. Grant, N. E. Bishop, N. GOtzen, C. Sprecher, M. Honl and M. M. Morlock, "Artificial compositie bone as a model of human trabecular bone: The implant-bone interface," *Journal of Biomechanics,* vol. 40, pp. 1158-1164, 2007.

[134] G. Bergmann, F. Grauchen, A. Bender, M. KAAB, A. Rohlmann and P. Westerhoff, "In vivo glenohumeral contact forces - Measurements in the first patient 7 months postoperatively," *Journal of Biomechanics,* vol. 40, pp. 2139-2149, 2007.

[135] M. A. Neuert and C. E. Dunning, "Determination of remodeling parameters for a strain-adaptive finite element model of the distal ulna," *Journal of Engineering in Medicine,* vol. 227, no. 9, pp. 994-1001, 2013.

[136] C. N. Kelly, T. Wang, J. Crowley, D. Wills, M. H. Pelletier, E. R. Westrick, S. B. Adams, K. Gall and W. R. Walsh, "High-strength, porous additively manufactured implants with optimized mechanical osseointegration," *Biomaterials,* vol. 121206, p. 279, 2021.

[137] W. Anderson, "Development of a Wireless Telemetry Load and Displacement Sensor for Orthopaedics Applications," Western Graduate & Postdoctoral Studies, London, Ontario, 2021.

5 Appendices

5.1 Netgen Gyroid Meshing Parameters

The following meshing parameters (Table 5-1) were used for all five gyroid cylinders and all three gyroid humeral stems.

Table 5-1. Netgen meshing parameters used for the gyroid cylinder and humeral stems.

Parameter	Mesh-size grading	Elements per curvature radius	Elements per edge
Value	0.175	4.0	3.0

Mesh-size grading is a defined value in the range of 0.1-1.0 where a smaller value results in a finer mesh. Element per edge and element per curvature radius are defined values in the range of 0.2-10.0 where a smaller value results in a coarser mesh.

5.2 Video Extensometer Calibration and Validation

Before the video extensometer could be used for strain measurement during testing, it needed to be calibrated (Figure 5-1). The calibration bar consists of a matrix of black dots which are 6 mm away from each adjacent vertical and horizontal dot. This calibration bar is placed between the load cell and the actuator (in the same location as the testing specimens) so that it is vertical and centralized within the image window on the computer (Figure 5-2). If the video extensometer measures the vertical and horizontal dots as being 6 mm apart, the system is then calibrated.

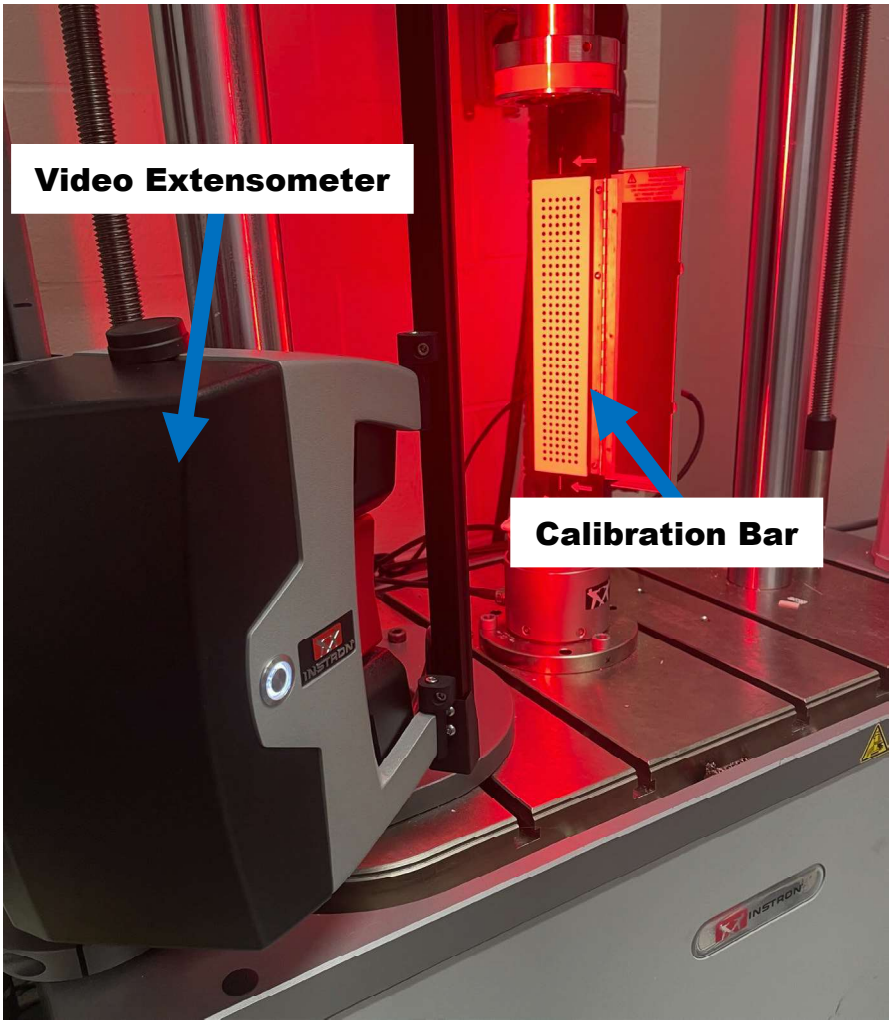

Figure 5-1. Set-up for the calibration of the video extensometer before the static compression testing.

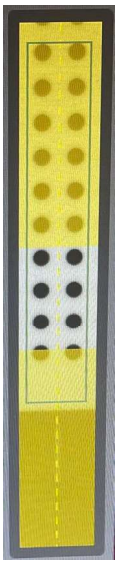

Figure 5-2. Image window on the computer displaying the matrix of black dots from the calibration bar in the camera's field of view.

To further validate the strain measurements, two marks were placed on either end of one gyroid specimen, just as during testing. The gyroid specimen was attached to the actuator and the specimen was moved upwards along the camera's entire field of view (FOV). No force was applied to the specimen and therefore no strain occurred. The strain was measured between the two markers for the duration of this movement to observe any errors in the strain measurement. Throughout the entire movement, the strain measured between 0.06% and -0.08%.

5.3 Fe-Safe Settings

The .odb file produced by the static analysis in Abaqus was loaded into the Fe-Safe software. The resultant stresses and strains, at the integration points of each element were imported. One loading cycle is defined from 10% of the maximum load to 100% of the maximum load to simulate the loading ratio used in the experimental tests. As Abaqus is a dimensionless software, the property units were defined before analysis (Figure 5-3).

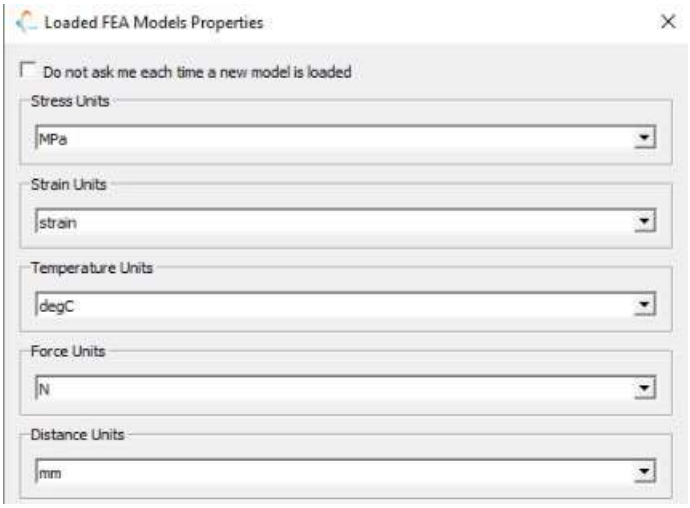

Figure 5-3. Units defined for the loaded finite element model properties.

Fe-safe approximated the material's fatigue properties (Table 5-2) from its ultimate tensile strength (950 MPa for Ti-6Al-4V) and Young's modulus (110 GPa for Ti-6Al-4V), using Seeger's method [123]. The surface finish was also considered by defining the Roughness Average (Ra) to be between 1.6μm and 4μm, aligning with reported values for grit-blasted Ti6Al4V [129].

Table 5-2. Fatigue properties estimated for Ti-6Al-4V using Seeger's method. All of the fatigue parameters are a constant value for all titanium alloys except for the cyclic strain hardening coefficient and the fatigue strength coefficient which are dependent on the defined ultimate tensile strength.

Fatigue Parameter	Symbol	Equation	Estimated Value
Cyclic strain hardening coefficient	K'	K' = $1.61\sigma_{uts}$	1529.5 MPa
Cyclic strain hardening exponent	n'	n' = 0.11	0.11
Basquin's fatigue strength exponent	b	b = -0.095	-0.095
Coffin-Manson fatigue ductility exponent	c	c = -0.69	-0.69
Fatigue ductility coefficient	ε_f'	ε_f' = 0.35	0.35
Fatigue strength coefficient	σ_f'	σ_f' = $1.67\sigma_{uts}$	1586.5 MPa

Fe-safe used these fatigue parameters and calculated the fatigue predictions using the following Normal Strain-Morrow equations:

$$\frac{\Delta\varepsilon}{2} = \frac{\left(\sigma_f' - \sigma_m\right)}{E}\left(2N_f\right)^b + \varepsilon_f{}'\left(2N_f\right)^c$$

$$damage = \frac{1}{N_f}$$

$$life\ in\ repeats = \frac{1}{\sum\frac{1}{N_f}}$$

Where $\Delta\varepsilon$ is the strain range for the cycle, σ_m is the mean stress in the cycle, $2N_f$ is the endurance in reversals.

5.4 Printed Gyroid Porosity Calculations

Table 5-3. Measured masses of each 3D printed gyroid specimen.

Printed Specimen Masses [g]						
Specimen	1	2	3	4	5	6
60P	22.973	22.805	22.717	23.114	23.100	23.133
70P	19.096	18.782	18.992	19.125	19.122	N/A
80P	15.701	15.756	15.794	15.772	15.496	N/A
85P	14.062	14.024	14.002	13.757	14.014	N/A
90P	12.203	12.218	12.144	12.000	12.191	12.168

Table 5-4. Independent Variables used in porosity calculations.

Variable	Symbol	Value
Volume of end cap (based on CAD model)	V_{endcap}	1.0915 cm^3
Density of Ti6Al4V	ρ	4.28 g/cm^3
Volume of solid cylinder	Volume $_{Solid\ Cylinder}$	8.898 cm^3

$$m_{avg} = \frac{\sum_{i=1}^{n} m_i}{n}$$

$$m_{cone} = V_{endcap} \times \rho$$

$$Volume_{Actual} = \frac{m_{avg} - 2(m_{cone})}{\rho}$$

$$Actual\ Porosity = \left[1 - \frac{Volume_{Actual}}{Volume_{Solid\ Cylinder}}\right] \times 100$$

Example Calculation (60P Specimens):

$$m_{avg} = \frac{22.973g + 22.805g + 22.717g + 23.114g + 23.100g + 23.133g}{6}$$

$$m_{avg} = 22.974\ g$$

$$m_{cone} = (1.0915\ cm^3)(4.28\ g/cm^3)$$

$$m_{cone} = 4.671\ g$$

$$Volume_{Actual} = \frac{(22.974g) - 2(4.671g)}{4.28g/cm^3}$$

$$Volume_{Actual} = 3.185\ cm^3$$

$$Actual\ Porosity = \left[1 - \frac{3.185\ cm^3}{8.898\ cm^3}\right] \times 100$$

$$Actual\ Porosity = 64.21\%$$

5.5 Static Compression Figures

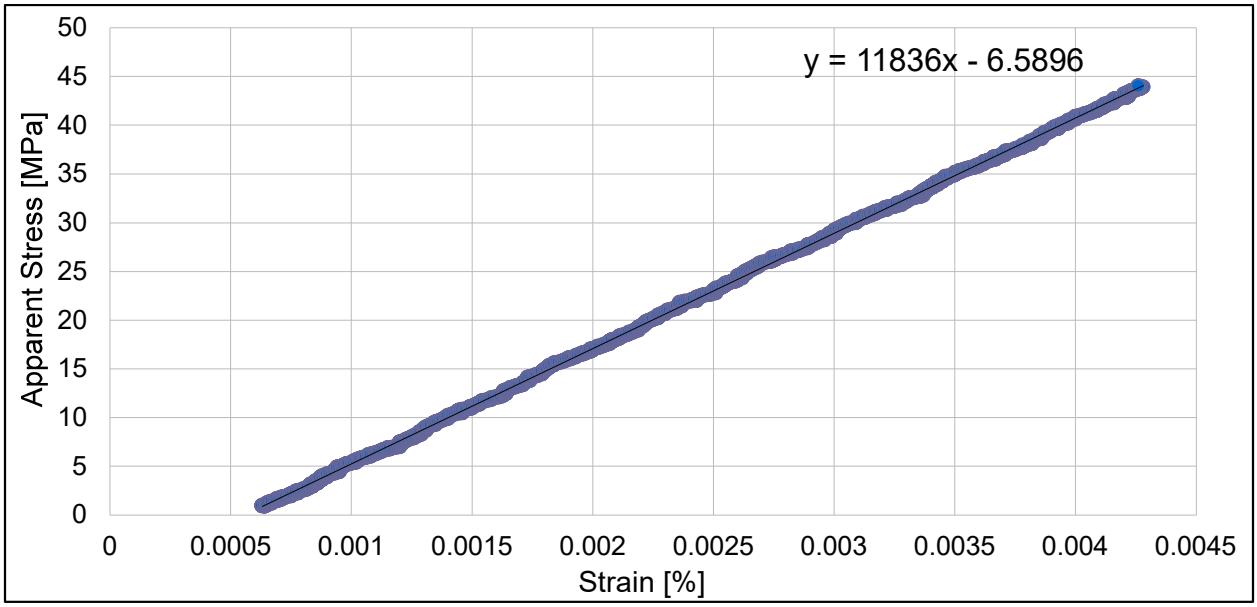

Figure 5-4. Apparent Stress versus Strain for the static compression test of the 60P cylinder: specimen #1. The apparent stress is equal to the applied load over the area of a 17 mm diameter circle (diameter of the cylinder). Strain was measured using a video extensometer and is the change in length over the original length of the cylinder. The apparent modulus elasticity is equal to the apparent stress over strain also known as the slope of the equation of the linear line.

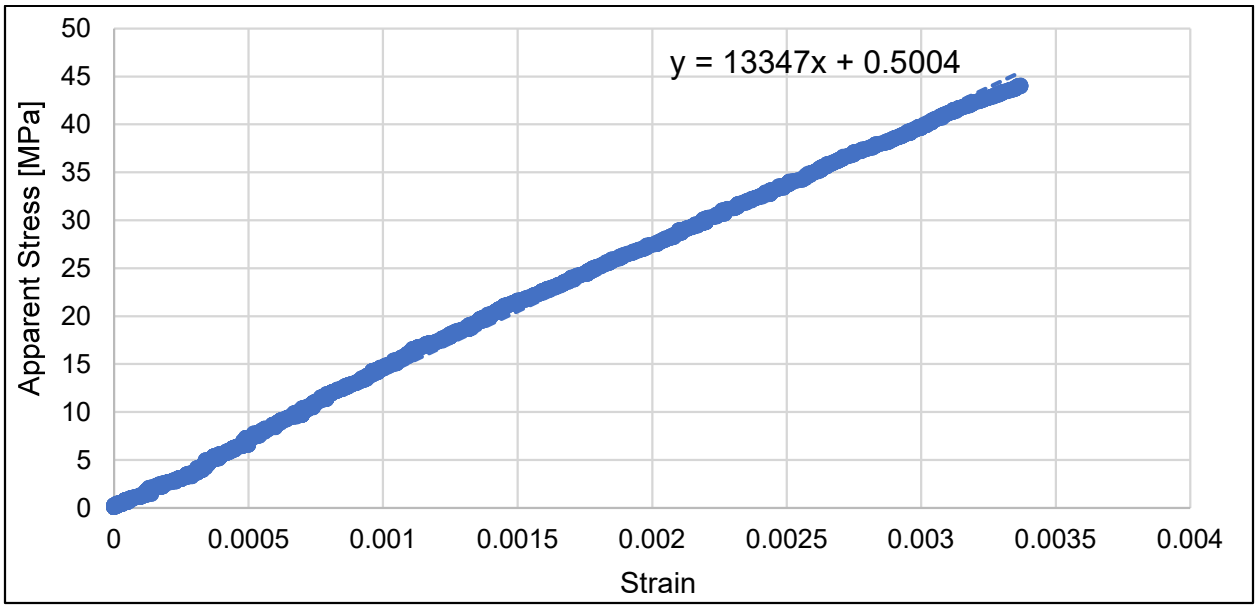

Figure 5-5. Apparent Stress versus Strain for the static compression test of the 60P cylinder: specimen #2. The apparent stress is equal to the applied load over the area of a 17 mm diameter circle (diameter of the cylinder). Strain was measured using a video extensometer and is the change in length over the original length of the cylinder. The apparent modulus elasticity is equal to the apparent stress over strain also known as the slope of the equation of the linear line.

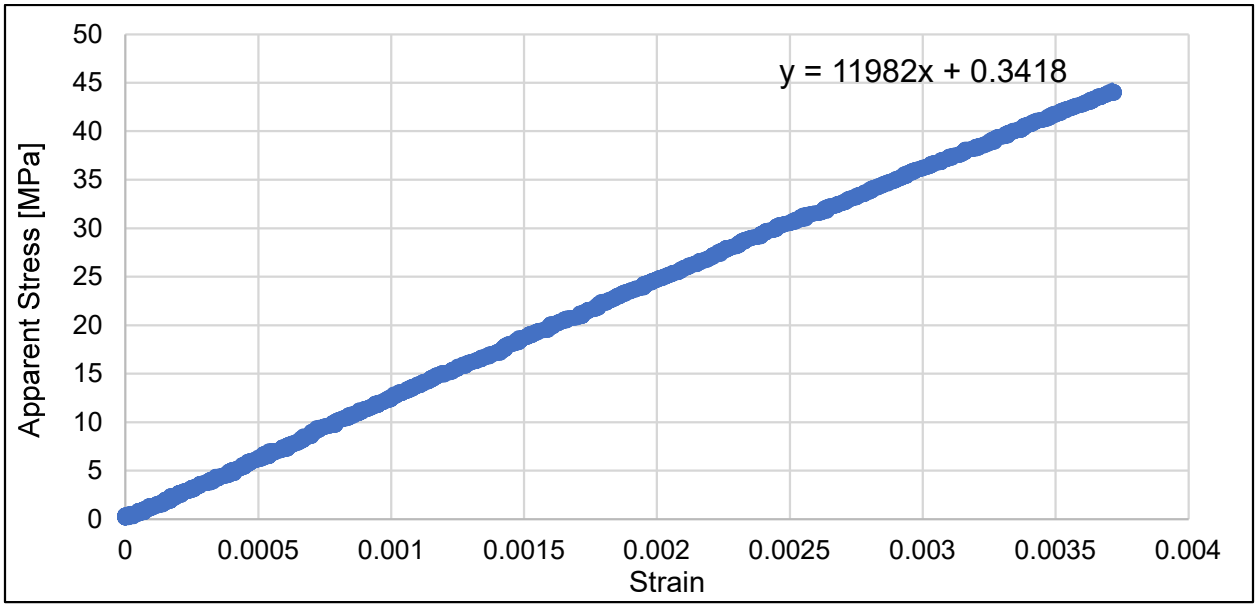

Figure 5-6. Apparent Stress versus Strain for the static compression test of the 60P cylinder: specimen #3. The apparent stress is equal to the applied load over the area of a 17 mm diameter circle (diameter of the cylinder). Strain was measured using a video extensometer and is the change in length over the original length of the cylinder. The apparent modulus elasticity is equal to the apparent stress over strain also known as the slope of the equation of the linear line.

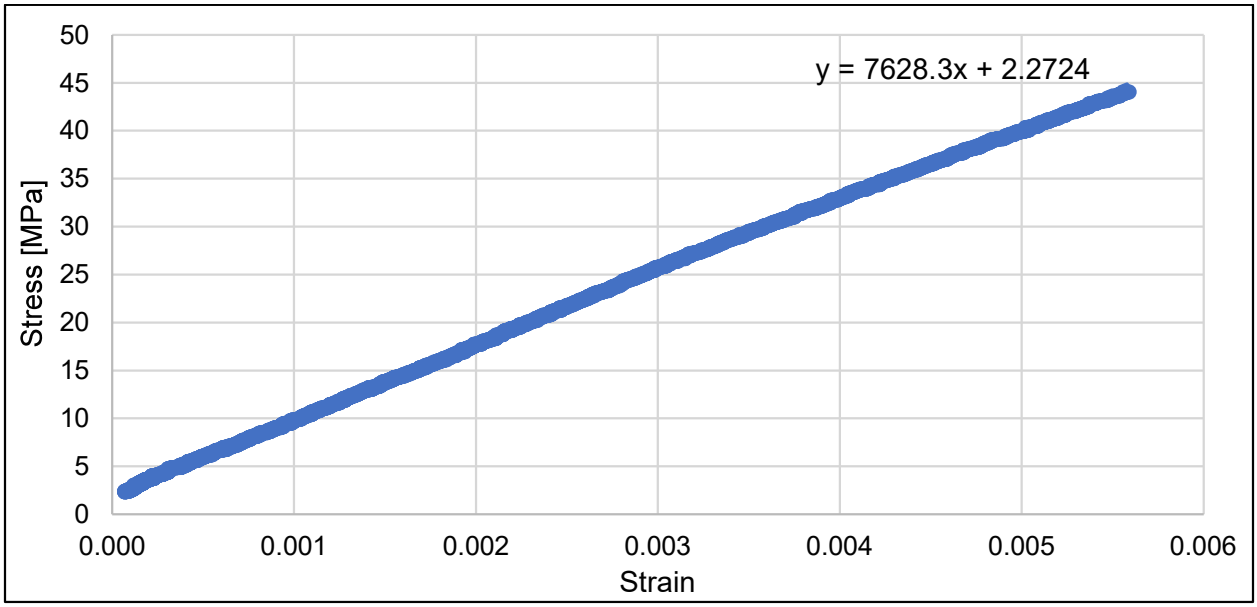

Figure 5-7. Apparent Stress versus Strain for the static compression test of the 70P cylinder specimen. The apparent stress is equal to the applied load over the area of a 17 mm diameter circle (diameter of the cylinder). Strain was measured using a video extensometer and is the change in length over the original length of the cylinder. The apparent modulus elasticity is equal to the apparent stress over strain also known as the slope of the equation of the linear line.

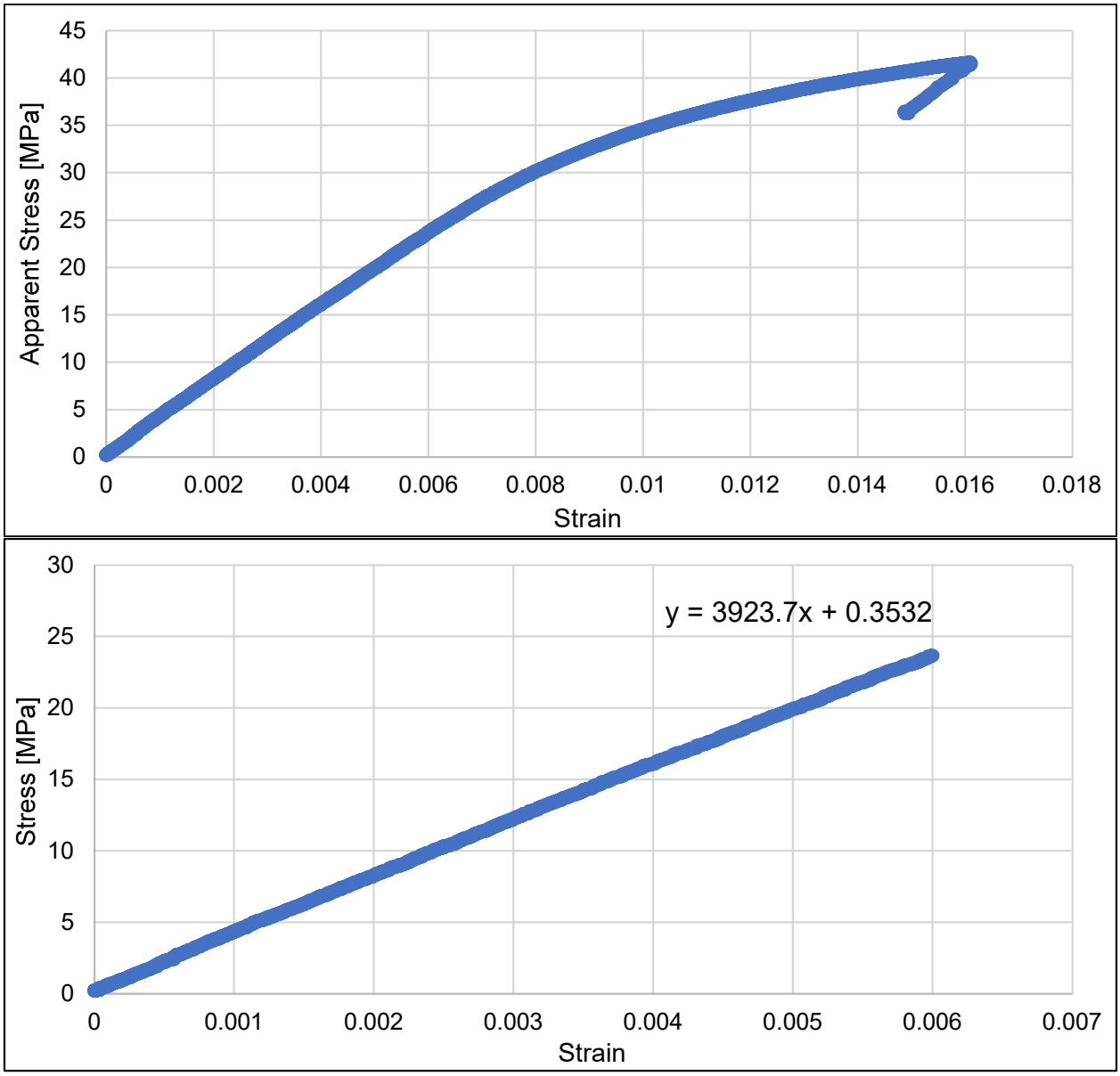

Figure 5-8. Apparent Stress versus Strain for the static compression test of the 80P cylinder specimen for the whole test (top) and just the linear elastic region (bottom). The apparent stress is equal to the applied load over the area of a 17 mm diameter circle (diameter of the cylinder). Strain was measured using a video extensometer and is the change in length over the original length of the cylinder. The apparent modulus elasticity is equal to the apparent stress over strain (in the bottom graph) also known as the slope of the equation of the linear line.

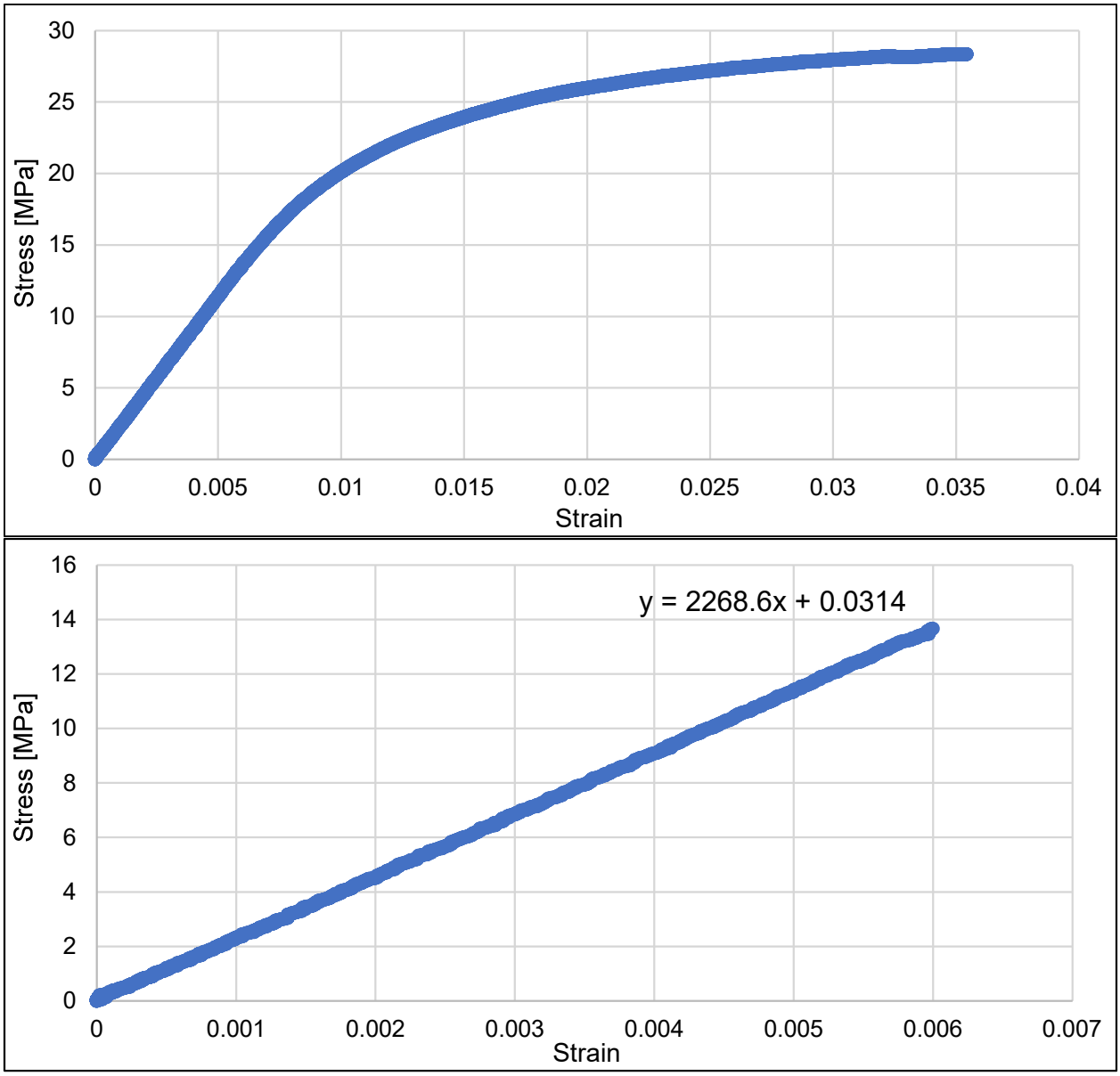

Figure 5-9. Apparent Stress versus Strain for the static compression test of the 85P cylinder specimen for the whole test (top) and just the linear elastic region (bottom). The apparent stress is equal to the applied load over the area of a 17 mm diameter circle (diameter of the cylinder). Strain was measured using a video extensometer and is the change in length over the original length of the cylinder. The apparent modulus elasticity is equal to the apparent stress over strain (in the bottom graph) also known as the slope of the equation of the linear line.

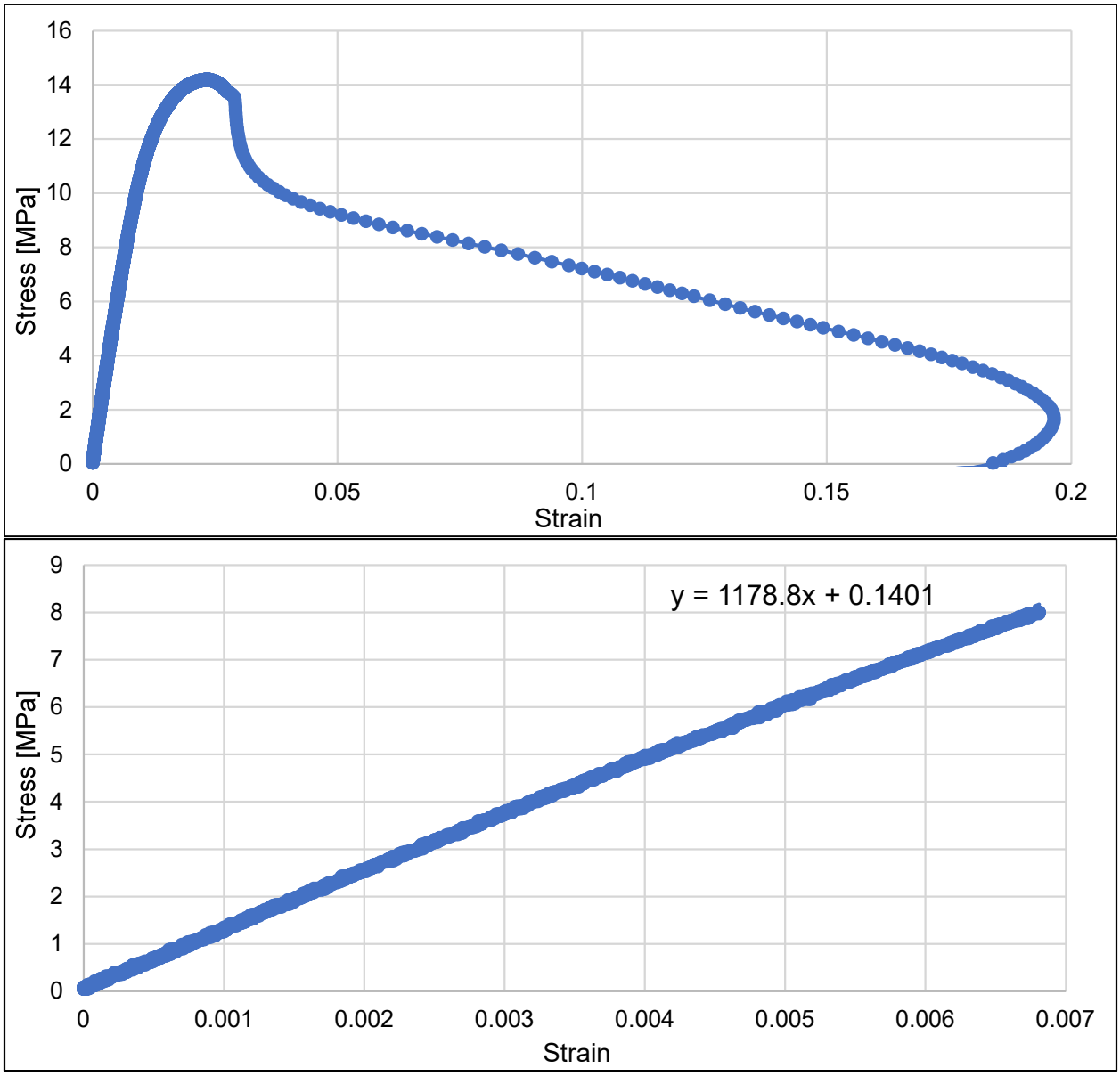

Figure 5-10. Apparent Stress versus Strain for the static compression test of the 90P cylinder specimen for the whole test (top) and just the linear elastic region (bottom). The apparent stress is equal to the applied load over the area of a 17 mm diameter circle (diameter of the cylinder). Strain was measured using a video extensometer and is the change in length over the original length of the cylinder. The apparent modulus elasticity is equal to the apparent stress over strain (in the bottom graph) also known as the slope of the equation of the linear line.

5.6 Fatigue Testing Specimens

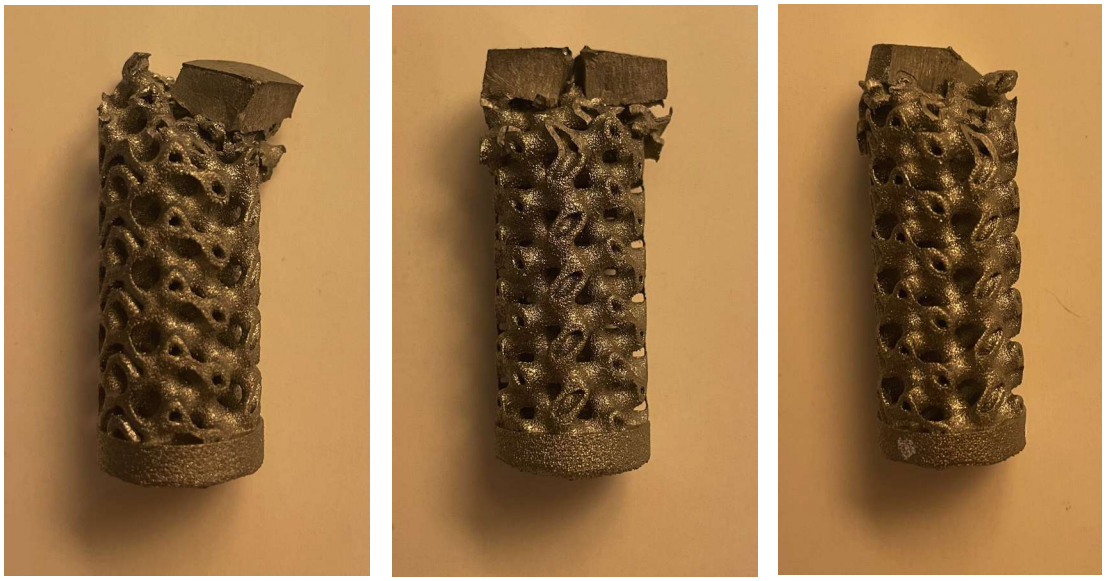

Figure 5-11. 60P specimens after fatigue testing. All specimens were tested at the same maximum load (~45% of their yield force).

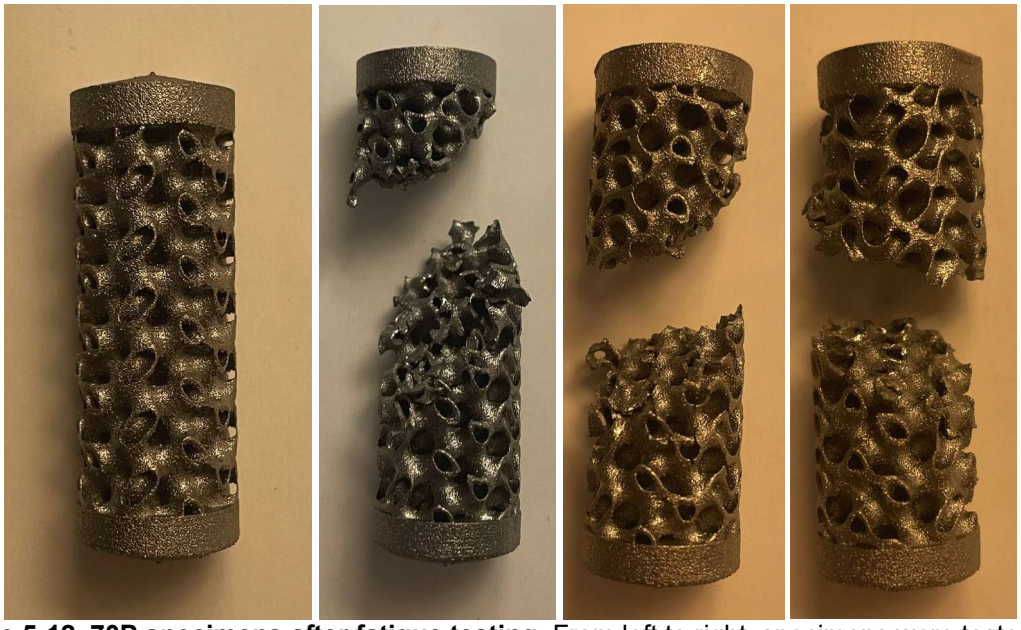

Figure 5-12. 70P specimens after fatigue testing. From left to right, specimens were tested at a maximum applied load of 50%, 65%, 70%, and 75% of their yield force.

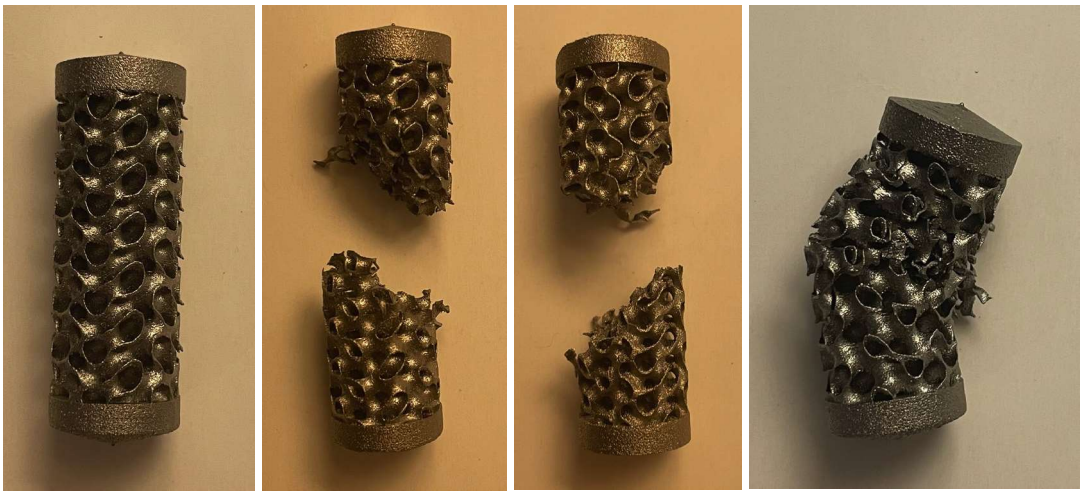

Figure 5-13. 80P specimens after fatigue testing. From left to right, specimens were tested at a maximum applied load of 50%, 70%, 80%, and 90% of their yield force.

Figure 5-14. 85P specimens after fatigue testing. From left to right, specimens were tested at a maximum applied load of 50%, 70%, 80%, and 90% of their yield force.

Figure 5-15. 90P specimens after fatigue testing. From left to right, specimens were tested at a maximum applied load of 50%, 70%, 80%, and 90% of their yield force.

5.7 Mechanobiology Outcome Figures for Individual Loading Conditions

5.7.1 Change in Von Mises Stress

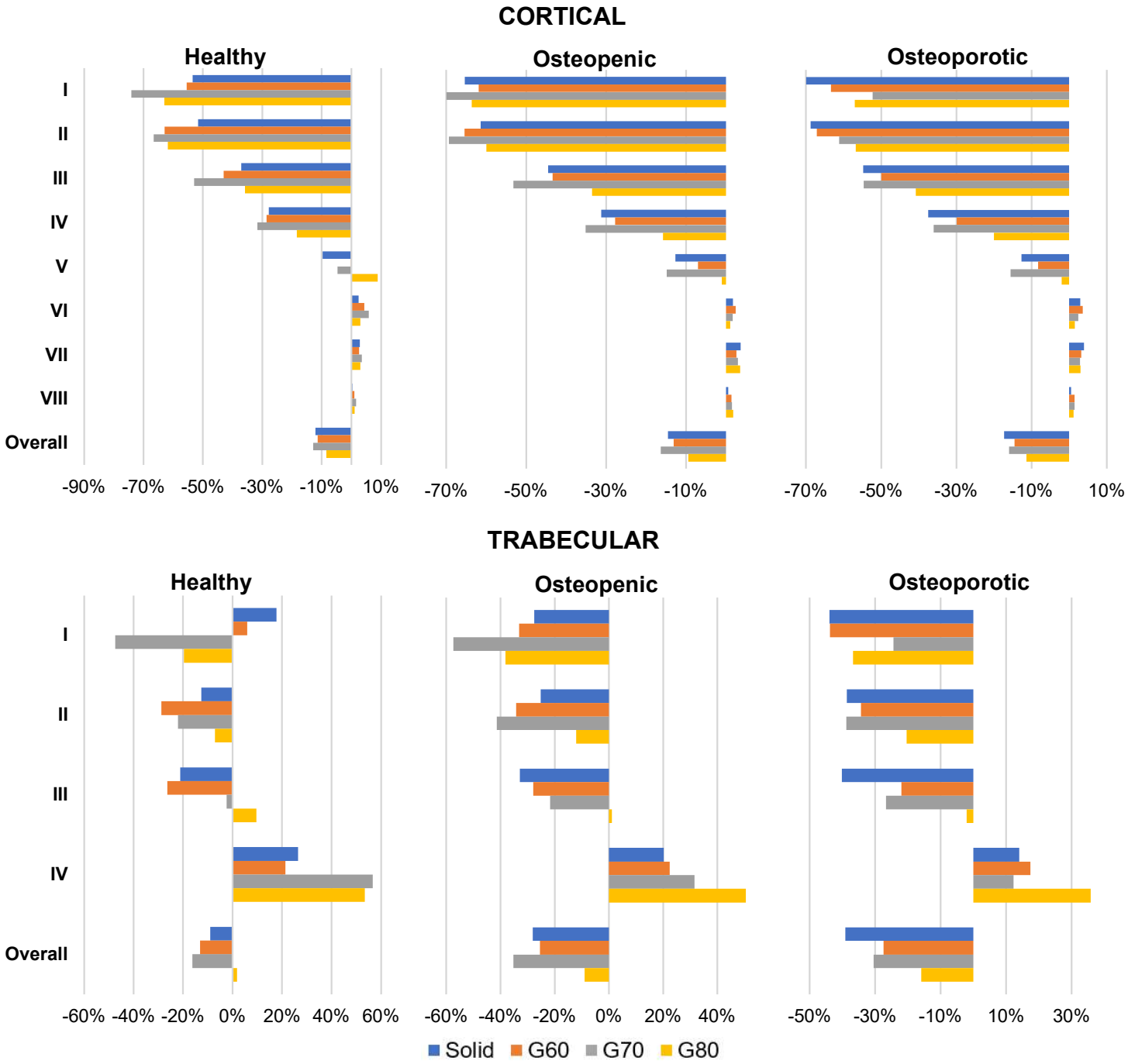

Figure 5-16. Volume-weighted average in the magnitude of Von Mises stress for the reconstructed bone as a percentage of the intact bone by slice and overall proximal 80mm (cortical) and 40mm (trabecular). 45° of abduction loading condition.

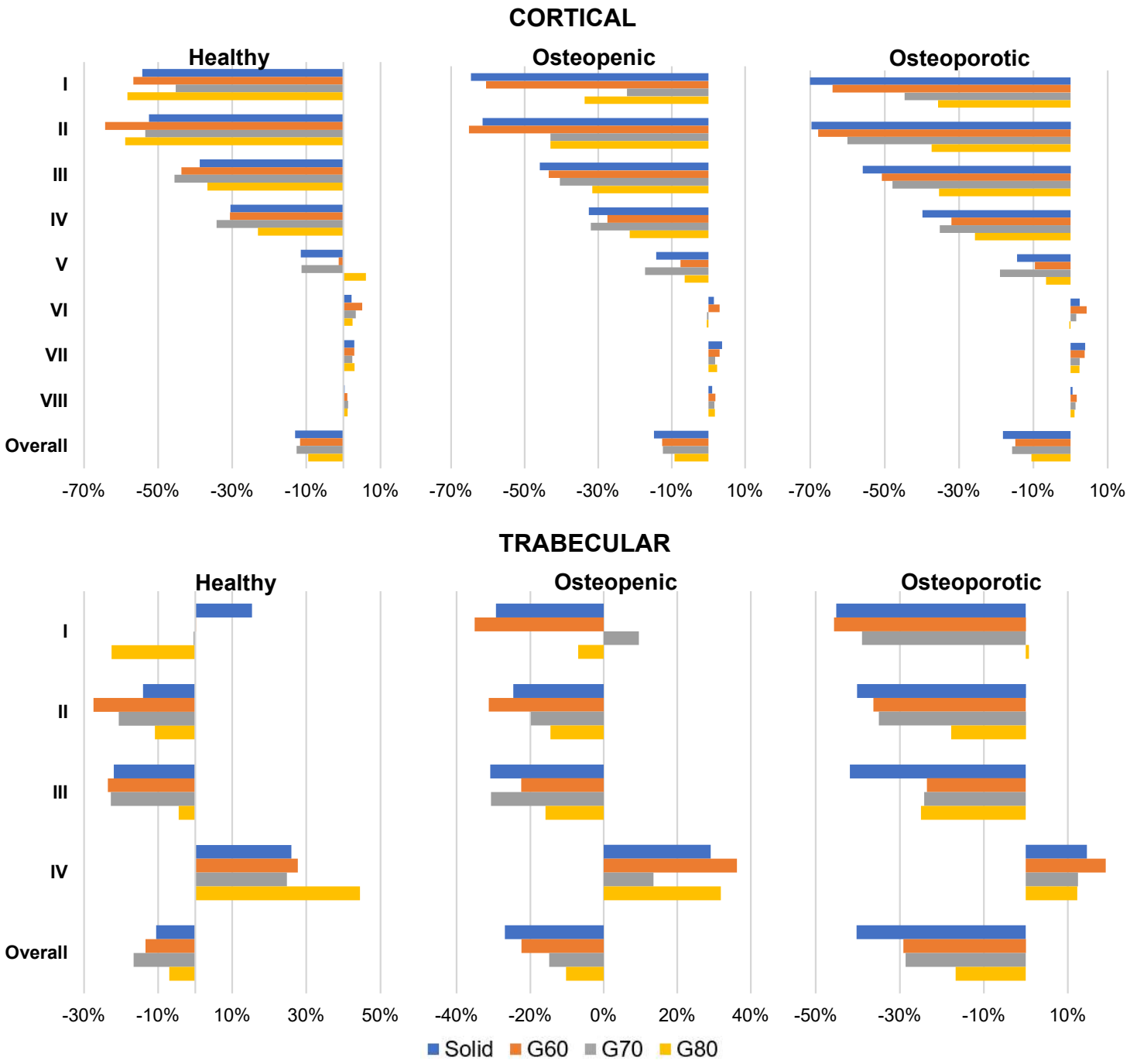

Figure 5-17. Volume-weighted average in the magnitude of Von Mises stress for the reconstructed bone as a percentage of the intact bone by slice and overall proximal 80mm (cortical) and 40mm (trabecular). 75° of abduction loading condition.

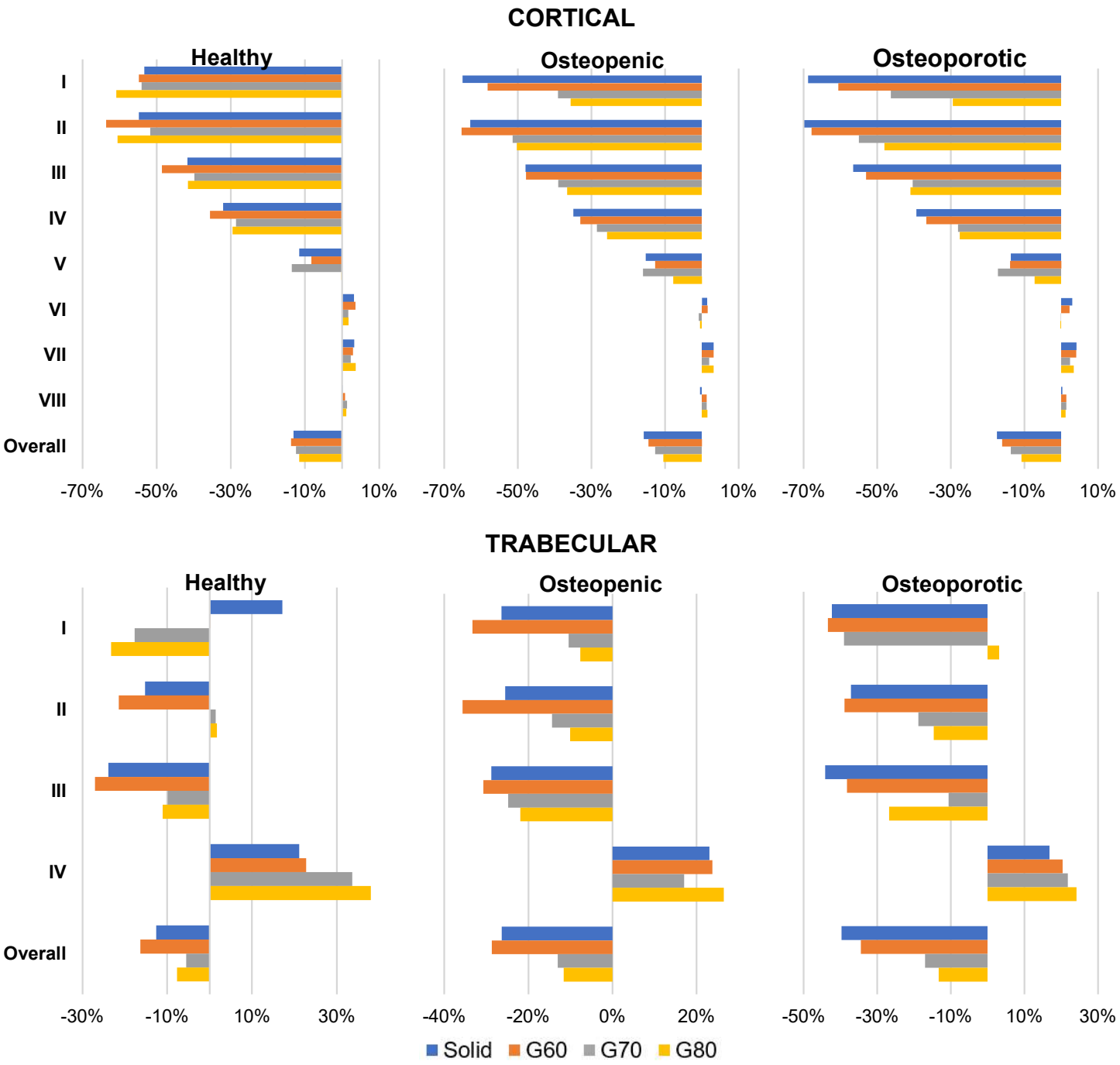

Figure 5-18. Volume-weighted average in the magnitude of Von Mises stress for the reconstructed bone as a percentage of the intact bone by slice and overall proximal 80mm (cortical) and 40mm (trabecular). 90° of flexion loading condition.

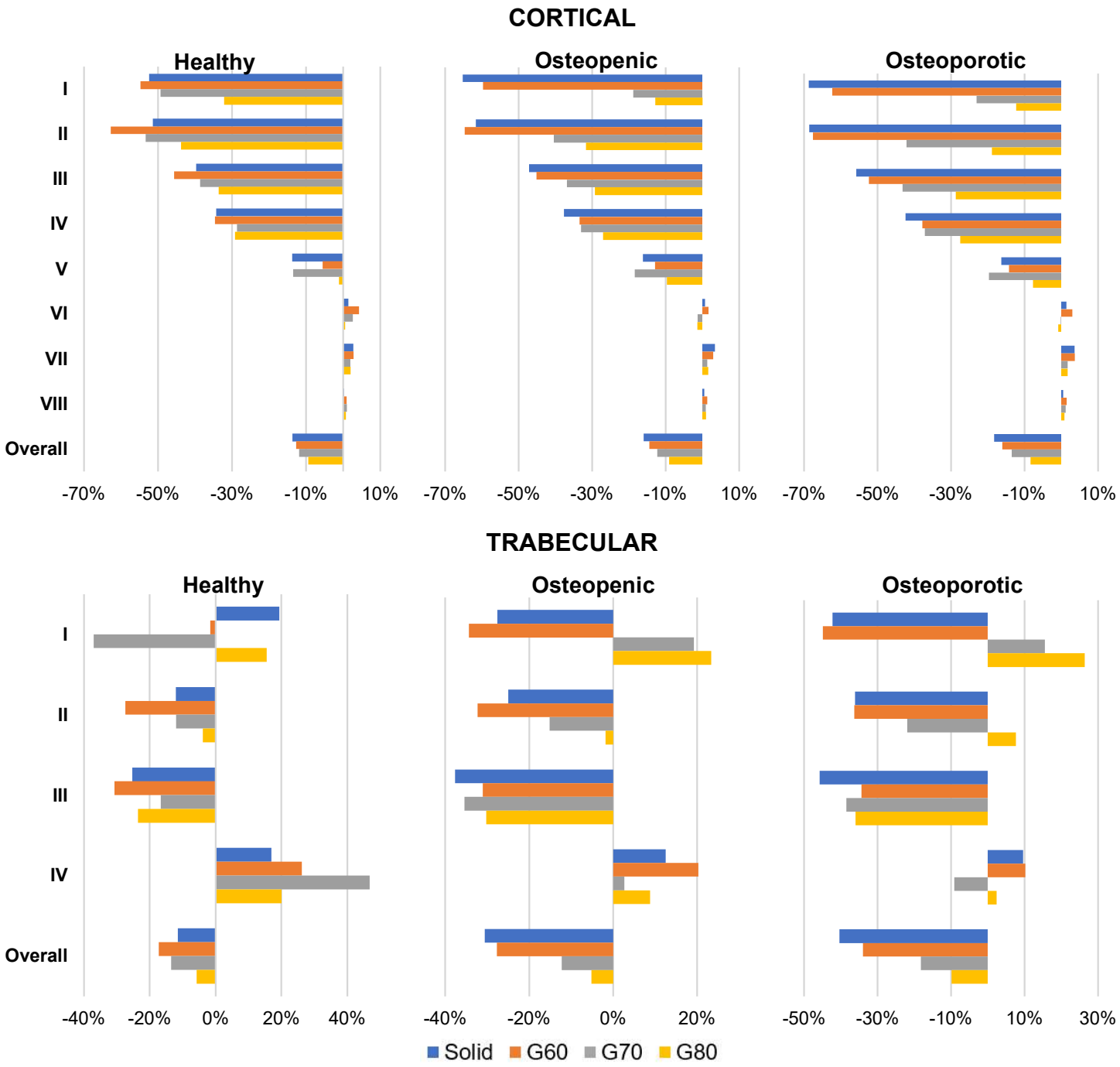

Figure 5-19. Volume-weighted average in the magnitude of Von Mises stress for the reconstructed bone as a percentage of the intact bone by slice and overall proximal 80mm (cortical) and 40mm (trabecular). 120° of flexion loading condition.

5.7.2 Deviatoric Change in Stress

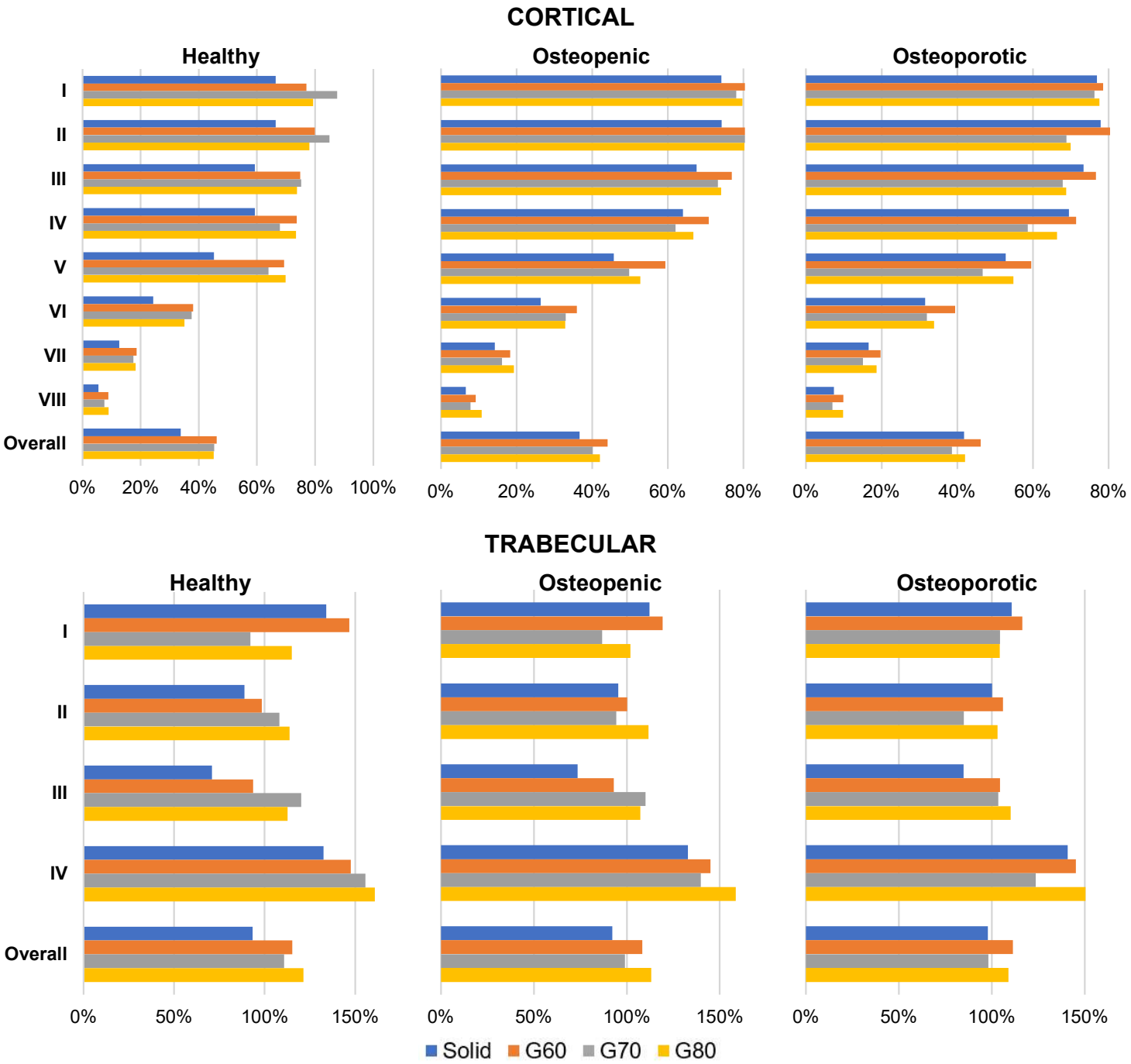

Figure 5-20. Volume-weighted deviatoric change in stress tensor for the reconstructed bone as a percentage of the intact bone by slice and overall proximal 80mm (cortical) and 40mm (trabecular). 45° of abduction loading condition.

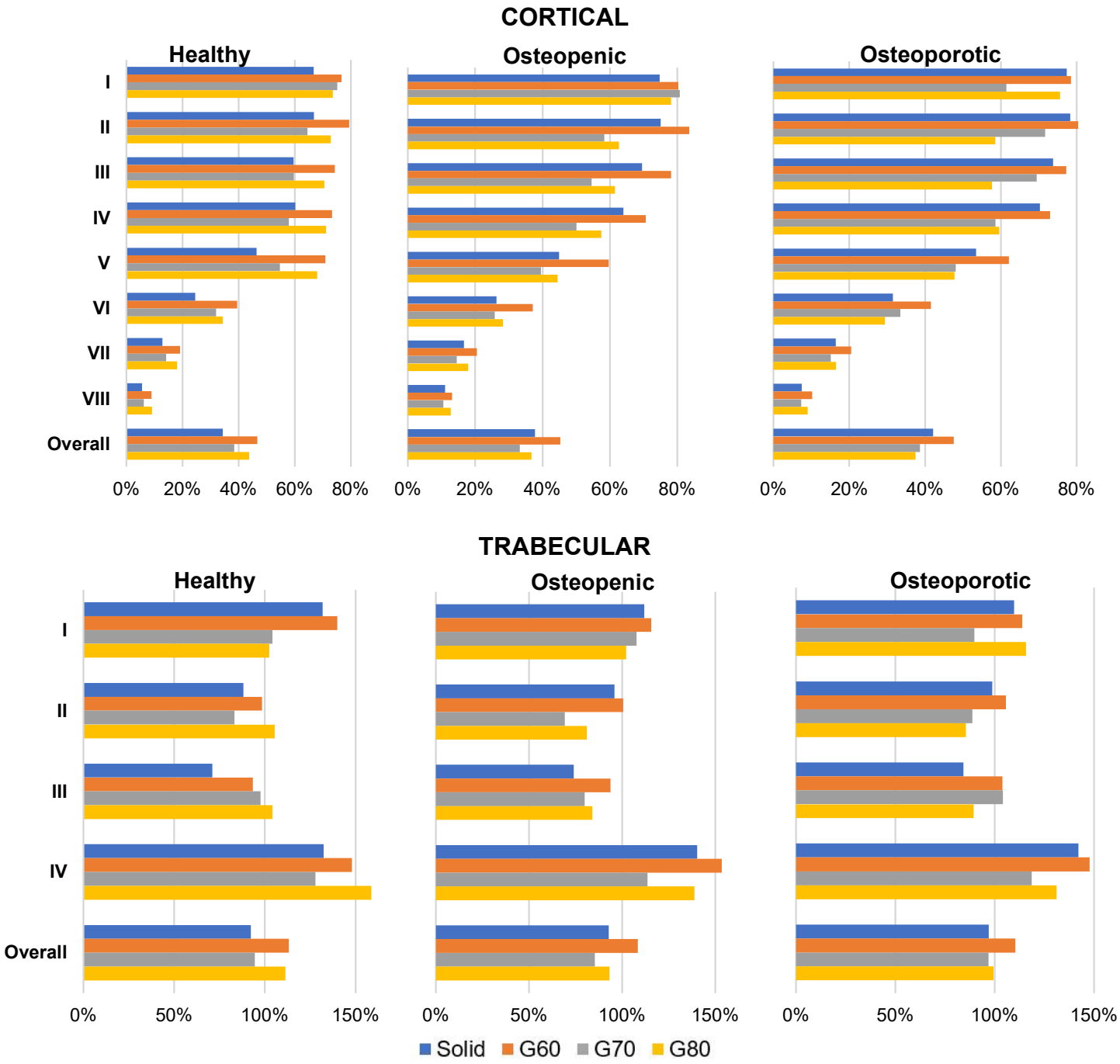

Figure 5-21. Volume-weighted deviatoric change in stress tensor for the reconstructed bone as a percentage of the intact bone by slice and overall proximal 80mm (cortical) and 40mm (trabecular). 75° of abduction loading condition.

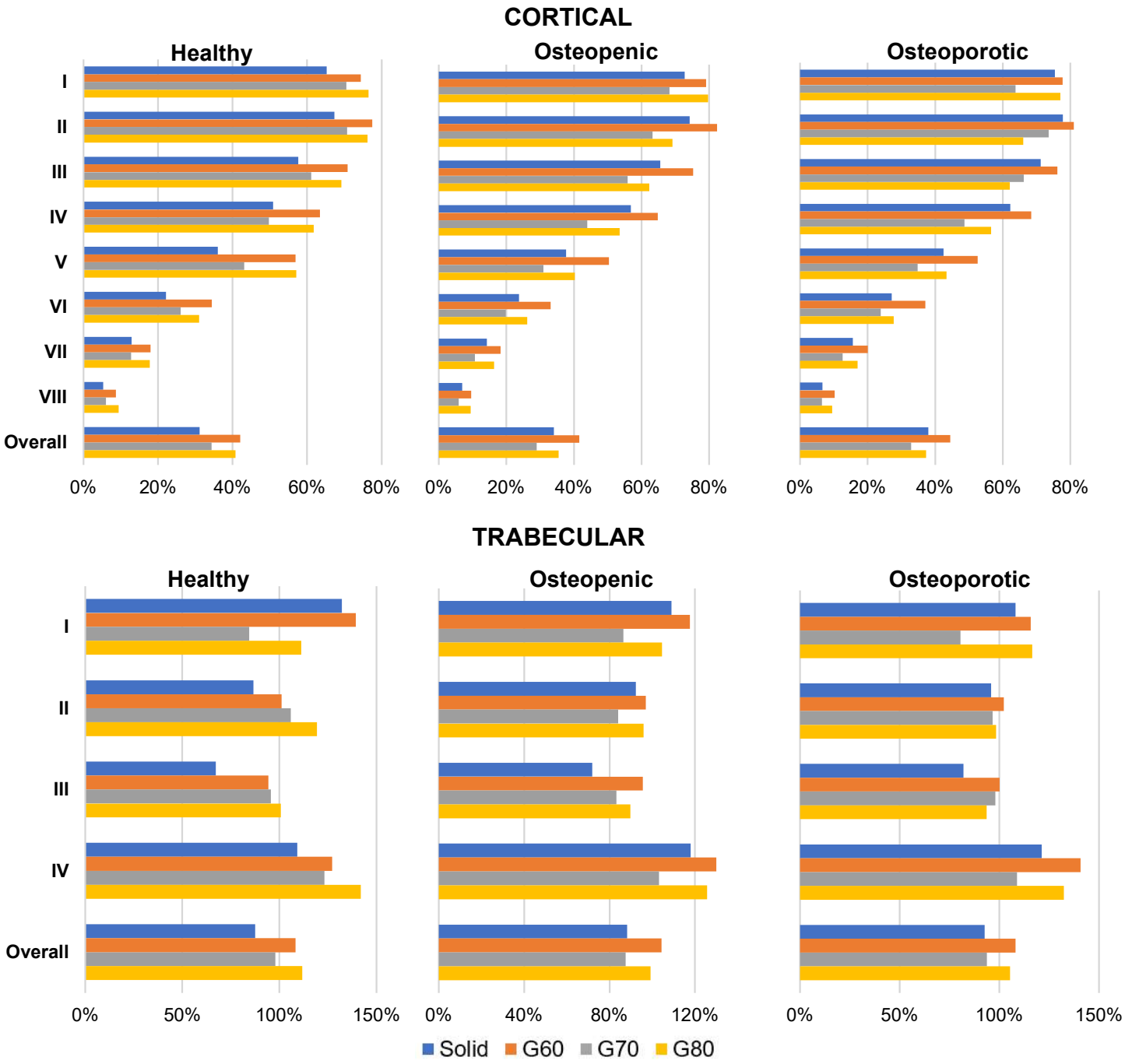

Figure 5-22. Volume-weighted deviatoric change in stress tensor for the reconstructed bone as a percentage of the intact bone by slice and overall proximal 80mm (cortical) and 40mm (trabecular). 90° of flexion loading condition.

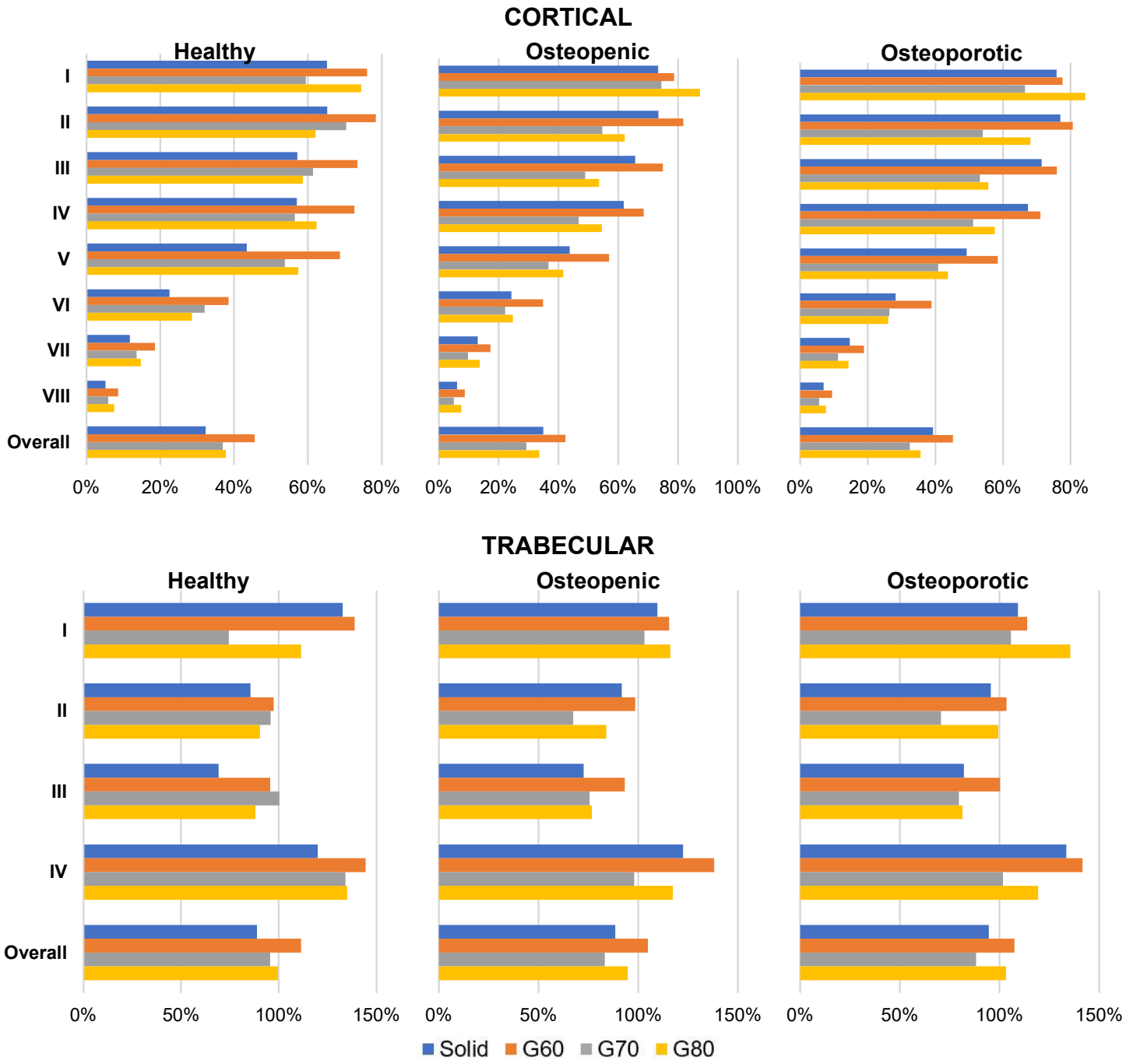

Figure 5-23. Volume-weighted deviatoric change in stress tensor for the reconstructed bone as a percentage of the intact bone by slice and overall proximal 80mm (cortical) and 40mm (trabecular). 120° of flexion loading condition.

5.7.3 Percentage of Bone Resorption/Formation

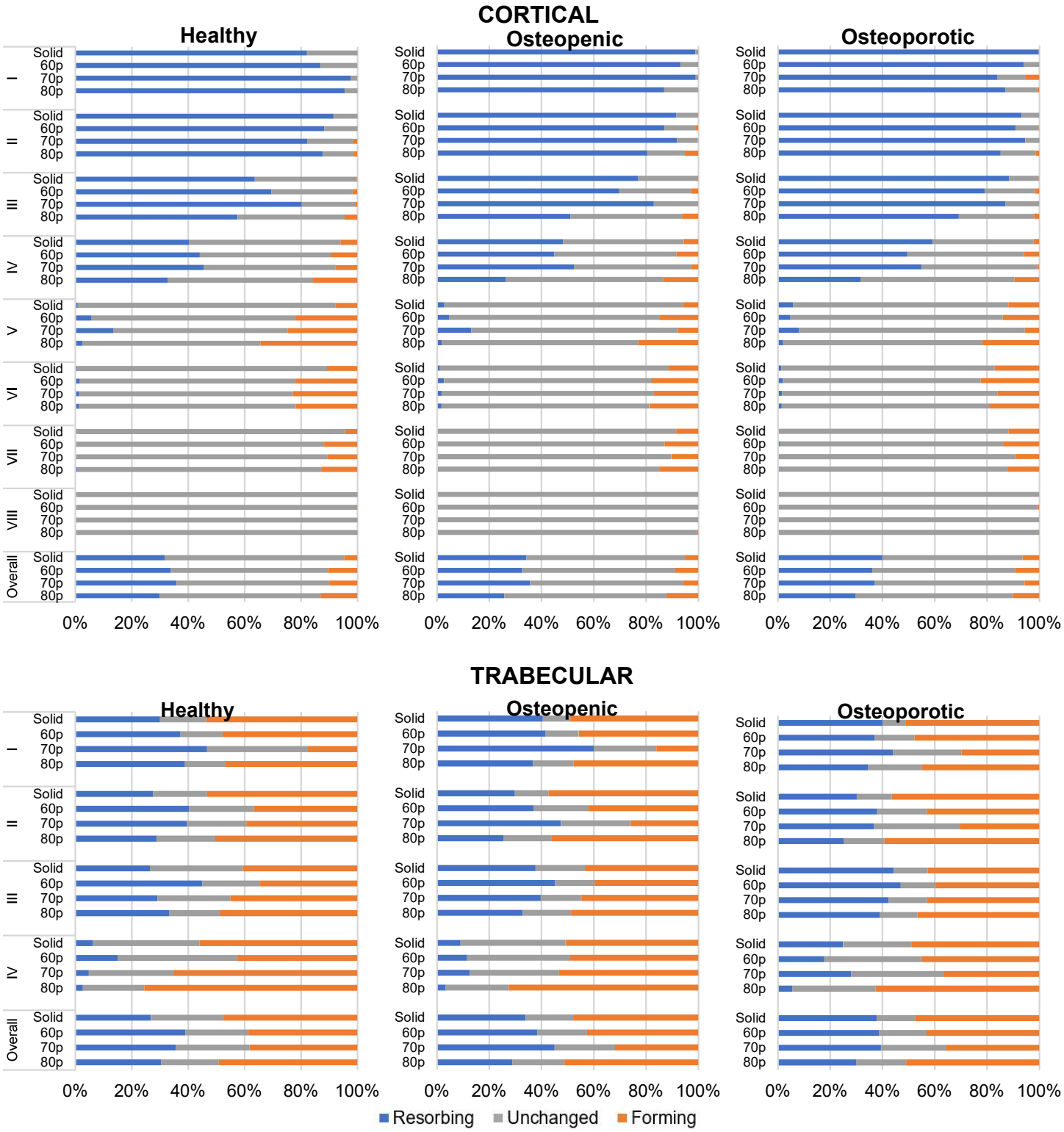

Figure 5-24. Volume percentage of bone resorption/formation in the reconstructed bones by slice and overall proximal 80mm (cortical) and 40mm (trabecular). 45° of abduction loading condition.

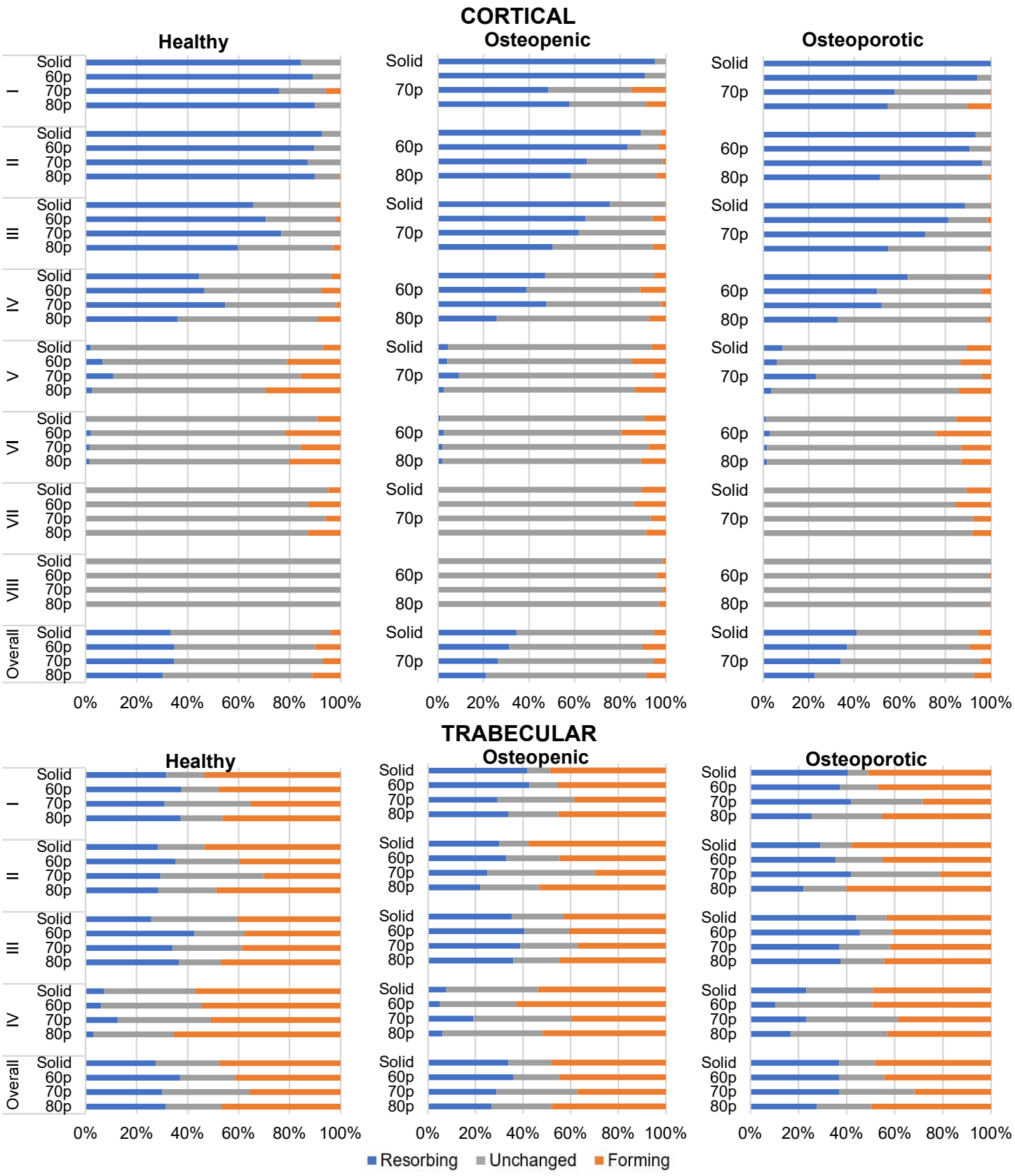

Figure 5-25. Volume percentage of bone resorption/formation in the reconstructed bones by slice and overall proximal 80mm (cortical) and 40mm (trabecular). 75° of abduction loading condition.

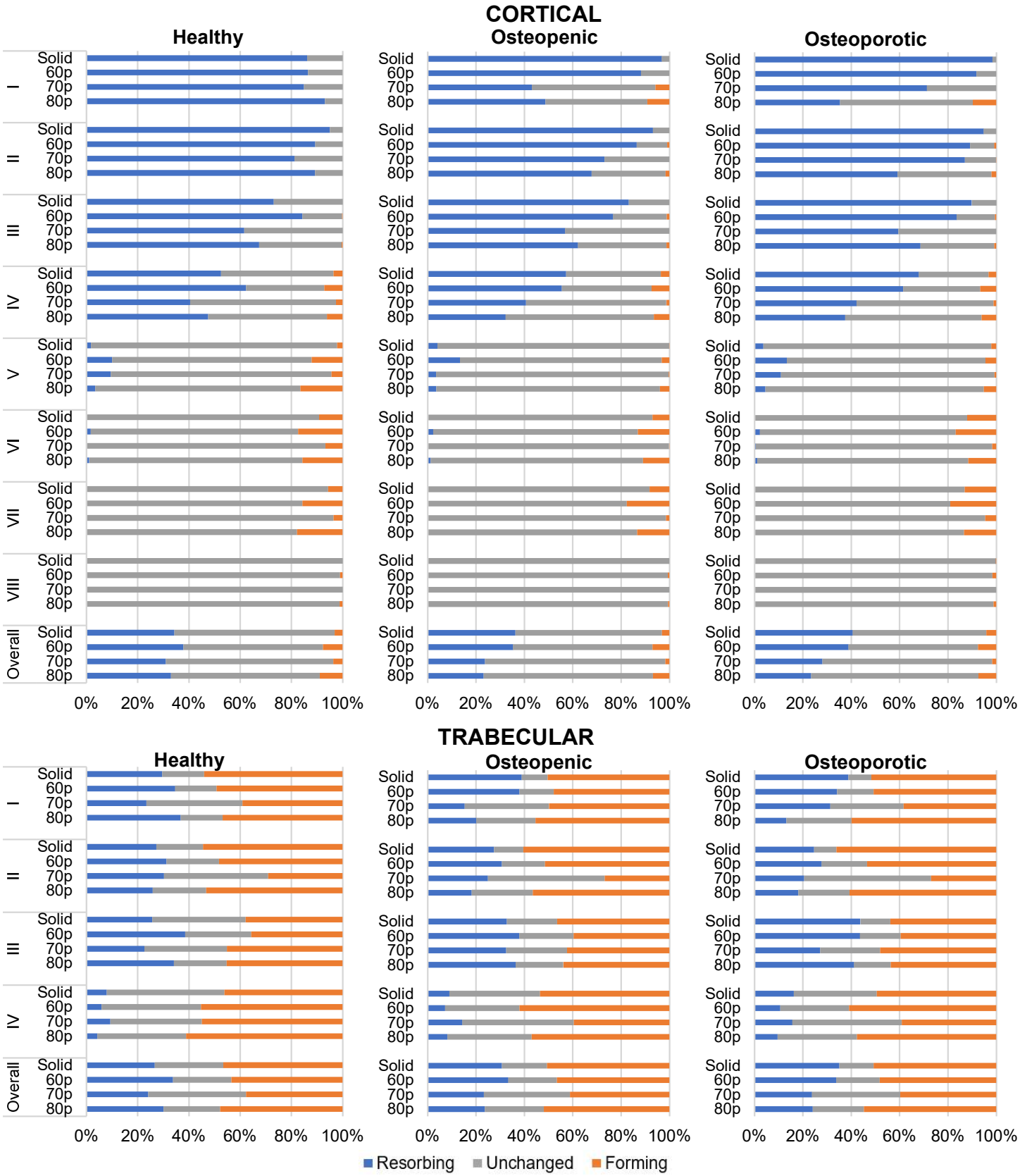

Figure 5-26. Volume percentage of bone resorption/formation in the reconstructed bones by slice and overall proximal 80mm (cortical) and 40mm (trabecular). 90° of flexion loading condition.

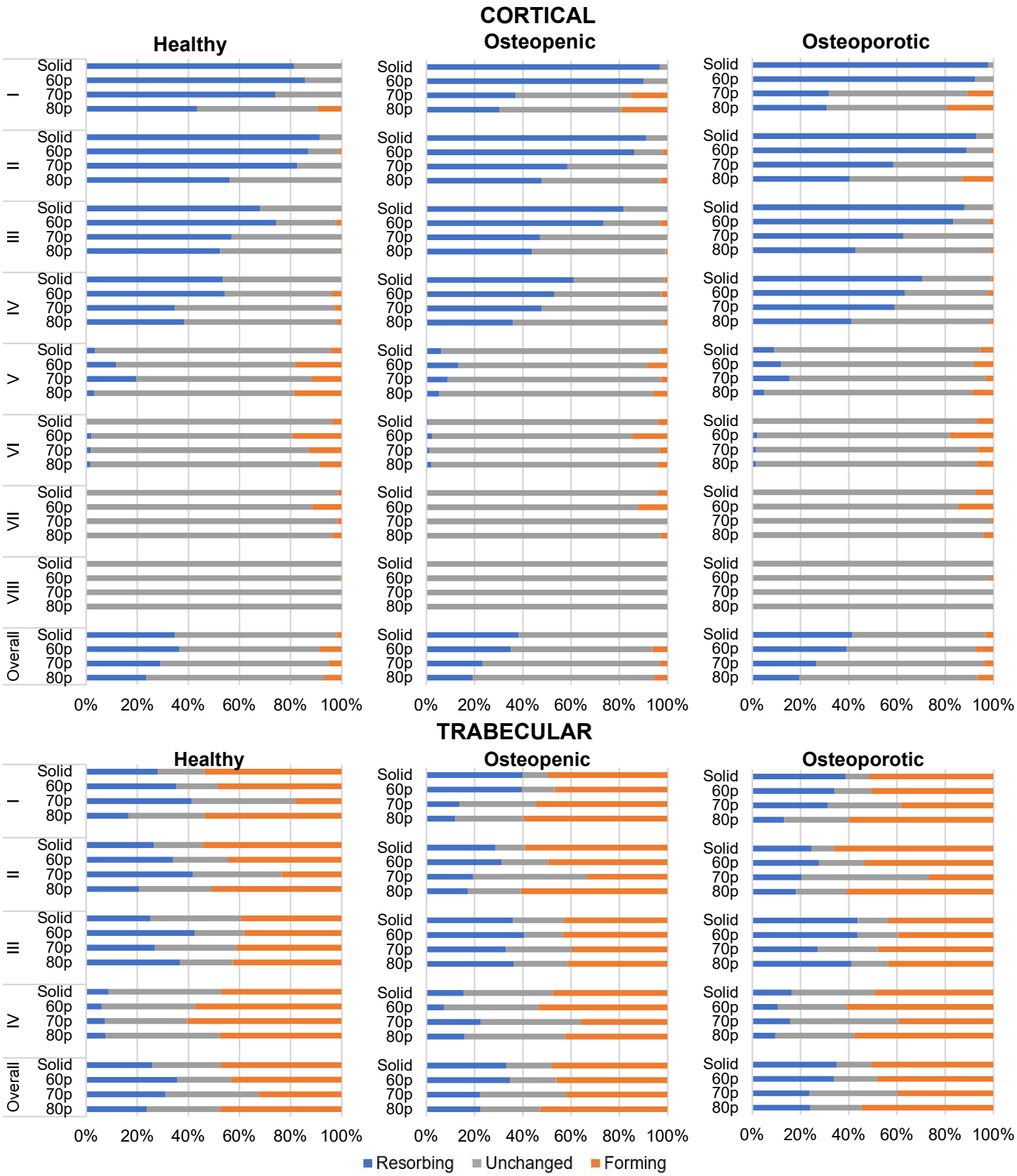

Figure 5-27. Volume percentage of bone resorption/formation in the reconstructed bone by slice and overall proximal 80mm (cortical) and 40mm (trabecular). 120° of flexion loading condition.

5.8 Solid Stem with Porous Modulus of Elasticity Figures

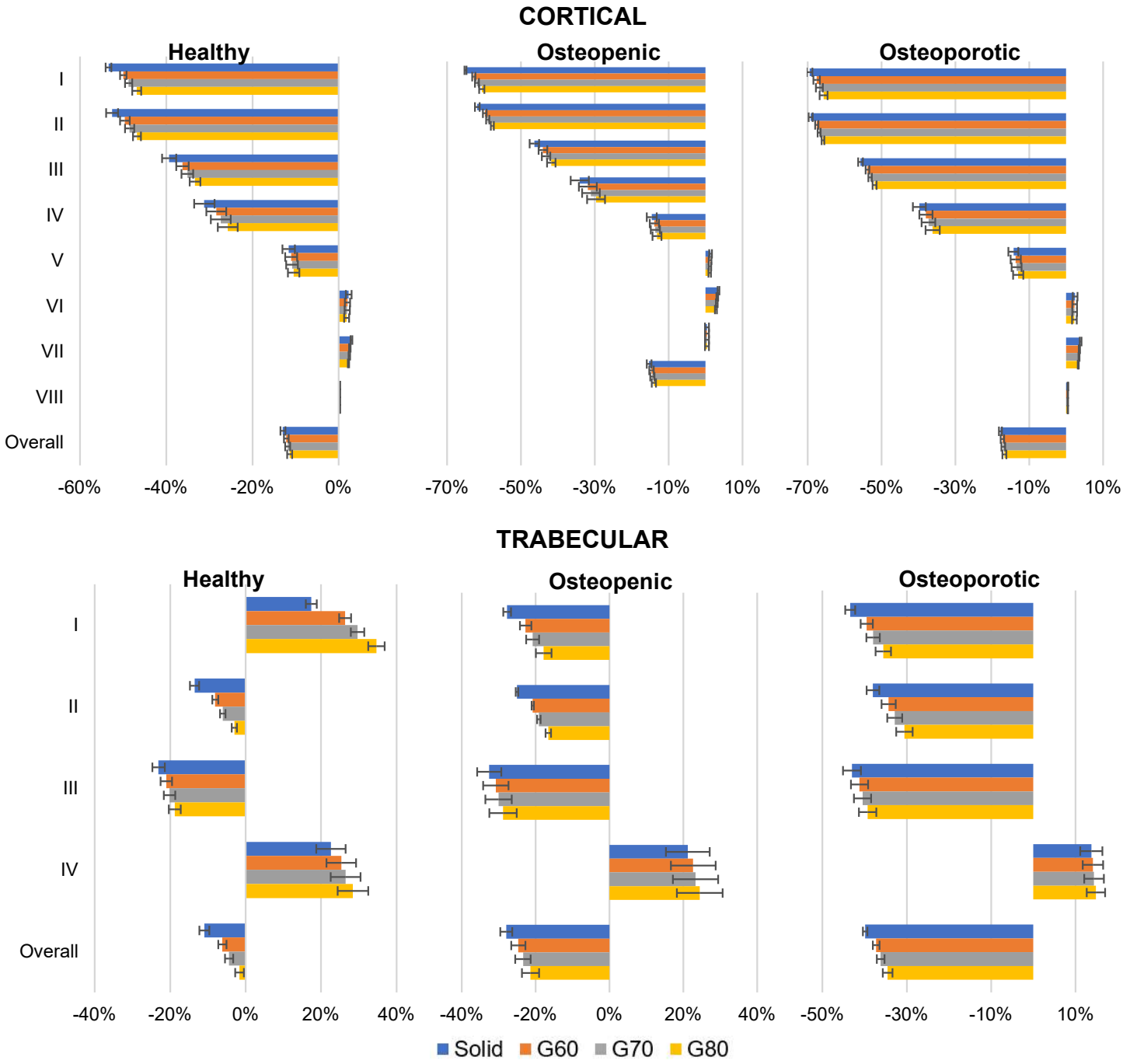

Figure 5-28. Volume-weighted average in the magnitude of Von Mises stress for the reconstructed bone as a percentage of the intact bone by slice and overall proximal 80mm (cortical) and 40mm (trabecular). Reported values are averaged across the four loading conditions. Error bars represent the standard deviation. * indicates a significant difference between two values. G60, G70, G80 represents the solid stem modelled with the moduli of elasticity of those respective gyroid porosities.

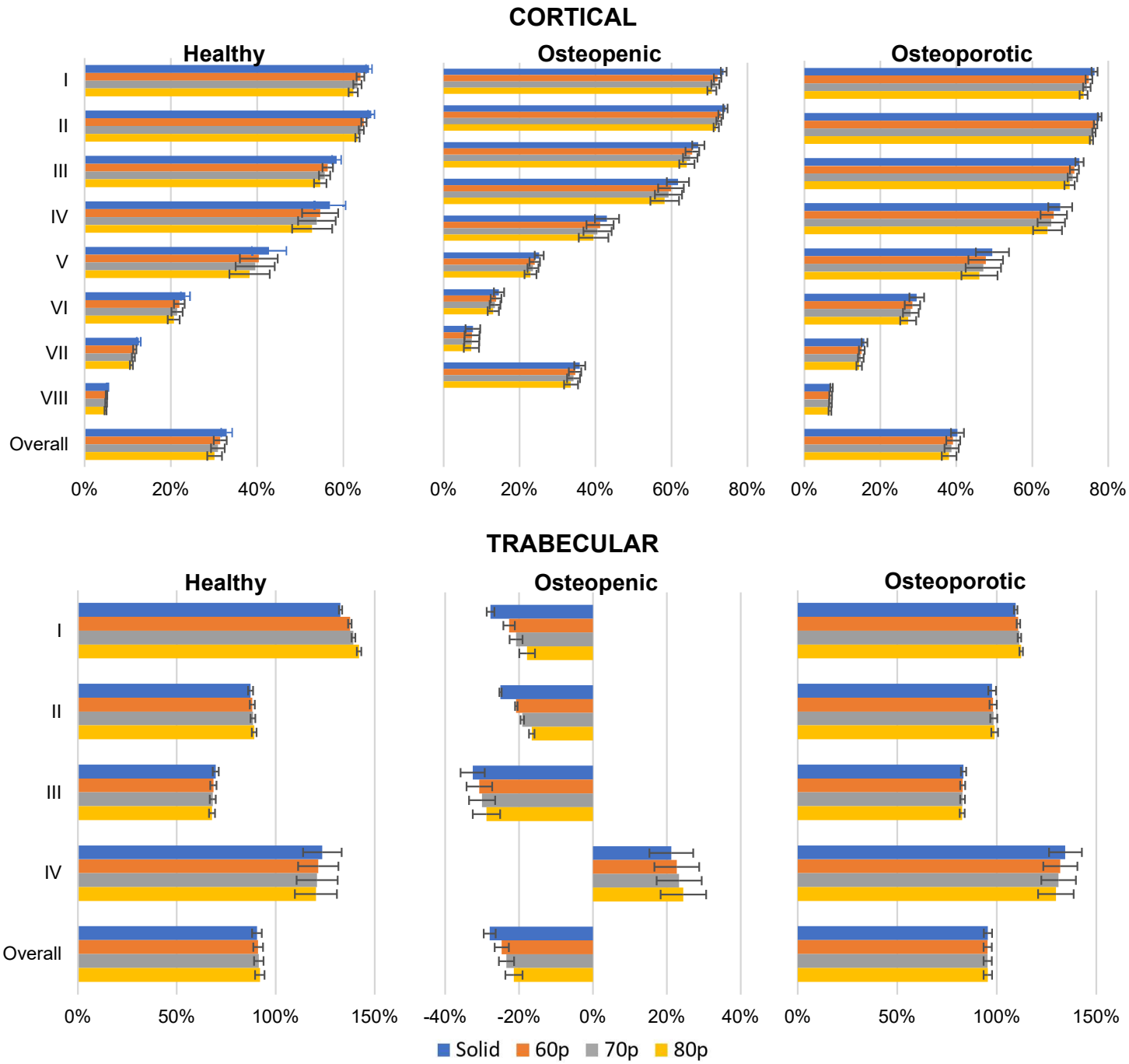

Figure 5-29. Volume-weighted deviatoric change in stress tensor for the reconstructed bone as a percentage of the intact bone by slice and overall proximal 80mm (cortical) and 40mm (trabecular). Reported values are averaged across the four loading conditions. Error bars represent the standard deviation. * indicates a significant difference between two values. G60, G70, G80 represents the solid stem modelled with the moduli of elasticity of those respective gyroid porosities.

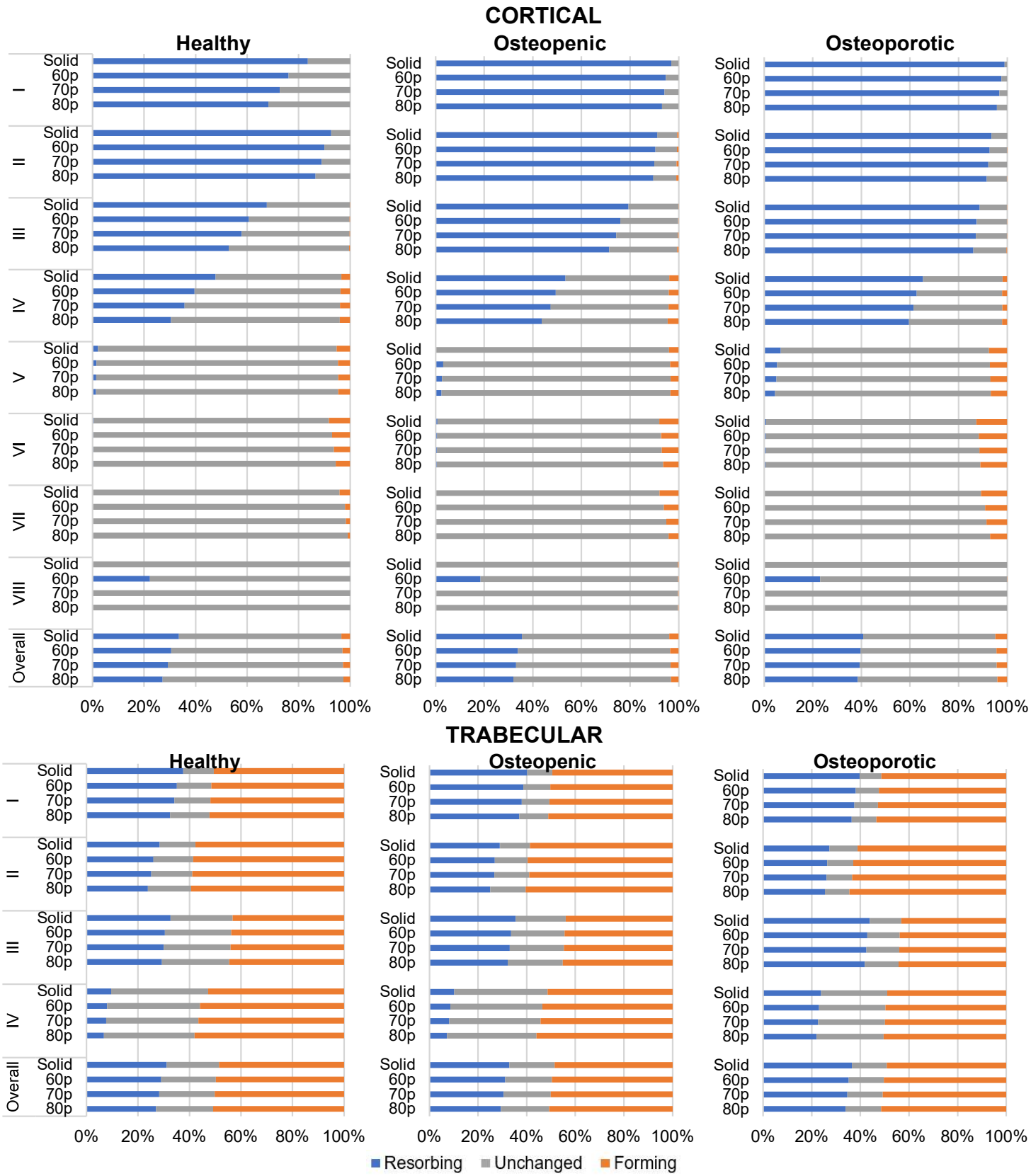

Figure 5-30. Volume percentage of bone resorption/formation in the reconstructed bone by slice and overall proximal 80mm (cortical) and 40mm (trabecular). Reported values are averaged across the four loading conditions. G60, G70, G80 represents the solid stem modelled with the moduli of elasticity of those respective gyroid porosities.

Curriculum Vitae

Name :	Sydney Hitchon
Post-secondary Education and Degrees:	Queen's University Kingston, Ontario, Canada 2016-2020 B.A.Sc. Western University London, Ontario, Canada 2020-2022 M.E.Sc.
Related Work Experience:	Teaching Assistant Engineering Ethics, Sustainable Development and the Law Western University 2021 Teaching Assistant Foundations of Engineering Practice Western University 2021-2022 Teaching Assistant Engineering Experimentation Western University 2022

Publications:

S. Hitchon, J. Milner, D. Holdsworth and R. Willing, Mechanics Of Porous Glenohumeral Implant Stems In Humeri Of Different Bone Densities, The Orthopaedic Research Society (ORS), Tampa, FL, USA (Poster, February 2022).

S. Hitchon, J. Milner, D. Holdsworth and R. Willing, Effect of Porous Shoulder Implant Stems in Different Bone Densities, Canadian Bone and Joint Conference (CBJC), London, ON, Canada (Oral Presentation, April 2022).

E. Bangsboll, **S. Hitchon**, D. Holdsworth, R. Willing, “Mechanics of Porous Tibial Implant Components”, Canadian Bone and Joint Conference (CBJC), London, ON, Canada (Poster Presentation, April 2022).

S. Hitchon, J. Milner, D. Holdsworth and R. Willing, “Porous Shoulder Implant Stems in Various Bone Densities for Single-staged Revision Surgery”, London Health Research Day (LHRD), London, ON, Canada, (Poster Presentation, May 2022).

S. Hitchon, J. Milner, D. Holdsworth and R. Willing, Mechanical Analysis of Porous Shoulder Implant Stems in Humeri of Different Bone Densities, Canadian Orthopaedic Research Society Conference (CORS), Quebec City, QC, Canada (Podium Presentation, June 2022).

S. Hitchon, J. Milner, D. Holdsworth and R. Willing, Finite Element Modelling of Porous Shoulder Implant Stems in Humeri of Varying Bone Densities, World Congress of Biomechanics (WCB), Taipei, Taiwan (Podium Presentation, July 2022).

S. Hitchon, J. Milner, D. Holdsworth and R. Willing, Impact of Porous Shoulder Implant Stems in Various Humeri Densities, International Society of Technology in Arthroplasty (ISTA), Maui, HI, USA (Poster Presentation, September 2022).